Characterization of Single Photon Sources

Master Thesis

Stijn van der Waal

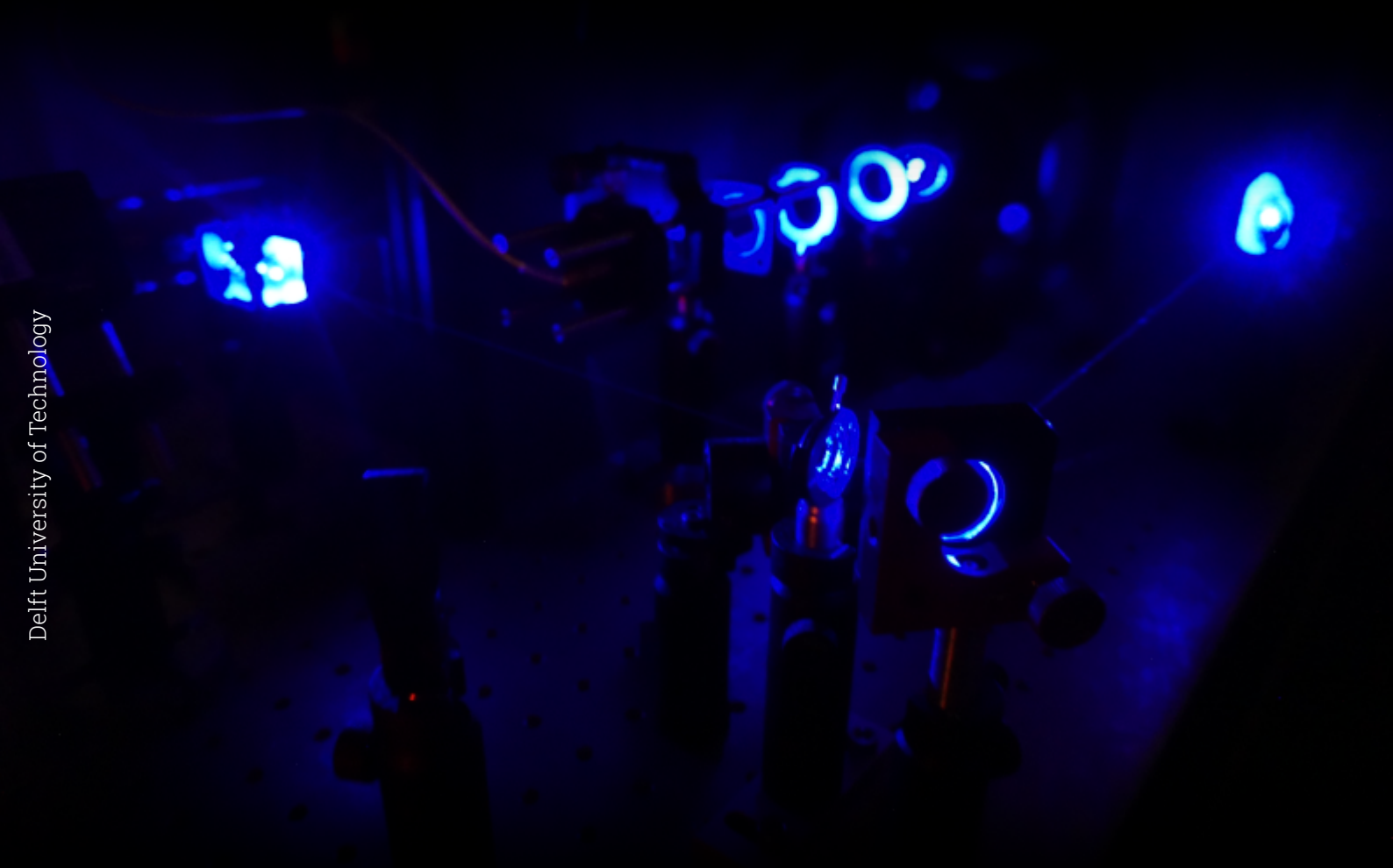

Delft University of Technology

TU Delft

Characterization of Single Photon Sources

by

Stijn van der Waal

to be defended publicly on Tuesday November 29, 2022 at 13:00.

Student number: 5175720
Project duration: April 2022 – November 2022
Thesis committee:

Prof. dr. ir. S. Pereira,	TU Delft, Optics Research Group (Supervisor)
Dr. I. E. Zadeh,	TU Delft, Optics Research Group (Supervisor)
Dr. M. N. Ali	TU Delft, TU Delft, Quantum Nanoscience.

TU Delft

I'd like to dedicate this page to acknowledge and express my gratitude towards a number of people that have been involved in this project.

Iman Esmaeil Zadeh, thank you for not having spared any effort during your time as my supervisor, not uncommonly spending entire afternoons helping me out in the lab. Also, thanks for always being available, even during weekends. Thanks for giving me a good impression of what life in academics is like, not only by having me work in your lab, but also by inviting me to go for lunch with potential collaborators for example. And lastly, thank you for even including me into your personal life and welcoming me into your family home.

Silvania Pereira, thank you for your contribution by following my progress from a distance with a critical eye, ensuring I kept on track and the organization was in order. Also, thanks for adding an extra dimension to my master project by encouraging me to participate in events like the Dutch Photonics event and Carla Camp. Lastly, thank you for regularly taking the time to discuss the project, asking me the questions that pointed me in the right direction forward and recommending and providing me with useful literature.

Even though it is very likely this page will never reach the following people, I'd still like to additionally mention:

Bruno Lopez Rodriguez, gracias por estar atento y siempre dispuesto a ayudar. Y gracias por ayudarme a familiarizarme rápidamente en el laboratorio.

Yanik Herrmann, thanks for letting me use your diamond samples and giving me some insight into your work on single-photon generation in tin-vacancy centers at Qutech.

Chunxiao Chen, thanks for being pleasant company during my time in the lab. I've enjoyed our conversations on i.a. Christianity, photonics and Freddy Mercury.

Technicians Roland and Thomas, thank you in particular for being persistent with regards to working towards a fix for the broken cryostat. Even though whom, or what exactly fixed the issue still remains somewhat of a mystery, the fact remains that the cryostat is operational now.

Our collaborators in Exeter and Stockhom for providing us with alternatives to the quantum dots in nanowire allowing us to continue our work despite a malfunctioning cryostat.

Stijn van der Waal
Den Haag, December 2022

Abstract

Single-photon emitters are at the heart of quantum optics and photonic quantum-information technologies . Identifying and characterizing such quantum emitters requires sophisticated experimental physics. In this experimental master end project, we aim to design and build an optical setup that allows for the characterization of single photon sources. More specifically, we aim to build a setup that allows for photoluminescence (PL) spectroscopy and second-order autocorrelation ($g^{(2)}$) measurements of single-photon emission (SPE).
The initial design of the optical setup is based on that of a micro photoluminescence setup and optimized for single-photon emission from indium arsenide phosphide (InAsP) quantum dots (QDs). This design therefore includes a continuous-flow liquid-helium cryostat, and a high resolution monochromator that can be used to extract the emission line of a single QD transition.
The final version of the experimental setup is demonstrated to be able to perform high resolution PL spectroscopy measurements. $g^{(2)}$ Measurements are performed on room temperature hexagonal Boron Nitride (hBN) SPE using a free-space Hanbury-Brown and Twiss (HBT) interferometer containing two geiger-mode avalanche photodiodes (APDs) indicating pronounced photon antibunching. Due to malfunctioning of the cryostat, however, measurements have exclusively been performed at room temperature.

Contents

1

Introduction

With the advent of quantum information applications like quantum cryptography and linear optical quantum computing [1], the demand for generation and control of single photons has been growing. Identifying and characterizing such single quantum emitters requires sophisticated experimental physics [2]. In this master end project an experimental setup is built that allows for the characterization of single photon sources. The setup is tested with different materials: silicon nitride (SiN), two-dimensional tungsten diselenide (WSe_2) and two-dimensional hexagonal boron nitride (hBN).

This thesis is structured as follows. In this chapter we will provide some contextual background and motivate single photon research by discussing an example of a societal application. In chapter 2 we will provide the reader with the necessary background theory for understanding the experiments performed. Section 2.1 briefly summarizes both the classical theory of light based on the equations of Maxwell, and the quantum mechanical theory of light. In particular, it its made clear how the two differ in their expressions of the second-order auto-correlation function and how a measurement of $g^{(2)}(0) < 1/2$ is indicative of a non-classical light source. Having introduced the concept of the photon allows us to investigate the photon statistics of different quantum states of light in section 2.2 where we will discern three categories based on photon number distribution. We will find that light displaying sub-Poissonian photon statistics produces $g^{(2)}(0) < 1/2$ and that this is indicative of single photon emission. Having established that the second-order auto-correlation function is essential in the identification of single photon sources, we describe in section 2.3 how $g^{(2)}(\tau)$ is experimentally determined with the Hanbury-Brown and Twiss (HBT) interferometer.
Chapter 3 reports on the experiment and results. Before the final version of the experimental setup is described in section 3.4, the reader is walked through the process that led up to the realization of the experimental setup. Section 3.1 describes how to first goal of obtaining accurate PL-spectra was achieved after two unsuccessful attempts. In section 3.2 PL-spectra of SiN, WSe_2 and hBN are presented. In section 3.3 we describe how the second goal of obtaining $g^{(2)}$ measurements was worked towards. Sections 2.3-3.3.4 describe four different attempts to include a free-space HBT interferometer in the optical setup. With the fourth and final version a $g^{(2)}$ measurement of hBN PL-emission is performed indicating indisputable photon anti-bunching. The results are presented in 3.3.4.
Chapter 4 contains a number of concluding remarks and suggestions are made for future extensions of the optical setup.

1.1. Application

In this section a major driving force behind research and development of single photon technologies is discussed: quantum cryptography. For a more extensive report and a treatment of other single photon applications like linear optical quantum computing, quantum optical metrology, quantum imaging and sensing, the reader is referred to [3], [4], [5], [6], and [7].

1.1.1. Cryptography

Cryptography (from Greek: *kryptos* "secret"; , and *graphein* "to write") is concerned with making communication secure. Two commonly used classical cryptography schemes are public key cryptography and private key cryptography.

The public key cryptography scheme assigns to each user a public and a private key. A "key" in this sense is an operation that, when applied to the message to be communicated leads to an encryption, e.g. a mathematical operation or a set of instructions leading to a reshuffling of letters or bits. As the names suggest, a user's public key is publicly accessible whereas his private key is known by himself only. In communication, the message is encrypted using the recipients public key. Ideally, the public and private keys are designed such that the encrypted message is impossible to decipher without knowledge of the recipients' private key. In practice however, this is not impossible but at best sufficiently difficult. Public key cryptography therefore stands and falls on the capability of a malicious third party being able to reverse engineer public key encryption, which currently seems to be just an issue of achieving sufficient computational power.

Private key cryptography requires the communicating parties to share a key, which is supposed to be known by them only. This scheme relies on the communicating parties being able to transmit a secret key without a third party being able to intercept and/or eavesdrop. Classically, this condition is never theoretically guaranteed. Quantum mechanically however, as will be illustrated in the next section, such a transmission *is* possible.

Both aforementioned, and in fact, all other forms of classical cryptography schemes are susceptible to leaks. The laws of quantum physics however allow for theoretically safe ways of communication. One system which exploits these enabling quantum principles is *quantum key distribution* (QKD) which allows two parties to create a secret shared key over public channels. A number of cryptography schemes have been proposed that make use of QKD. Here only the Bennet-Brassard 1984 (BB84) protocol [8] will be summarized as it sufficiently illustrates the relevance of the development of deterministic single photon sources.

The BB84 protocol, relies on the fact that it is theoretically impossible to extract from a (quantum) system all information without altering it. In this example Alice (A) wishes to send Bob (B) a private key via a public channel. Eavesdropper Eve (E) will attempt to listen in and obtain the secret key without A and B knowing of her intervention.

Starting off, A sends B a list of random bits. She will do so using single photons and an apparatus that allows her to control the polarization of each photon (a Pockels cell for instance). She uses two polarization bases: $\oplus$ and $\otimes$. Per photon, the choice of basis will be randomly chosen. In the $\oplus$ basis, $0\ ^\circ$ and 90° polarization represent a 0 and 1 respectively. In the $\otimes$ basis 0 and 1 translate into 45° and 135° respectively.

In quantum mechanical terms, the (qu)bits that A sends B will be in either one of the following four states:

$$
\begin{aligned}
|\oplus_0\rangle &= |0\rangle\,, \\
|\oplus_1\rangle &= |1\rangle\,, \\
|\otimes_0\rangle &= \frac{1}{\sqrt{2}}(|0\rangle + |1\rangle), \\
|\otimes_1\rangle &= \frac{1}{\sqrt{2}}(|0\rangle - |1\rangle).
\end{aligned}
$$

At this stage, neither B nor E knows A's choice of basis. During measuring, receiver B also randomly alters between bases $\oplus$ and $\otimes$. Half the time he will choose the same basis as A and will therefore register the correct bit. The other half of the time B will choose a basis differing from A's and will therefore

measure the correct bit only with a 50% probability.

When all qubits have been sent, B reveals to A his choice of detection bases. A then compares B's choices with her own and also publicly communicates with B when their choice of bases matched and when it did not. A and B discard of the bits for which the detection and sending bases differed from each other and keep all the other bits.

In the next step A and B will be able to determine the possible presence of E. From the remaining bits (which on average count half of the bits sent by A), B sends a subset back to A. If A sees that in 25% or more of the cases their bits disagree, the security of their communication is not guaranteed as will become clear when looking closer at how introducing E will affect the situation.

Say E has access to equipment similar to that of A and B by which she is therefore able to measure and send out qubits. The best attempt at eavesdropping and staying unnoticed is for E to intercept the qubit coming from A and without noticeable delay send out a copy of the measured qubit to B. The random nature of A's secret choice of basis however will make that E sends out the opposing bit 25% of the time. Namely, E has a 50% chance of choosing the right basis and therefore measuring and transmitting the correct bit, and 50% chance of choosing the wrong basis after which she has a 50% chance of sending B the wrong, opposing bit: $50\% \times 50\% = 25\%$.

If A records an error rate that is low enough, A and B will use the remaining, secret bits as their shared private key that will be used for encryption in their future communication.

Bibliography

[1] Pieter Kok, W. J. Munro, Kae Nemoto, T. C. Ralph, Jonathan P. Dowling, and G. J. Milburn. Linear optical quantum computing with photonic qubits. *Reviews of Modern Physics*, 79:135–174, 1 2007.

[2] Hans A. Bachor and Timothy C. Ralph. *A Guide to Experiments in Quantum Optics*. Wiley, 9 2019.

[3] Vittorio Giovannetti, Seth Lloyd, and Lorenzo MacCone. Advances in quantum metrology, 4 2011.

[4] Marco Genovese. Real applications of quantum imaging. *Journal of Optics*, 18:073002, 7 2016.

[5] L A Lugiato, A Gatti, and E Brambilla. Quantum imaging. *Journal of Optics B: Quantum and Semiclassical Optics*, 4:S176–S183, 6 2002.

[6] E. Knill, R. Laflamme, and G. J. Milburn. A scheme for efficient quantum computation with linear optics. *Nature*, 409:46–52, 1 2001.

[7] Jeremy L. O'Brien, Akira Furusawa, and Jelena Vučković. Photonic quantum technologies, 12 2009.

[8] Charles H. Bennett and Gilles Brassard. Quantum cryptography: Public key distribution and coin tossing. 3 2020.

2

Background and Theory

2.1. Classical vs quantum theory of light

In this section, both the classical and quantum mechanical theories of light are briefly described. The main purpose of this section is to introduce the second-order auto correlation function which is the main tool used in this thesis for identifying single photon sources. For a much more in-depth treatment of the following subject matter, the reader is referred to [1], [2], [3], [4] [5].

2.1.1. Classical

Classical electromagnetism is concerned with the behaviour of electromagnetic fields (the electric field $\mathbf{E}$ and the magnetic field $\mathbf{B}$) and electrical charges. Their behaviour is governed by the Maxwell equations, which in SI units are:

$$\boldsymbol{\nabla} \cdot \mathbf{E} = \frac{\rho}{\varepsilon_0} \tag{2.1}$$

$$\boldsymbol{\nabla} \times \mathbf{E} = -\frac{\partial \mathbf{B}}{\partial t} \tag{2.2}$$

$$\boldsymbol{\nabla} \cdot \mathbf{B} = 0 \tag{2.3}$$

$$\boldsymbol{\nabla} \times \mathbf{B} = \mu_0 \epsilon_0 \frac{\partial \mathbf{E}}{\partial t} + \mu_0 \mathbf{J}, \tag{2.4}$$

where μ_0 and ϵ_0 are the permeability and permittivity of vacuum which are empirically determined to be

$$\mu_0 = 1.256\,637\,062\,12(19) \times 10^{-6}\,\mathrm{N/A^2} \text{ and,} \tag{2.5}$$

$$\epsilon_0 = 9.854\,187\,812\,8(13) \times 10^{-12}\,\mathrm{F\,m^{-1}}. \tag{2.6}$$

In general, given a charge distribution $\rho(\mathbf{r}, t)$ and current distribution $\mathbf{J}(\mathbf{r}, t)$, one can solve Maxwell's equations via the introduction of the scalar and vector potentials V and $\mathbf{A}$ which relate to the electric and magnetic field as:

$$\mathbf{E} = -\nabla V - \frac{\partial \mathbf{A}}{\partial t} \tag{2.7}$$

$$\mathbf{B} = \boldsymbol{\nabla} \times \mathbf{A}. \tag{2.8}$$

In the Lorenz gauge, this reduces the problem of solving the six partial differential equations making up Maxwell's equations, to solving four inhomogeneous wave equations. With $\Box$ the d'Alambertian operator, they are:

$$\Box^2 V = -\frac{\rho}{\epsilon_0} \tag{2.9}$$

$$\Box^2 \mathbf{A} = -\mu_0 \mathbf{J}. \tag{2.10}$$

For our brief discussion on linear classical optics however, the situation is simplified. Classical optics regards light as consisting of electromagnetic waves which are solutions to the Maxwell equations in vacuum (or in insulators, i.e. media for which the free charge and currents are null):

$$\boldsymbol{\nabla} \cdot \mathbf{D} = 0 \tag{2.11}$$

$$\boldsymbol{\nabla} \times \mathbf{E} = -\frac{\partial \mathbf{B}}{\partial t} \tag{2.12}$$

$$\boldsymbol{\nabla} \cdot \mathbf{B} = 0 \tag{2.13}$$

$$\boldsymbol{\nabla} \times \mathbf{H} = \frac{\partial \mathbf{D}}{\partial t}, \tag{2.14}$$

where we have introduced the fields $\mathbf{D}$ and $\mathbf{H}$ that include the electric and magnetic response of a linear isotropic medium with permittivity ϵ and permeability μ :

$$\mathbf{D} = \epsilon \mathbf{E} \tag{2.15}$$

$$\mathbf{H} = \frac{1}{\mu}\mathbf{B}. \tag{2.16}$$

As knowledge of either $\mathbf{E}$ or $\mathbf{B}$ is sufficient for describing the full electromagnetic field and the magnitude of $\mathbf{B}$ is commonly orders of magnitude smaller than that of $\mathbf{E}$ making it irrelevant in most optical problems, we'll limit the discussion to the electrical field from here on.
From the Maxwell equations, we obtain a three dimensional wave equation after taking the curl of the Maxwell-Faraday equation (eqn. 2.12), applying the identity $\boldsymbol{\nabla} \times (\boldsymbol{\nabla} \times \mathbf{E}) = \boldsymbol{\nabla} \cdot (\boldsymbol{\nabla} \cdot \mathbf{E}) - \nabla^2 \mathbf{E}$ and using Gauss's law (eqn. 2.11) to get rid of the divergence term and Ampere's law (eqn. 2.14) to substitute for the curl of $\mathbf{B}$:

$$\nabla^2 \mathbf{E} = \mu\epsilon \frac{\partial^2 \mathbf{E}}{\partial t^2} \tag{2.17}$$

which indeed implies that the vacuum (or insulators) support the propagation of electromagnetic waves that travel with speed:

$$v = \frac{1}{\sqrt{\mu\epsilon}}. \tag{2.18}$$

The speed of these electromagnetic waves in vacuum is then $1/\sqrt{\mu_0\epsilon_0} \approx c \equiv 299\,792\,458\,\mathrm{m\,s^{-1}}$.
By intoducing the refractive index n of a certain medium as:

$$n = \sqrt{\frac{\epsilon\mu}{\epsilon_0\mu_0}}, \tag{2.19}$$

the speed of light in a medium can be expressed as the ratio of c and n:

$$v = \frac{c}{n}. \tag{2.20}$$

For any medium other than the vacuum (in so far the vacuum can be regarded as a medium) the magnitude of n is larger than 1, which makes that light travels slower through matter than through vacuum. In general. it can be stated that the index of refraction relates the optical properties of a material to its dielectric properties and dictates e.g. the occurrence of reflection, refraction and dispersion.
A solution to eqn 2.17 is a plane wave of frequency ω which in complex notation is given by:

$$\mathbf{E}(\mathbf{r}, t) = \mathrm{Re}\left(\mathbf{E}_0 e^{i(\mathbf{k}\cdot\mathbf{r} - \omega t + \phi)}\right). \tag{2.21}$$

The frequency ω of light determines its colour. For a constant value of ω, the electromagnetic wave is therefore said to be monochromatic. The frequency aswell as the phase can also vary with time and/or space $\omega = \omega(\mathbf{r}, t)$, $\phi = \phi(\mathbf{r}, t)$. The variability of ω and ϕ affect the frequency and phase 'stability' of

light. The idea of stability of light brings us to the concept of coherence, which is further discussed by looking at the following experiment. A clear demonstration of the wave nature of light is Young's double slit experiment (figure 2.1). Light passes through two slits before illuminating a screen. It was first performed by Thomas Young in 1802 [6] who observed that for certain types of light interference fringes could be observed on the screen. As we will see in the following analysis, the extent to which light is able to interfere with itself, depends on the degree of first order coherence.

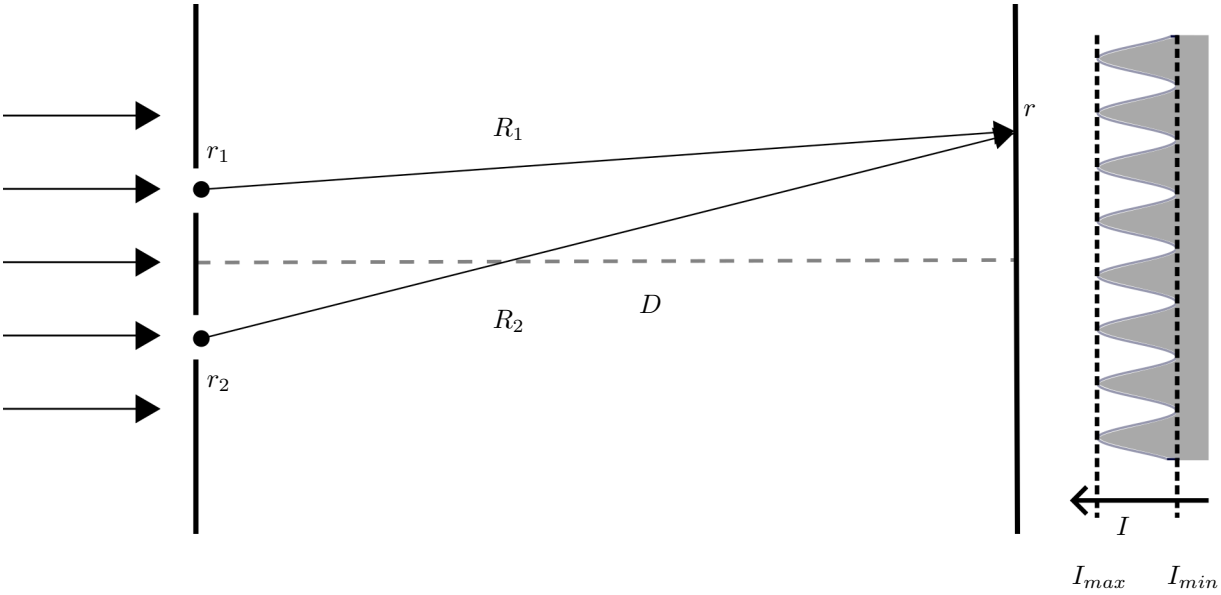

Figure 2.1: Young's double slit experiment demonstrating the wave nature of light. Interference fringes appear depending on the degree of first order coherence.

In our analysis, we use Huygens' principle by assuming that light at the slits originates from spherically emitting point sources. The field at position r on the screen is then a superposition of the two fields coming from the two slits and is expressed as:

$$E(r,t) = K_1 E(r_1, t-\tau_1) + K_2 E(r_2, t-\tau_2), \tag{2.22}$$

where K_1 and K_2 depend on the distances R_1 and R_2 and $\tau_1 = R_1/c$ and $\tau_2 = R_2/c$ are the times it takes for the light to travel from the slits to the point r. Writing $t_i = t - \tau_i$, the intensity at point r is:

$$\begin{aligned} I(r,t) &= \langle |E(r,t)|^2 \rangle && (2.23)\\ &= |K_1|^2 \langle |E(r_1,t_1|^2 \rangle + |K_2|^2 \langle |E(r_2,t_2|^2 \rangle && (2.24)\\ &+ 2\,\mathrm{Re}(K_1^* K_2 \langle E^*(r_1,t_1) E(r_2,t_2) \rangle) && (2.25)\\ &= I_1 + I_2 + 2\,\mathrm{Re}(K_1^* K_2 G^{(1)}(r_1,t_1,r_2,t_2)). && (2.26) \end{aligned}$$

where I_1 and I_2 are the contributions to the intensity at point r by each of the fields independently, and the third term is a contribution arising from interference which in the last line is written in terms of the first order correlation function:

$$G^{(1)}(x_1,x_2) = \langle E^*(x_1) E(x_2) \rangle, \tag{2.27}$$

writing $x_i = r_i, t_i$. The normalized first-order coherence function is defined as:

$$g^{(1)}(x_1,x_2) = \frac{\langle E^*(x_1) E(x_2) \rangle}{\sqrt{\langle |E(x_1)|^2 \rangle \langle |E(x_2)|^2 \rangle}}. \tag{2.28}$$

To make apparent the sinusoidal interference pattern that arises on the screen, we write $K_i = |K_i| e^{i\phi_i}$ and $g^{(1)} = |g^{(1)}| e^{i\Phi}$. In terms of $g^{(1)}(x_1,x_2)$, the intensity then becomes:

$$I(r,t) = I_1 + I_2 + 2\sqrt{I_1 I_2} |g^{(1)}(x_1,x_2)| \cos\left(\Phi - (\phi_1 - \phi_2)\right). \tag{2.29}$$

The magnitude of $g^{(1)}$ therefore determines the extent to which interference fringes appear. More precisely, we can define a fringe visibility ν which can be shown to be equal to the magnitude of $g^{(1)}$ (beyond the scope of this text):

$$\nu = \frac{I_{max} - I_{min}}{I_{max} + I_{min}} = |g^{(1)}(x_1, x_2)|. \tag{2.30}$$

$|g^{(1)}|$ can be regarded as a measure of first-order coherence. Three types of coherence are distinguished:

$$|g^{(1)}(x_1, x_2)| = 1, \qquad \text{complete coherence,} \tag{2.31}$$

$$0 < |g^{(1)}(x_1, x_2)| < 1, \qquad \text{partial coherence,} \tag{2.32}$$

$$|g^{(1)}(x_1, x_2)| = 0, \qquad \text{incoherent.} \tag{2.33}$$

When $g^{(1)}$ is evaluated for an electromagnetic wave at one point in space but different points in time, $g^{(1)}$ is dependent on time difference τ only and will give a measure of temporal self coherence. A coherence time τ_c can be defined which defines a temporal range over which the light wave can be regarded to be coherent. Qualitatively, when the phase of a wave is known at certain position at time t_1, then the phase at this position is known with a high degree of certainty at time t_2 given that $|t_2 - t_1| << \tau_c$, but with very low degree of certainty if $t_2 - t_1| >> \tau_c$. In a similar fashion, light can be assigned a degree of spatial self coherence by considering $g^{(1)}$ at one point in time but different points in space. The coherence length, which relates to the coherence time as $L_c = c\tau_c$, then defines a spatial range over which light is coherent. Because in this manner correlations of the light with itself are evaluated, one sometimes speaks of auto correlation.

In anticipation of section 2.1.2, we end this section by defining the intensity analogue of the normalized first-order auto correlation function as:

$$\begin{aligned} g^{(2)}_{classical}(\tau) &= \frac{\langle E^*(t)E^*(t+\tau)E(t+\tau)E(t)\rangle}{\langle E^*(t)E(t)\rangle\langle E^*(t+\tau)E(t+\tau)\rangle} \\ &= \frac{\langle I(t)I(t+\tau)\rangle}{\langle I(t)\rangle\langle I(t+\tau)\rangle}, \end{aligned} \tag{2.34}$$

which is the normalized second-order auto correlation function. Where 2.28 is a measure of correlations in electric field amplitude, 2.34 quantifies intensity correlations and is a degree of second-order coherence.

It is interesting to look at its accepted values when evaluated at $\tau = 0$:

$$g^{(2)}_{classical}(0) = \frac{\langle I(t)^2\rangle}{\langle I(t)\rangle^2}. \tag{2.35}$$

We can rewrite the averages in the numerator and denumerator in the limit of $N \to \infty$ as:

$$\langle I(t)^2\rangle = \frac{1}{N}\sum_i^N I(t_i)^2 \tag{2.36}$$

$$\langle I(t)\rangle^2 = \left(\frac{1}{N}\sum_i^N I(t_i)\right)^2. \tag{2.37}$$

From Cauchy's inequality, we know that $2I(t_i)I(t_j) \leq I(t_i)^2 + I(t_j)^2$, therefore:

$$\sum_i^N\sum_j^N I(t_i)I(t_j) \leq \frac{1}{2}\sum_i^N\sum_j^N \left(I(t_i)^2 + I(t_j)^2\right) \tag{2.38}$$

$$= \frac{N+1}{2}\sum_i^N I(t_i)^2 \tag{2.39}$$

$$\leq N\sum_i^N I(t_i)^2, \qquad \text{for } N \geq 1. \tag{2.40}$$

We can expand $\langle I(t)\rangle^2$ by writing eqn 2.37 in terms of its cross terms so that we can use the Cauchy inequality to come to the following conclusion:

$$\langle I(t)^2\rangle = \left(\frac{1}{N}\sum_i^N I(t_i)\right)^2 \tag{2.41}$$

$$= \frac{1}{N^2}\sum_i^N\sum_j^N I(t_i)I(t_j) \tag{2.42}$$

$$\leq \frac{1}{N}\sum_i^N I(t_i)^2 = \langle I(t)^2\rangle, \tag{2.43}$$

In other words, we find that classically, $g^{(2)}(0)$ will always be greater or equal to 1:

$$g^{(2)}_{classical}(0) = \frac{\langle I(t)^2\rangle}{\langle I(t)\rangle^2} \geq 1. \tag{2.44}$$

Experimentally however, it has been demonstrated that this inequality is not always satisfied, hinting towards the incompleteness of the classical theory and the need for a different formalism. In the next section we will see how the quantum mechanical counterpart of $g^{(2)}$ allows for values of $g^{(2)}(0) < 1$ and we will find how the second-order autocorrelation function is an indispensable tool for identifying single photon sources.

2.1.2. Quantum

In the quantum mechanical description of light, the electromagnetic field of the theory of Maxwell is quantized in modes. Each mode is regarded as an independent quantum harmonic oscillator, where the electric and magnetic fields play the roles of canonical position and momentum.
For simplicity, we consider a simple example of a one dimensional optical cavity in which the electromagnetic field vanishes at its boundaries ($E(0,t) = 0$ and $E(L,t) = 0$). A solution to this boundary value problem is the single-mode field:

$$E(x,t) = \left(\frac{2\omega^2}{V\varepsilon_0}\right)^{1/2} q(t)\sin(kx) \tag{2.45}$$

$$B(x,t) = \left(\frac{\mu_0\varepsilon_0}{k}\right)\left(\frac{2\omega^2}{V\varepsilon_0}\right)^{1/2} \dot{q}(t)\cos(kx), \tag{2.46}$$

where V is the effective volume of the cavity, $E(x,t)$ the magnitude of the electric field pointing in the y-direction and $B(x,t)$ the magnitude of the magnetic field in the z-direction. When writing $p(t) = \dot{q}(t)$ and looking at the classical Hamiltonian of the single-mode field it becomes apparent that the Hamiltonian is equivalent to that of a classical harmonic oscillator:

$$H = \frac{1}{2}\int dV \left(\varepsilon_0 E^2(x,t) + \frac{1}{\mu_0}B^2(x,t)\right) \tag{2.47}$$

$$= \frac{1}{2}(p^2 + \omega^2 q^2). \tag{2.48}$$

The step from classical to quantum is made when we replace the canonical variables p and q by the Hermitian, non commuting operators $\hat{p}$ and $\hat{q}$:

$$\hat{H} = \frac{1}{2}(\hat{p}^2 + \omega^2\hat{q}^2). \tag{2.49}$$

The single-mode electric and magnetic fields now become the field operators:

$$\hat{E}(x,t) = \left(\frac{2\omega^2}{V\varepsilon_0}\right)^{1/2} \hat{q}(t)\sin(kx) \tag{2.50}$$

$$\hat{B}(x,t) = \left(\frac{\mu_0\varepsilon_0}{k}\right)\left(\frac{2\omega^2}{V\varepsilon_0}\right)^{1/2} \hat{p}(t)\cos(kx). \tag{2.51}$$

With the introduction of the *creation* ($\hat{a}^\dagger$) and *annihilation* ($\hat{a}$) operators:

$$\hat{a}^\dagger = (2\hbar\omega)^{(-1/2)}(\omega\hat{q} + i\hat{p}) \tag{2.52}$$

$$\hat{a} = (2\hbar\omega)^{(-1/2)}(\omega\hat{q} + i\hat{p}), \tag{2.53}$$

which satisfy the bosonic commutation relation:

$$[\hat{a}, \hat{a}^\dagger] = 1, \tag{2.54}$$

we can rewrite the field operators:

$$\hat{E}(x,t) = \mathcal{E}_0(\hat{a} + \hat{a}^\dagger)\sin(kx) \tag{2.55}$$

$$\hat{B}(x,t) = \mathcal{B}_0\frac{1}{i}(\hat{a} - \hat{a}^\dagger)\cos(kx), \tag{2.56}$$

with $\mathcal{E}_0 = (\hbar\omega/\epsilon_0 V)^{1/2}$ and $\mathcal{B}_0 = (\mu_0/k)(\epsilon_0\hbar\omega^3/V)^{1/2}$, and the Hamiltonian in eqn 2.49 can be rewritten as:

$$\hat{H} = \hbar\omega\left(\hat{a}^\dagger\,\hat{a} + \frac{1}{2}\right). \tag{2.57}$$

Using the ladder operator method (see for instance [7]) with $\hat{a}^\dagger$ and $\hat{a}$ as the ladder operators, the energy spectrum of $\hat{H}$ can be evaluated.

Taking $|n\rangle$ to be an eigenfunction of $\hat{H}$ with energy E_n, we find that applying $\hat{a}^\dagger$ to $|n\rangle$ gives another eigenfunction with eigenvalue (or energy) $E_n + \hbar\omega$:

$$\hat{H}\,\hat{a}^\dagger\,|n\rangle = ([\hat{H}, \hat{a}^\dagger] + \hat{a}^\dagger\hat{H})\,|n\rangle \tag{2.58}$$

$$= (E_n + \hbar\omega)\,|n+1\rangle \tag{2.59}$$

Similarly, $\hat{a}\,|n\rangle$ is an eigenfunction of $\hat{H}$ with energy $E_n - \hbar\omega$.

$$\hat{H}\,\hat{a}\,|n\rangle = (E_n - 1)\,|n-1\rangle\,. \tag{2.60}$$

It can thus be said that operators $\hat{a}^\dagger$ and $\hat{a}$ create and annihilate discrete energy quanta (hence the naming) each of energy $\hbar\omega$. These quanta are universally referred to as photons. In quantum field theory therefore, photons are not considered to be localized "corpuscles" of light, but rather excitations of electromagnetic modes.

Noting that $\hat{a}\,|0\rangle = 0$, the energy of the groundstate is readily evaluated as:

$$\hat{H}\,|0\rangle = \hbar\omega\left(\hat{a}^\dagger\,\hat{a} + \frac{1}{2}\right)|0\rangle = \frac{1}{2}\hbar\omega\,|0\rangle = E_0\,|0\rangle\,. \tag{2.61}$$

Therefore

$$\hat{H}\,|n\rangle = \hbar\omega(n + \frac{1}{2})\,|n\rangle\,. \tag{2.62}$$

$$\tag{2.63}$$

Comparing eqns 2.57 and 2.62, we can introduce the number operator $\hat{n}$:

$$\hat{n} = \hat{a}^\dagger\,\hat{a}, \tag{2.64}$$

which when applied to $|n\rangle$, which is commonly referred to as a *number state*, returns the number of photons in the corresponding mode. Repeated application of the creation operator on the ground state produces any single-mode number state:

$$|n\rangle = \frac{(\hat{a}^\dagger)^n}{\sqrt{n!}}\,|0\rangle\,, \tag{2.65}$$

where the factor $1/\sqrt{n!}$ ensures that the state is normalized.

These results for a single-mode field in a one dimensional cavity can be extended to multi-mode electromagnetic fields in three dimensional freespace by going through similar steps for a three dimensional cubic cavity of sides L with with periodic boundary conditions (reflective walls) and taking the limit of $L \to \infty$. In general then, the electric and magnetic field are expressed as:

$$\hat{\mathbf{E}}(\mathbf{r},t) = i\sum_{\mathbf{k}s}\left(\frac{\hbar\omega_k}{2\varepsilon_0 V}\right)^{1/2}\mathbf{e}_{\mathbf{k}s}\left[\hat{a}_{\mathbf{k}s}e^{i(\mathbf{k}\cdot\mathbf{r}-\omega_k t)} - \hat{a}^\dagger_{\mathbf{k}s}e^{-i(\mathbf{k}\cdot\mathbf{r}-\omega_k t)}\right], \tag{2.66}$$

$$\hat{\mathbf{B}}(\mathbf{r},t) = \sqrt{\mu_0\varepsilon_0}i\sum_{\mathbf{k}s}(\mathbf{k}/|\mathbf{k}|\times\mathbf{e}_{\mathbf{k}s})\left(\frac{\hbar\omega_k}{2\varepsilon_0 V}\right)^{1/2}\mathbf{e}_{\mathbf{k}s}\left[\hat{a}_{\mathbf{k}s}e^{i(\mathbf{k}\cdot\mathbf{r}-\omega_k t)} - \hat{a}^\dagger_{\mathbf{k}s}e^{-i(\mathbf{k}\cdot\mathbf{r}-\omega_k t)}\right] \tag{2.67}$$

where a sum over wave vectors $\mathbf{k}$ is a sum over normal modes, each labeled by $\mathbf{k} = (m_x, m_y, m_z)$ and index s takes on values 1 and 2 denoting two independent orthogonal polarizations. And any number state can then be generated from the electromagnetic vacuum ($|\{0\}\rangle$):

$$|n_j\rangle = \prod_j \frac{\hat{a}_j^{\dagger n_j}}{\sqrt{n_j!}}\,|\{0\}\rangle\,, \tag{2.68}$$

with index j denoting the specific mode. The number states constitute the basis vectors of a bosonic *Fock space*.

Similarly to the case of the photon creation and annihilation operators, with the introduction of the *collective annihilation* and *creation operator* respectively as:

$$\hat{E}^{(+)}(\mathbf{r},t) = i\sum_{\mathbf{k}s}\left(\frac{\hbar\omega_k}{2\varepsilon_0 V}\right)^{1/2}\mathbf{e}_{\mathbf{k}s}\,\hat{a}_{\mathbf{k}s}e^{i(\mathbf{k}\cdot\mathbf{r}-\omega_k t)} \tag{2.69}$$

$$\hat{E}^{(-)} = \left[\hat{E}^{(+)}(\mathbf{r},t)\right]^{\dagger}, \tag{2.70}$$

the electric field can also be written as:

$$\hat{E}(\mathbf{r},t) = \hat{E}^{(+)}(\mathbf{r},t) + \hat{E}^{(-)}(\mathbf{r},t). \tag{2.71}$$

For a step by step derivation the reader is referred to §2.4 of [1].

As mentioned before, the second-order auto-correlation function is a measure of intensity correlations. Intensity in the quantum mechanical framework is proportional to the photon flux incident on a photodetector. To introduce the quantum version of the second-order auto-correlation function we therefore look at the phenomenon of photodetection in a bit more detail.

In a detection event of a photon, it is absorbed by some optical active material which will subsequently release a photon-electron that is later counted by the experimenter. Such a measurement is therefore photon-destructive, as it involves the annihilation of a photon. For this reason, in the quantum mechanical description of photodetection, not the creation, but the annihilation operator $\hat{E}^{(+)}(t)$ appears. For simplicity, we will assume that all quantities that can be assigned a certain polarization share the same polarization such that we can consider them to be scalar. Moreover, the electric fields are assumed to be in pure states so that they do not have to be expressed in terms of density matrices and the detector is modeled by a single, photon absorbing atom. We can then make use of Fermi's golden rule to calculate the photon absorption rate of our detector atom as:

$$W_i(t) = \sum_{\psi_f} |\left\langle\psi_f\right| \hat{E}^{(+)}(t)\left|\psi_i\right\rangle|^2 \tag{2.72}$$

$$= \sum_{\psi_f} \left\langle\psi_i\right| \hat{E}^{(-)}(t)\left|\psi_f\right\rangle\left\langle\psi_f\right| \hat{E}^{(+)}(t)\left|\psi_i\right\rangle \tag{2.73}$$

$$= \left\langle\psi_i\right| \hat{E}^{(-)}(t)\hat{E}^{(+)}(t)\left|\psi_i\right\rangle, \tag{2.74}$$

where $|\psi_i\rangle$ is the state of the electric field before and $|\psi_f\rangle$ the state of the electric field after absorption. In the last step we have summed over all possible final states and we made use of the completeness relation:

$$\sum_{\psi_f}\left|\psi_f\right\rangle\left\langle\psi_f\right| = 1. \tag{2.75}$$

Being the photon absorbtion rate, the expression of eqn 2.74 can be regarded as a measure of the intensity of light at the position of the detector. More generally, we define the first-order correlation function as:

$$G^{(1)}(x_1,x_2) = \langle\hat{E}^{(-)}(x_1)\hat{E}^{(+}(x_2)\rangle, \tag{2.76}$$

where $x_i = (\mathbf{r}_i, t_i)$ is a position in space-time. $G^{(1)}(x_1,x_2)$ is then a measure of correlation between electric fields at x_1 and x_2. This function can be normalized to obtain the normalized first-order coherence function:

$$g^{(1)}(x_1,x_2) = \frac{G^{(1)}(x_1,x_2)}{\left[G^{(1)}(x_1,x_1)G^{(1)}(x_2,x_2)\right]^{(1/2)}}. \tag{2.77}$$

In complete analogy with the classical case described in section 2.1.1, three categories are distinguished:

$$|g^{(1)}(x_1, x_2)| = 1, \quad \text{complete coherence,} \tag{2.78}$$

$$0 < |g^{(1)}(x_1, x_2)| < 1, \quad \text{partial coherence,} \tag{2.79}$$

$$|g^{(1)}(x_1, x_2)| = 0, \quad \text{incoherent.} \tag{2.80}$$

It is interesting to look at the absorption rate at a time τ after the detection of the first photon. When the annihilation operator $\hat{E}^{(+)}(t)$ is applied to the original field, the field after absorption is obtained:

$$|\psi_2\rangle = \hat{E}^{(+)}(t)\,|\psi_1\rangle\,. \tag{2.81}$$

Therefore, the absorption rate at time $t + \tau$ is:

$$G^{(2)}(\tau) = \langle\psi_2|\,\hat{E}^{(-)}(t+\tau)\hat{E}^{(+)}(t+\tau)\,|\psi_2\rangle \tag{2.82}$$

$$= \langle\psi_1|\,\hat{E}^{(-)}(t)\hat{E}^{(-)}(t+\tau)\hat{E}^{(+)}(t+\tau)\hat{E}^{(+)}(t)\,|\psi_1\rangle\,. \tag{2.83}$$

This is the quantum second-order correlation function which translates into a probability of detecting a photon a time τ after the first photon detection event when used to define the second-order quantum coherence function:

$$g^{(2)}(\tau) = \frac{\langle\hat{E}^{(-)}(t)\hat{E}^{(-)}(t+\tau)\hat{E}^{(+)}(t+\tau)\hat{E}^{(+)}(t)\rangle}{\langle\hat{E}^{(-)}(t)\hat{E}^{(+)}\rangle\langle\hat{E}^{(-)}(t+\tau)\hat{E}^{(+)}(t+\tau)\rangle}, \tag{2.84}$$

which is the quantum analog of the classical second order correlation function given in section 2.1.1. $g^{(2)}$ is an important quantity in the characterization of single photon sources. To make this clear, we investigate the second order auto correlation function a bit further by in particular comparing the expression for $g^{(2)}(\tau)$ at $\tau = 0$ in quantum theory to that which we have found in classical theory (eqn 2.44).

Just as we did for the classical case, we can evaluate the second-order quantum auto correlation function at $\tau = 0$:

$$g^{(2)}(0) = \frac{\langle\hat{E}^{(-)}(t)\hat{E}^{(-)}(t)\hat{E}^{(+)}(t)\hat{E}^{(+)}(t)\rangle}{\langle\hat{E}^{(-)}(t)\hat{E}^{(+)}\rangle^2}, \tag{2.85}$$

If we substitute for the operators of a single mode field (equations 2.70 and 2.69) we obtain:

$$g^{(2)}(0) = \frac{\langle\hat{a}^\dagger\,\hat{a}^\dagger\,\hat{a}\,\hat{a}\rangle}{\langle\hat{a}^\dagger\,\hat{a}\rangle^2}, \tag{2.86}$$

which can then be rewritten in terms of the number operator (eqn 2.64) after reorganization of the creation and annihilation operators using the commutation relation from eqn 2.54:

$$\begin{aligned} g^{(2)}(0) &= \frac{\langle\hat{a}^\dagger(\hat{a}\,\hat{a}^\dagger - 1)\,\hat{a}\rangle}{\langle\hat{a}^\dagger\,\hat{a}\rangle^2} \\ &= \frac{\langle\hat{n}^2\rangle - \langle\hat{n}\rangle}{\langle\hat{n}\rangle^2} \\ &= \frac{\langle(\Delta n)^2\rangle + \langle\hat{n}^2\rangle - \langle\hat{n}\rangle}{\langle\hat{n}\rangle^2} \qquad (2.87) \\ &= 1 + \frac{\langle(\Delta n)^2\rangle - \bar{n}}{\bar{n}^2}. \qquad (2.88) \end{aligned}$$

where in the second to last line we introduced the expression for the photon number variance $\langle(\Delta n)^2\rangle = \langle\hat{n}^2\rangle - \langle\hat{n}\rangle$. It is clear from eqn 2.88 that light with photon statistics characterized by $\bar{n} > \Delta n$ will return a

value of $g^{(0)}(0) < 1$, which, as we have seen in eqn 2.44, is not allowed in the classical regime. We will see in the next section that a photon number state corresponds to a mean photon number that is larger than the photon variance and a pure single photon state will even return a $g^{(2)}(0) = 0$. The range of allowed values in quantum theory is then:

$$g^{(2)}(0) \geq 0. \tag{2.89}$$

2.2. Classification of light according to its photon statistics

In the previous section, we have described how the quantum theory of light considers light to consist of indivisible quanta, or photons distributed among different quantum field states. This model allows us the investigate the photon statistics of light. Here we will give three examples of quantum states of light and how they each present a different photon number distribution. It will be shown that the photon distribution of the coherent state is a Poisson distribution. Moreover, it will be described how the coherent state is the quantum mechanical equivalent of a classical coherent monochromatic electromagnetic wave. For this reason, light is often classified according to how its photon statistics compare to the Poisson distribution. Thermal light will be given as an example of *super-Poissonian* light and photon number states as that of *sub-Poissonian* light.

2.2.1. Poissonian

A quantum state of light is not necessarily assigned a well defined number of photons: it can also be in a superposition of different number states. A coherent state, for example, is such a superposition of number states. It is defined a being an eigenfunction of the annihilation operator $\hat{a}\,|\alpha\rangle = \alpha\,|\alpha\rangle$ and can be expressed as:

$$|\alpha\rangle = e^{-\frac{1}{2}|\alpha|^2} \sum_n \frac{\alpha^n}{\sqrt{n!}} |n\rangle\,. \tag{2.90}$$

Looking at its average photon number:

$$\bar{n} = \langle\hat{n}\rangle = \langle\alpha|\,\hat{n}\,|\alpha\rangle = \langle\alpha|\,\hat{a}^\dagger\,\hat{a}\,|\alpha\rangle = |\alpha|^2, \tag{2.91}$$

and its photon number variance:

$$\begin{aligned}
\langle(\Delta n)^2\rangle &= \langle\hat{n}^2\rangle - \langle\hat{n}\rangle^2 && (2.92)\\
&= \langle\alpha|\,\hat{n}^2\,|\alpha\rangle - \langle\alpha|\,\hat{n}\,|\alpha\rangle^2 \\
&= \langle\alpha|\,\hat{a}^\dagger\,\hat{a}\,\hat{a}^\dagger\,\hat{a}\,|\alpha\rangle - |\alpha|^4 \\
&= \langle\alpha|\,\hat{a}^\dagger\,\hat{a}^\dagger\,\hat{a}\,\hat{a}\,|\alpha\rangle + \langle\alpha|\,\hat{a}^\dagger\,\hat{a}\,|\alpha\rangle - |\alpha|^4 \\
&= |\alpha|^2 = \bar{n}, && (2.93)
\end{aligned}$$

we find that for the coherent state, the fluctuations in photon number equal the mean photon number. We can further calculate the probability of finding n photons in the coherent state $|\alpha\rangle$:

$$\begin{aligned}
P(n) &= |\,\langle n|\alpha\rangle\,|^2 \\
&= |\,\langle n|\,e^{-\frac{1}{2}|\alpha|^2} \sum_{n'} \frac{\alpha^{n'}}{\sqrt{n'!}}\,|n'\rangle\,|^2 \\
&= |e^{-\frac{1}{2}|\alpha|^2} \sum_n \frac{\alpha^n}{\sqrt{n!}}\,\langle n|n'\rangle\,|^2 \\
&= |e^{-\frac{1}{2}|\alpha|^2} \sum_n \frac{\alpha^n}{\sqrt{n!}}\delta_{nn'}|^2 \\
&= e^{-|\alpha|^2}\frac{|\alpha|^{2n}}{n!} = e^{-\bar{n}}\frac{\bar{n}^n}{n!}, && (2.94)
\end{aligned}$$

where in the last step we used eqn 2.91. This is the Poisson distribution. From equation 2.88 we immediately find that for the coherent state $g^{(2)}(0) = 1$, obeying both the classical 2.44 and the quantum

2.89 regime. In fact, the coherent state is characterized by a constant second-order auto-correlation function $g^{(2)}(\tau) = 1$, reflecting the Poissonian nature of its photon statistics because, as mentioned earlier, $g^{(2)}(\tau)$ can be interpreted as the probability of detecting two photons a time τ apart. A constant $g^{(2)}(\tau)$ therefore implies that every interval τ between photon detections is equally likely to occur. Each photon detection event is therefore independent of the others. This is indeed characteristic of the underlying processes making up a Poissonian distribution.

The coherent state displays some remarkable properties. Apart from being an eigenstate of the annihilation operator and displaying a Poissonian photon number distribution, it is also an optimal state in the sense that it optimizes the uncertainty relation and therefore has the most well defined combined position and momentum as a quantum state could possible get. This can be shown by solving a variational problem posed by requiring a wavefunction to minimize the uncertainty relation $\Delta x \Delta p \geq \frac{\hbar}{2}$. This wavefunction expanded in a basis of number states is equal to eqn 2.90. Finally, the coherent state is regarded as "the most classical" a quantum state can get. This becomes tangible when looking at the expectation of the single mode electric field:

$$\begin{aligned}
\langle\alpha|\,\hat{\mathbf{E}}(\mathbf{r},t)\,|\alpha\rangle &= i\mathbf{A}\,\langle\alpha|\,\hat{a}^\dagger e^{-i\chi} - \hat{a}e^{i\chi}\,|\alpha\rangle && (2.95)\\
&= i\mathbf{A}\,\langle\alpha|\,\hat{a}^\dagger\,|\alpha\rangle\,e^{-i\chi} - \langle\alpha|\,\hat{a}\,|\alpha\rangle\,e^{i\chi} && (2.96)\\
&= i\mathbf{A}|\alpha|(e^{-i(\chi+\theta)} - e^{i(\chi+\theta)}) && (2.97)\\
&= 2\mathbf{A}|\alpha|\sin(\chi+\theta), && (2.98)
\end{aligned}$$

where for sake of brevity we have used $\chi = \mathbf{k}\cdot\mathbf{r} - \omega t$ and $\mathbf{A} = -\mathbf{e}(\hbar\omega/2\epsilon_0 V)^{(1/2)}$, and we have written $\alpha = |\alpha|e^{i\theta}$. We find that the expectation value simply corresponds to a classical single mode electric field. The coherent state is therefore suitable as a benchmark in the classification of light according to its photon statistics.

2.2.2. Super-Poissonian

A quantum state of light for a single-mode radiation field at frequency ω in thermal equilibrium with a heat bath of temperature T is given by

$$\hat{\rho} = \sum P_n\,|n\rangle\,\langle n|\,, \tag{2.99}$$

where it is known from statiscal mechanics that P_n, the probability that the mode is excited in its nth level (or holds n photons), is given the Boltzmann factor:

$$P(n) = \frac{1}{Z}e^{-\hbar\omega n/k_B T}, \tag{2.100}$$

with Z the partition function $Z = \sum exp(-\hbar\omega n/k_B T)$. This is the Bose-Einstein distribution.
The average photon number is:

$$\begin{aligned}
\bar{n} = \langle\hat{n}\rangle &= Tr(\hat{n}\hat{\rho}) = \sum\langle n|\,n\hat{\rho}\,|n\rangle\\
&= \sum P(n)n = \sum\frac{1}{Z}n\left(e^{-\hbar\omega/k_B T}\right)^n\\
&= -\frac{1}{Z}q\frac{\delta}{\delta q}\sum q^n \quad , q = e^{-\hbar\omega/k_B T}\\
&= \frac{q}{1-q}\\
&= \frac{1}{e^{\hbar\omega/k_B T} - 1}, && (2.101)
\end{aligned}$$

where in the second to last step both Z and the summation over n are recognized as being geometric series and subsequently expressed in their closed form. We can use eqn 2.101 to rewrite eqn 2.100 in terms of $\bar{n}$:

$$P(n) = \frac{\bar{n}^n}{(1+\bar{n})^{n+1}}. \tag{2.102}$$

Looking at the variance of the photon number:

$$\begin{aligned}\langle(\Delta n)^2\rangle &= \langle\hat{n}^2\rangle - \langle\hat{n}\rangle^2 \\ &= \bar{n} + 2\bar{n}^2 - \bar{n}^2 = \bar{n} + \bar{n}^2,\end{aligned} \tag{2.103}$$

which is always larger than the variance corresponding to the Poissonian distribution of the coherent state: $\Delta n > \sqrt{\bar{n}}$ hence a thermal light field is classified as super-Poissonian.

For super-Poissonian light we find (eqn 2.88

$$g^{(2)}(0) \geq 1. \tag{2.104}$$

which is, like the coherent state, also in accordance with classical limitations 2.44. Classicaly it can be shown that $g^{(2)}(\tau) \leq g^{(2)}(0)$. For thermal, or chaotic light in particlar, $g^{(2)}(\tau)$ is exclusively smaller than its value at $\tau = 0$. The highest probability is therefore to detect photons simultaneously (or, in practice, with the second-order auto-correlation fuction being a smooth monotonic function, the smaller interval τ, the higher the probability): photons tend to bunch together. Equation 2.104 is a characteristic of photon-bunching.

2.2.3. Sub-Poissonian

Finally, as an example of sub-Poissonian light, we will briefly look at the rather straightforward photon statistics of the photon number state, or Fock state.

The probability distribution is simply a delta peak

$$P(n) = |\langle n|m\rangle|^2 = \delta_{nm}. \tag{2.105}$$

For which the mean photon number and variance are just as easily evaluated:

$$\bar{n} = \langle\hat{n}\rangle = \langle n|\,\hat{n}\,|n\rangle = n; \tag{2.106}$$

and,

$$\langle(\Delta n)^2\rangle = \langle\hat{n}^2\rangle - \langle\hat{n}\rangle^2 = n^2 - n^2 = 0. \tag{2.107}$$

Clearly, $\Delta n < \sqrt{\bar{n}}$, classifying a photon number state as sub-Poissonian. When we evaluate $g^{(2)}(0)$ for the Fock state using eqn 2.88, we find that it will return non-classical values:

$$g^{(2)}(0) = 1 + \frac{(\Delta n)^2 - \bar{n}}{\bar{n}^2} = 1 - \frac{1}{\bar{n}} < 1. \tag{2.108}$$

An ideal single photon state for which $\bar{n} = n$ gives $g^{(2)}(0) = 0$ and is theoretically the only state that will produce $g^{(2)}(0) < 1/2$. The consensus therefore is that measurement of $g^{(2)}(0) < \frac{1}{2}$ is indicative of single photon emission. A measurement of $g^{(2)}(0) < \frac{1}{2}$ is related to a phenomenon called photon anti-bunching, in which photons tend to spatially separate from one another.

The photon number distributions of each of the examples given in this section are plotted in figure 2.2.

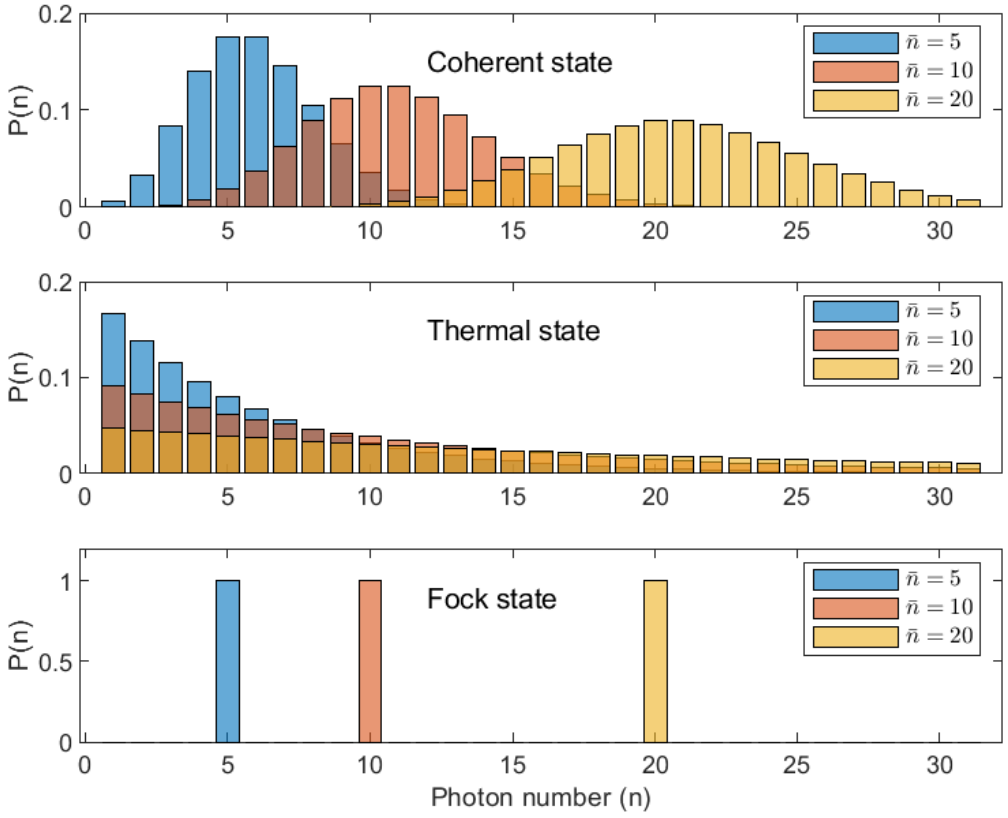

Figure 2.2: Histograms displaying different photon number distributions for three values of mean photon number $\bar{n}$. From top to bottom: Poisson distribution, super-Poissonian distribution, sub-Poissonian distribution.

2.3. Hanbury Brown and Twiss experiment

Having established that the second-order auto-correlation function can be used to determine whether or not a light source is a single photon emitter we will discuss in this section how $g^{(2)}(\tau)$ is evaluated experimentally. We have introduced $g^{(2)}(\tau)$ in section 2.1 as being related to the probabililty of detecting a pair of photons a time τ apart. If we were to have access to ideal photodetectors, measuring $g^{(2)}(\tau)$ would be as straightforward as recording photon detection events with a single detector and organizing them into time bins. Single photon detectors however, as we will see in section 2.4.1 are subject to *dead times* during which the detector is recovering from a photon detection event making it blind to any other incoming photons. The single-photon avalanche diodes used in this work for instance have a dead time of around $35\,\mathrm{ns}$. Coincidence events within the 'coherence/life' time of typical single-photon sources which is in the order of a few nanoseconds, would therefore not be registered. The Hanbury-Brown and Twiss interferometer [8] gets around this technical problem by using two photodetectors instead of one (figure 2.3).

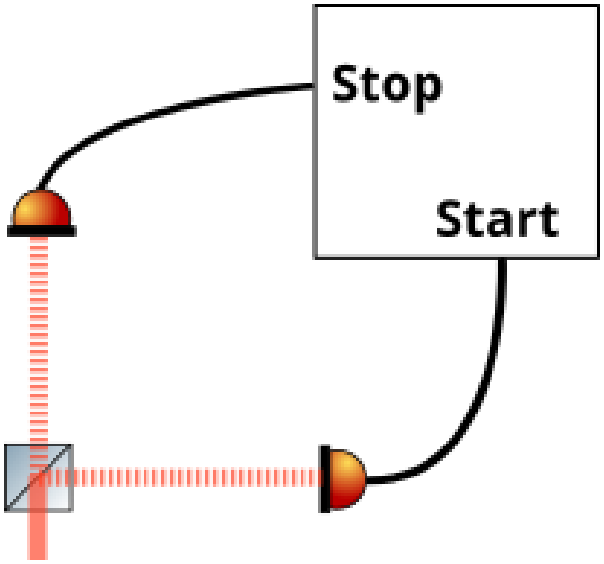

Figure 2.3: A schematic representation of the Hanbury-Brown and Twiss interferometer, which is used to measure the second-order coherence of light. Light is incident on a 50:50 beamsplitter after which it is diverted towards two separate detectors.

The HBT setup consist of a two detectors located at the output ports of a 50:50 beamsplitter. The photons incident on both detectors are counted and in particular, the time delay between detection events at detector 1 and at detector 2 are recorded. These coincidence events are then displayed in a histogram, reflecting the second-order auto-correlation function. A dip in the histogram at $\tau = 0$ would indicate anti-bunching. In light of the HBT setup, another way of interpreting $g^{(2)}() = 0$ corresponding to ideal single photon emission is to envision the wavefunction of a single photon number state to be diverted by the beamsplitter towards both detectors, but upon measurement is forced to collapse at only one of the detectors. It will take at least a time on the order of the life time of the single photon source before either of the detectors is exposed to a second photon. The broadening of the $g^{(2)}(\tau)$ dip corresponding to a single photon source can be related to the lifetime of the source and the excitation pump rate expressing the probability of re-excitation and emission of a second photon in a short time interval. note :In the case of a simple start-stop timer, the stop pulse is often purposely delayed from the start, so that negative delay data (τ < 0) can be recorded.

2.4. Single photon sources and detection

In this section a brief overview is given of the state of the art of single photon technologies. A selection of common single-photon detectors and single-photon sources are briefly described.

2.4.1. Single photon detectors

A single photon in the visible range corresponds to an energy of around 10^{-19} Joules. As detecting such miniscule energy quantas is far from trivial, it is appropriate to dedicate this section to single photon detection. Here a selection of commonly used single photon detectors (SPDs) is listed and each is briefly described. Most SPDs rely on the conversion of a photon that is incident on the active area of the detector into an electrical signal of some sort. This often involves very high gain and low noise as the energy of a single photon is so small. The detectors that are used in the current work are the Superconducting Nanowire Single Photon Detector (SNSPD) and the Avalanche Photodiode (APD).
In describing and characterising single photon detectors, the following terminology is used:

- **System detection efficiency**: The probability that a photon provided to the detector leads to a detection event (this regards the detection system in its entirety and therefore is also affected by coupling losses for example).
- **Quantum efficiency**: The fraction of photons reaching the active area of the detector that produce current carriers.
- **Timing latency/ detection time**: The time between the moment of incidence of a photon and the moment of signal detection.
- **Jitter**: Variance in the distribution of timing latency.
- **Dark counts**: An unwanted detection pulse that is not initiated by a photon.
- **After Pulsing**: A second, unwanted detection event triggered by an already measured photon.
- **Dead time**: The time a detector spends in its recovery phase during which it is insensitive to any incident photons.

Photomultiplier Tube

The first detector demonstrated to be capable of single photon detection [9] and therefore the oldest and most long established photon counting technology is the photomulitplier tube (PMT). The PMT is a vacuum device that consists of a photon cathode and anode sandwiching a series of dynodes (see figure 2.4). By the photoelectric effect, an incident photon sparks off the release of an electron from the cathode. An applied electric field accelerates the electron towards the first dynode, which on collision, releases secondary electrons. These electrons are then accelerated towards the second dynode, which in turn introduces even more electrons into the system. This avalanche-like amplification process continues until the electrons reach the anode. A typical PMT amplifies the original signal by a factor of $10^6 - 10^8$, which by then is easily detectable.

When properly designed, a PMT has a timing latency of a few nanoseconds, a typical jitter of 300 ps and dark count rates as low as 100 Hz ([10]). PMTs can be designed to have large active areas and cover a broad spectral range of $114-1700$ nm. Their limited maximum efficiency of around 40% however does not meet the requirements of most modern applications. Moreover, its reliance on vacuum tube technology limits their lifetime, reliability and scalability,

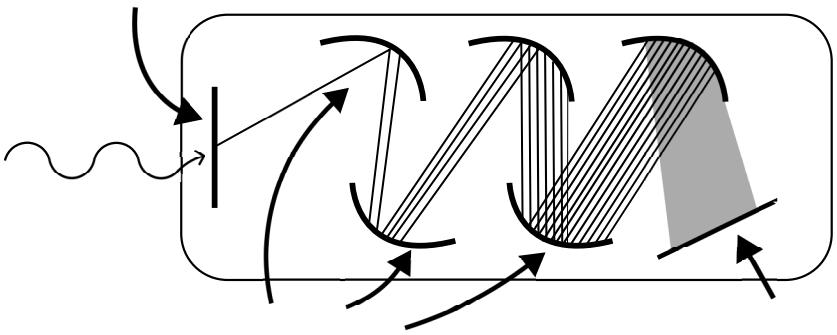

Figure 2.4: Schematic of a photomultiplier tube. A photon incident a cathode triggers the emission of a photoelectron that is amplified via a series of dynodes before it is detected.

Single-Photon Avalanche Photodiode

Similar to the PMT, the workings of a semiconductor based single-photon avalanche photodiode (SPAPD) [11] rely on the amplification of an initial photoelectron. More accurately, a photon is incident on the depletion region of a p-n junction, produces an electron-hole pair and instead of the eletrons being discretely multiplied via a series of dynodes, continuous charge multiplication caused by impact ionization takes place due to a applied reverse bias voltage accross the semiconductor lattice. The magnitude of the bias voltage is slightly higher than the diode's breakdown voltage, making that the diode is operating in 'Geiger-mode': the detector either 'clicks', on the incidence of one or more photons, or it does not. The charge multiplication continues untill it saturates at a self-sustaining current typically limited by an external circuit. In order to be able to detect a subsequent photon, the device is reset by a quenching circuit.
Charge carriers can occupy so called 'trap-sites' which must be allowed time to depopulate to prevent after pulsing. As a result, APD dead times are relatively long, ranging from tens of nanoseconds up to $10\ \mu$s. The photon wavelength range within which an APD operates depends on the semiconducting material used. Lower band-gap materials will be capable of detecting lower energy photons. For example, silicon APDs cover a spectral range of $300 - 1100$ nm, whereas germanium based APDs can be used between $800 - 1600$ and InGaAs APDs for wavelengths within spectral range of 900 to 1700 nm. Depending on the semiconducting material and the wavelength of incoming photons, APDs can have detection efficiencies much higher than PMTs (85% for Si APDs in the visibile range). However, dark count rates and jitter are typically slightly higher than those of the best performing PMTs.

The fundamental trade-off of geiger-mode avalanche photodiodes is detection efficiency versus dark count rates. Operating at higher bias voltage will improve detection efficiency but will at the same time also increase dark count rates. Dark count rates can be improved upon by for example by operating at lower temperatures or by decreasing the size of the active area of the detector. Another trade-off occurs between detection efficiency and jitter. A thinner semiconductor absorption layer will decrease jitter but so will it decrease detection efficiency.

The APDs used in the current work are the SPCM-AQRH-TR single photon counting modules manufactured by Excelitas Tecnologies: silicon APDs with a quantum efficiency at $650\,\mathrm{nm}$ of 75%, a maximum dark count rate of $1500\,\mathrm{s}^{-1}$, a probability of 1.0% of afterpulsing and a typical dead time of $35\,\mathrm{ns}$. For a full specification see the datasheet of the manufacturer [12].

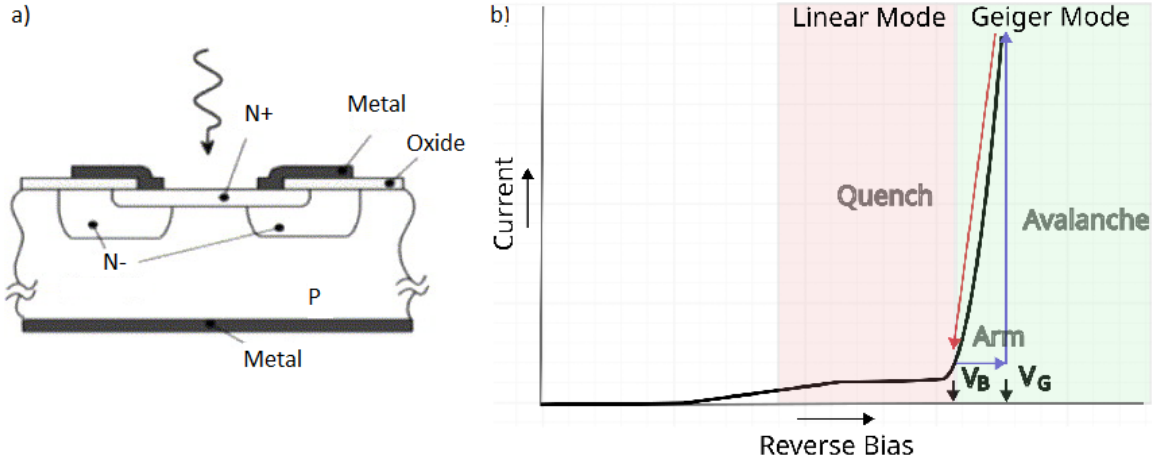

Figure 2.5: a) Schematic of a single-photon avalanche diode. An incident photon triggers the release of an electron-hole pair. The charge carriers are accelerated by an applied bias causing a 'charge-carrier-avalanche' which reaches the cathode and subsequently leads to a detection event. Source: [11] b) Voltage curve of a an avalanche photodiode. Two regimes of operation are distinguished based on the applied bias voltage: linear and Geiger mode. In Geiger mode operation, the device is biased slightly above breakdown (ARM, V_G). Upon photon incidence, a charge carrier avalanche is triggered (AVALANCHE). After detection, the avalanche is quickly quenched (QUENCH) and the device is brought back into idle mode (V_{BR}), ready to detect a next photon.

Superconducting Nanowire Single Photon Detector

A superconducting nanowire single photon detector (SNSPD) consist of a superconducting material (e.g. Niobium Nitride (NbN), Niobium Titanium Nitride (NbTiN), Tungsten silicide (WSi), Magnesium dibiroide (MgB_2)) that is shaped by e-beam lithography into a meandering nanowire which makes up the active area of the detector. A constant current is sent through the nanowire and the detector operates at a temperature just below its critical temperature. Absorption of a only a single photon then increases the temperature sufficiently to locally break superconductivity. This results in an increment in resistance which diverts the current diverts the current towards an amplification circuit creating a measurable voltage pulse. After photon absorption the SNSPD quickly recovers to its superconducting state and is ready to detect the next photon.

Just like avalanche photodiodes, a trade-off occurs between detection efficiency and dark count rate. A current closer to the critical current means better efficiency, but will also produce more dark counts. SNSPDs are particularly efficient at detecting photons in the visible to mid-infrared range (98% or higher). Overall this detector type has a relatively low dark count rate ($10 \times 10^{-3}\,\mathrm{s}^{-1}$), a short dead time and a timing jitter below $3\,\mathrm{ps}$.

The SNSPD used in this work are NbTiN structures that operate at a temperature below $2.9\,\mathrm{K}$. Its system detection efficiency has been shown to reach near-unity values up to $99.5 \pm 2\%$ [13] in the spectral range $1290 - 1500\,\mathrm{nm}$. The dark count rate is lower than $10\,\mathrm{s}^{-1}$ and the dead time below $97\,\mathrm{ns}$. A full specification is given in [14].

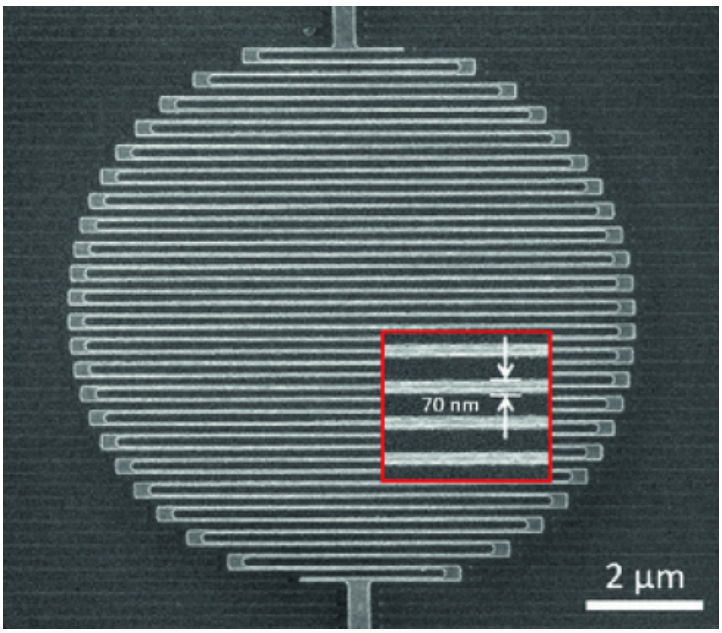

Figure 2.6: Sanning Electron Microscope image of a meandering superconducting nanowire making up the active area of a SNSPD. The inset displays a magnification of the 70-nm-wide nanowires. Source: [15]

2.4.2. Single photon sources

Single photon sources can be broadly categorized as being either probabilistic or deterministic. Probabilistic 'single-photon' sources are actually based on two photon emission, where detection of one of the two photons heralds the other as the single-photon emission. An example of a probabilistic SPE is Spontaneous Parametric Down Conversion (SPDC)[16], which is a quantum phenomenon that occurs when high energy laser light is sent through a nonlinear crystal (a crystal in which the induced dipole moment depends nonlinearly on the electric field). A photon in the incident beam hereby splits spontaneously into a pair of lower energy photons in accordance with momentum and energy conservation. The probabilistic nature of SPDC is due to the fact that it is driven by random vacuum fluctuations. Another example of a probabilistic SPE is sponaneous four-wave mixing [17]. Photon-pair based heralded single-photon sources enable the production of pairs of polarization-entangled photons which makes them particularly interesting for quantum information applications. They are also the most widely used SPE in quantum-enabled measurement applications and single-photon detector calibration. [16]
Many applications however require on-demand generation of a single-photon. Most deterministic single-photon sources involve a multi-level energy system and rely on similar principles of operation: charge carriers are brought into an excited state by optical or electrical triggers which after a characteristic lifetime will emit a single photon upon relaxation towards lower energy levels. An ideal two-level system is able to produce pure, sub-Poissonian single photon states. Technically, realizing such sources is therefore a matter of isolating and controlling a single multi-level system. As an example, an individual atom is such a multi-level system (figure 2.7. The first demonstration of single photon emission involved excitation of sodium atoms [18]. The downside of using atoms as single photon emitters is that it currently require highly complex architectures involving e.g. ultra high vacuum and potential lattices created by laser interference in which atoms are trapped. This brings us to the typically more robust solid-state single photon sources.

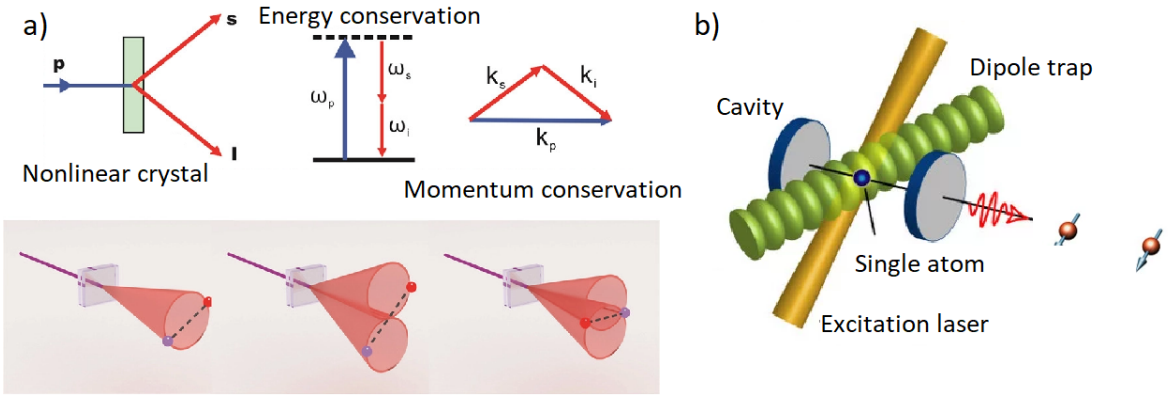

Figure 2.7: Schematic representation of single-photon producing processes. a) Probabilistic Spontaneous Down Conversion. A pump laser (P) is incident on a nonlinear crystal, producing a pair of photons: a signal (S) and idler (I) photon. One of them (I) heralds the presence of the other (S). To top three images illustrate energy and momentum conservation. The bottom three depict three different types of SPDC, from left to right: all three photons share the same polarization (type 0), (S) and (I) photon have the same polarization but are orthogonal to (P) (type I), (I) and (S) have perpendicular polarizations. Source: [16]. b) Schematic representation of a single atom single-photon source. The atom is trapped in an optical dipole trap and excited by a pump laser. A cavity enhances collection efficiency. Source [19]

The first example of a solid-state quantum emitter are color centres in three-dimensional bulk crystals. Some of the most thoroughly studied are color centers in diamond, silicon carbide (SiC) and zinc oxide (ZnO) [20]. Color centers are luminescent point defects in crystal lattices that determine the color of crystals (hence the naming). The defects can either occur naturally, or be artificially introduced by ion implementation and subsequent annealing. When their density is low enough, a single color center can be isolated and individually addressed. If in addition the electronic ground state and excited states lie well within the bandgap of the host crystal, color centers can make for stable single photon sources even at room temperature. The great diversity among the many different color centers make them a hot topic of research. The advantages of color centers are that they typically are robust a highly stable SPEs. However, high refractive index host materials put limits on single-photon extraction rates and many color centers exhibit fluorescence that is largely phonon shifted, making it hard to produce

indistinguishable single-photons. Successful attempts have been made to enhance extraction rates e.g. point defects have been encapsulated by solid immersion lenses [21], and resonating cavities [22]. Operation at cryogenic temperatures significantly reduces phonon-coupling, producing narrower single-photon emission lines.

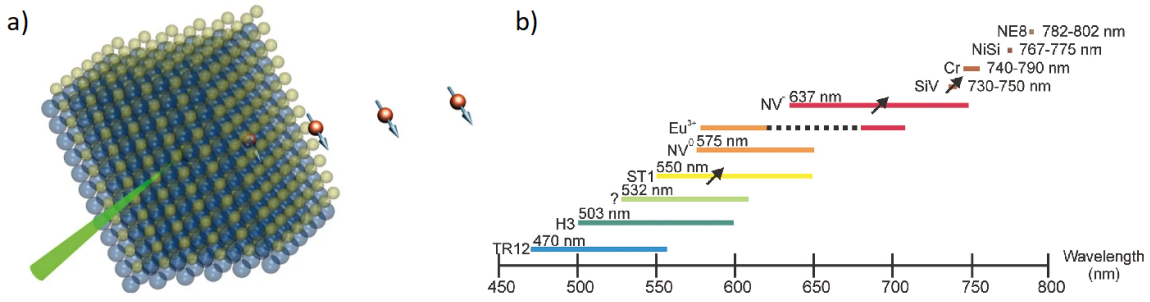

Figure 2.8: a) A schematic depiction of a color center in a bulk crystal. Laser light (green) is used to bring the point defect into an excited state. Upon relaxation towards lower energy levels single photons are emitted. b) A graph displaying a selection of single photon emitting color centers in diamond. The wavelength label of each emitter indicates the positions of the observed zero-phonon-line while the length of the colored bars represent the approximate width of the emission spectrum. Black arrows indicate controllable spin properties. Source: [20],

A second example of a solid-state single-photon source is the semiconductor quantum dot. A quantum dot consists of a tiny section of smaller-band-gap semiconductor that is embedded in a larger-band-gap semiconductor. In a bulk semiconductor, the electrons in the conduction band can be assumed to be free to move in all three dimensions and only to be confined by the boundaries of the semiconductor. The electrons can take on any energy above the band-gap energy. When one or more dimensions are reduced to a size comparable to the de Broglie wavelength of the electron, which is on the order of $10nm$ for typical semiconductors at room temperature, the system becomes a low-dimensional structure (LDS) and the density of states is affected.

A denisity of states analysis involving solving Schrödinger's equation for models of low-dimensional systems (infinite potential well) reveals the effects of this quantum confinement. In figure (2.9) a sketch of the density of states as a function of energy is shown for a bulk semiconductor and for the three different LDSs. As is apparent from looking at the figure, increased confinement of charge carriers leads to sharper quantization of energy levels. Most dramatically, charge carriers in quantum dots can only take on discrete values. Because the discretized nature of its density of states resembles that of an atom, solid state quantum dots are often called artificial atoms. Electrons can be excited on demand through optical or electrical excitation. Subsequent recombination of an electron-hole pair triggers the emission of a single photon with a wavelength corresponding to the difference between energy levels.

The QDs that were initially planned to be used in this thesis are semiconductor III-V compounds (more specifically, indium arsenide phosopide (InAsP) and embedded in a pure wurtzite (InP) nanowire. III-V QDs have high refractive index compared to air causing much of the emitted photons to be reflected back into the high index substrate at the semiconductor-air interface limiting the extraction efficiency. By embedding the QD in a nanowire with optimized geometry, the direction of the QD emission is largely controlled enhancing the extraction efficiency. Moreover, the nanowire is engineered such that single photons are emitted in a single spatial mode (gaussian). The QDs have not been measured upon due to problems with the cryostat. The following solid-state single photon sources however are used in the experiments and therefore treated in more detail.

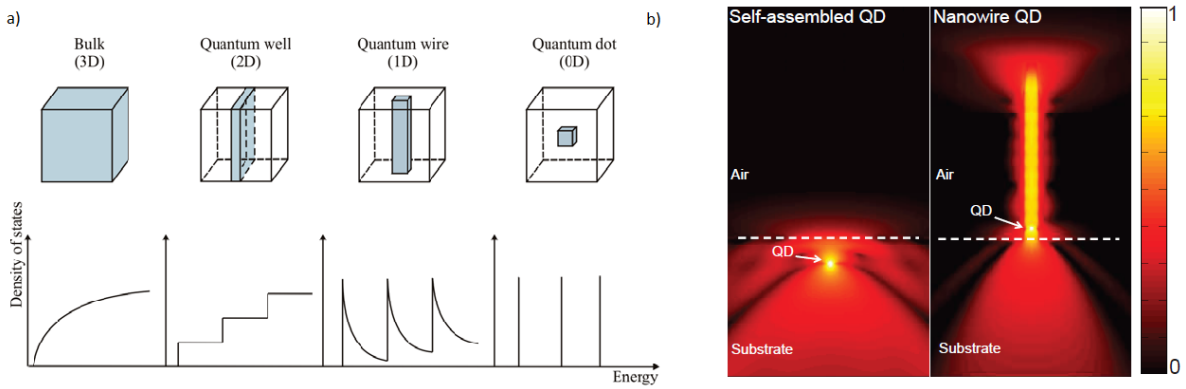

Figure 2.9: a) Density of states for different low dimensional systems. As free motion of charge carriers is restricted more, energy levels get quantized sharper. In quantum dots, charge carriers are confined to a discrete number of energy levels. Source: [23]. b) Comparison between the electric field emission profile of a self-assembled QD and a nanowire QD showing a much higher photon extraction efficiency for a QD in nanowire. Figures are obtained from numerical simulation. Source: [24]

Two-dimensional semi-conductor materials

Since the discovery of single-layered graphene [25], significant progress has been made in fabrication and application of various two-dimensional semi-conductor materials. 2D materials, transition metal dichalcogenides (TMDs) in particular, have long been relevant in optics related research due to their favorable optical properties [26]. It was not until only recently however that 2D were shown to be able to hold single-photons emitters[27].

SPEs embedded in 2D materials are interesting for a number of reasons. Most solid-state single-photon emitters are embedded in high refractive index three dimensional materials limiting integration ability and photon extraction efficiency. SPEs confined in atomically thin on the other hand, offer near unity extraction efficiencies as emission is much less likely to be reflected back into its host material. In addition, it has been demonstrated that their emission properties are controllable through a number of different methods [28] [29] [30]. For instance, being atomically thin, 2D materials are highly malleable, which allows for tunability of emission wavelength and intensity by strain engineering [31]. Moreover, 2D materials offer advantages by allowing for effective on-chip integration [32] and by being readily combined to form heterostructures benefitting from advantages of various different materials.

Two-dimensional materials can be created by various methods of fabrication. For a review on 2D fabrication techniques the reader is referred to [32]. Whilst the origin of single-photon emission in 2D materials remains a subject of debate, it is generally thought to originate from localized charge carrier potential traps induced by lattice point defects. Point defects can be artificially introduced by annealing and electron beam irradiation.

Tungsten Diselenide (WSe_2)

Single-photon emission in a 2D material was first demonstrated in 2015 by three groups simultaneously and involved monolayer tungsten-diselenide (WSe_2) cooled down to cryogenic temperatures [33] [34] [27]. WSe_2 is a semiconductor material in the group-VI transition metal dichalcogenides, with a band-gap of 1.7 eV in monolayer form [35]. Here we will highlight some of the results obtained by one of the three groups: Yu-Ming He et. al. [27].

Figure 2.10 (a) shows a photoluminescence (PL) map for 721 nm centered emission lines of a WSe_2 monolayer, displaying the locations and indicating the highly localized nature of the emitters. Figure 2.10 (b) shows a PL spectrum of one of the emitters. The insets compare emission from the localized excitons in point defects and emission from delocalized instrinsic monolayer excitons, which originates from carrier transitions across the WSe_2 direct band-gap. The much sharper single-photon spectral lines are redshifted compared to the monolayer exciton emission, demonstrating that the energy of the single-photon source lies within the WSe_2 bandgap. PL spectra of 92 different localized emitters yield an average linewidth of ~ 0.06nm.

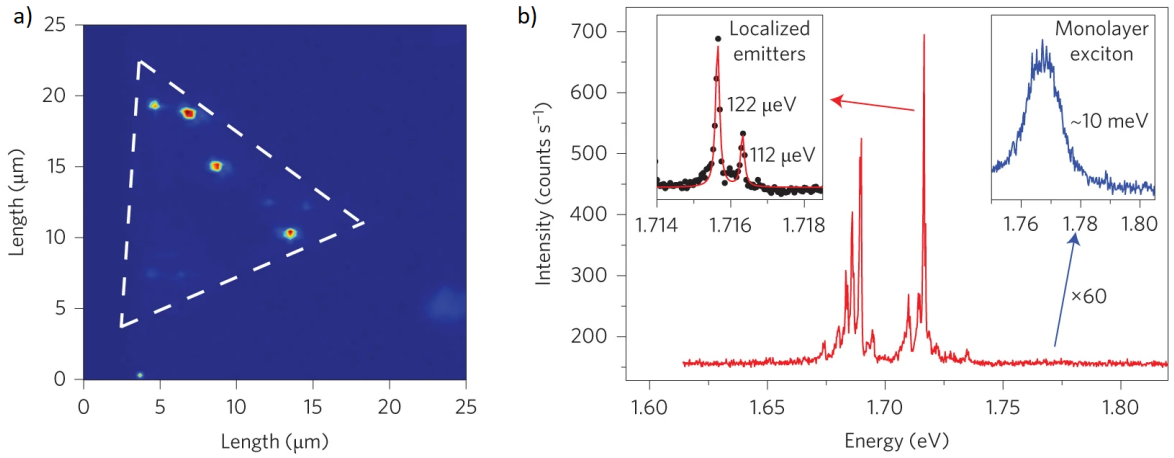

Figure 2.10: a) PL-intensity map of narrow emission lines centered at 721nm over an area of 25×25m. The dashed line indicates the boundaries of the WSe_2 monolayer. b) PL spectrum of localized emitters displaying sharp emission peaks red shifted compared to emission from delocalized valley exciton. The left inset is a higher resolution spectrum of the highest intensity peak showing its doublet nature, The right inset is an enlarged spectrum of the monolayer valley exciton emission, which is about 500 times lower in intensity under the continuous-wave 637nm laser excitation. Source: [27]

Figure 2.11 (a) shows a second-order auto-correlation measurement of PL emission of the highest intensity peak in figure 2.10(b). A value of $g^{(2)}(0) = 0.14 \pm 0.04$ is extracted from the data, indicating strong photon-antibunching. An excitation power versus intensity plot demonstrates that the emitter reaches a point of saturation at high enough excitation energy (2.11 (b)). The single-photon emission is thought to originate from neutral excitons trapped in anisotropic confining potentials from defects in the monolayer.

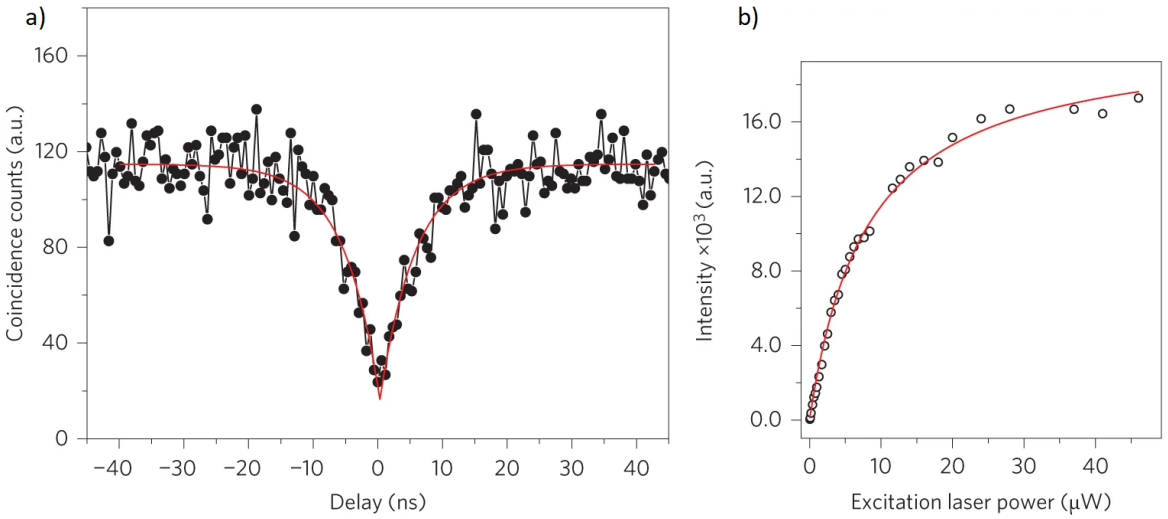

Figure 2.11: a) Second-order autocorrelation measurement of the PL emission of the highest intensity peak in figure 2.10 under a 6.8 W continuous wave laser excitation at 637 nm. From the fit (red line) $g^{(2)}(0) = 0.14 \pm 0.05$ is extracted. b) Saturation curve related to the PL emission of the same peak as (a). Source: [27]

Hexagonal Boron Nitride (hBN)

Shortly after the discovery of quantum emitters in WSe_2, a second material, namely the semiconductor hexagonal Boron Nitride (hBN) was demonstrated to have the capacity of holding single-photon emitters in two-dimensional structure [36] . Similarly to WSe_2, hBN SPE is thought to originate from localized potential traps induced by lattice point defects and impurities. hBN is a promising candidate for a new generation quantum emitter due to its chemical stability and large 6 eV band-gap [37] which is comparable to the band-gap of highly stable materials diamond and silicon carbide. Whereas WSe_2 requires operation at cryogenic temperatures, the large band gap of hBN allows stable single-photon emission at temperatures up to 800 Kelvin [38]. hBN has been shown to hold bright quantum emitters across the visible, near infrared [39] and even UV spectral ranges [36].

Figures 2.12 and 2.13 highlight some of the results of Toan Trong Tran et. al.[39]. Emitters are categorized in two groups based on their zero-phonon lines (ZPLs) and phonon-side band (PSB) spectral shapes. The ZPL is mainly determined by the intrinsic difference in energy levels between excited state and ground state. PSBs are caused phonon coupling of charge carriers. Group 1 consists of emitters with ZPL below 656 nm and the emitters in group 2 have ZPLs above 673 nm. Group 2 emitters have narrower, more symmetric ZPLs and weaker PSBs than the emitters of group 1 (figure 2.12 (b)). The asymmetry in ZPL of emitters in group 2 is hypothesized to be caused by phonon interactions.

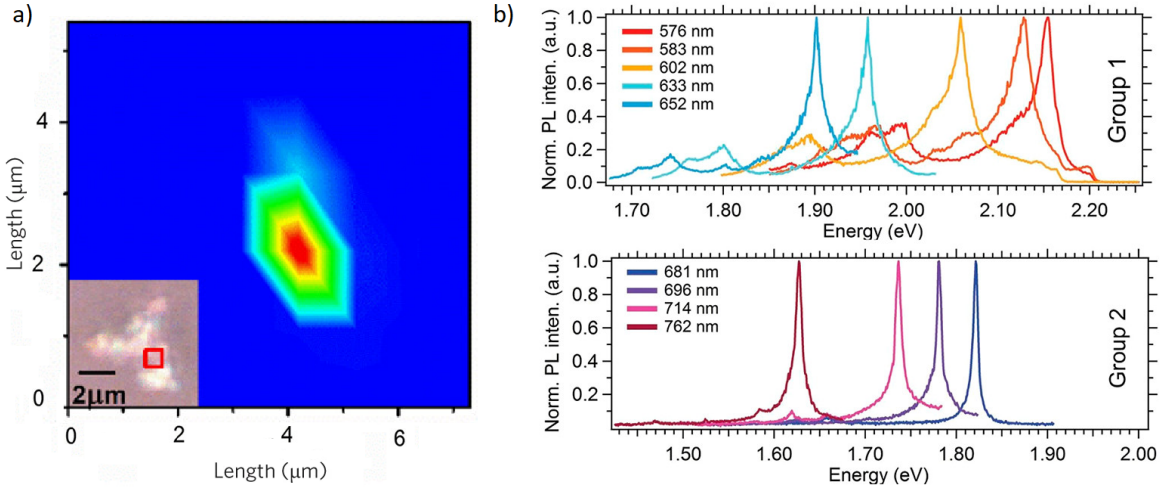

Figure 2.12: a) PL map of a hBN nanoflake. Inset: optical microscope image where red square indicates the location of a defect. Source: [31] b) PL spectra of eight different emitters in hBN. A distinction is made between group 1 emitters (top) and group 2 emitters (bottom). The five group 1 emitters and exhibit relatively broad and assymetric ZPLs and contain strong doublet PSBs. The four lower energy group 2 emitters have narrower, more symmetric ZPLs and weaker PSBs. Source: [39]

Second-order autocorrelation measurements are performed with a HBT interferometer on one representative emitter from each group (figure 2.13(a)). Both curves display anti-bunching, and a $g^{(2)}(0) < 0.5$ proofs the quantum nature of the emitters. The authors have analyzed the emitters in the frame of an extended three level system [40], involving a $g^{(2)}(\tau)$-fit of the form

$$1 - (1+a)e^{-\frac{|\tau|}{\tau_1}} + ae^{-\frac{|\tau|}{\tau_2}}, \tag{2.109}$$

where τ_1 is the emission lifetime and τ_2 is the metastable state lifetime which were found to be dependent on excitation power. $g^{(2)}(\tau)$ was measured as a function of excitation power and τ_1^0 and τ_2^0 were found by extrapolating the data to zero excitation power yielding values of $\tau_1^0 = 3.3$ and 8.1 ns and $\tau_2^0 = 88.6$ and 1.2 ns for the group 1 (633 nm) and group 2 emitter (714 nm) respectively, in good agreement with direct lifetime measurements performed. Similarly to the WSe_2 emitters of the previous section, the emitters are shown to reach a point of saturation in the intensity versus excitation power curve in figure 2.13(b). The data were fit using $I = I_\infty P/(P + P_0)$ where I_∞ and P_0 are the emission rate and excitation power at saturation.

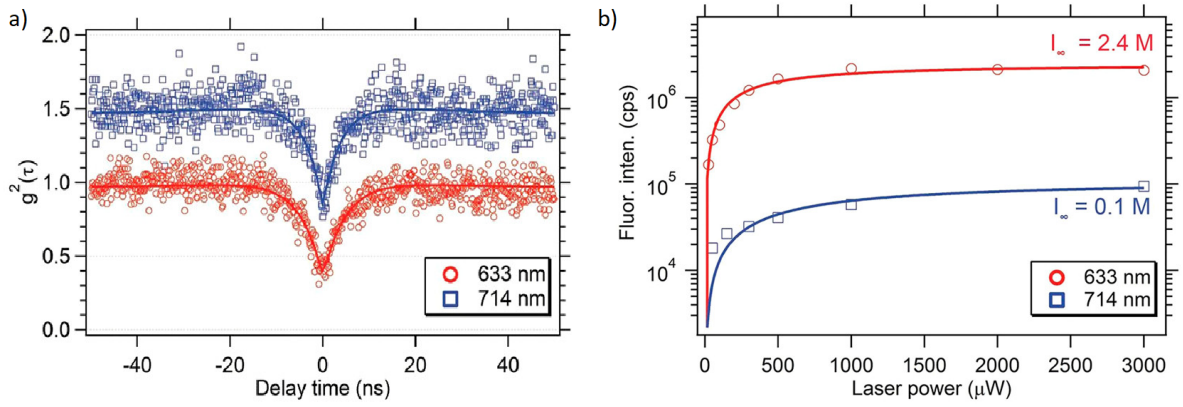

Figure 2.13: a) Second-order autocorrelation measrements of a group one (633 nm, red) and a group two (714 nm, blue) emitter, acquired using a sub-bandgap 300 W CW 532 nm excitation laser. Both display photon anti-bunching. From a three-level fit values $g^{(2)}(0) = 0.39$ and $g^{(2)}(\tau) = 0.34$ respectively are extracted proving that emission originates from point defects acting as single-photon emitters. Fluoresence saturation curve fitted by a three-level model. Saturation is reached at a power of $P_0 = 310$W and $P_0 = 770$W respectively. The corresponding maximum emission rates are $I_\infty = 2.4 \times 10^6$ and $I_\infty = 0.1 \times 10^6$ counts/s respectively. Source: [39]

2.4.3. Emission line broadening

Even though the energy separation between two energy eigenstates in a multi-level system is of a definite fixed value, single-photon emission is typically not monochromatic. In this section we briefly cover two line broadening mechanisms that single-photon emission is subject to: natural broadening and environmental broadening.

The cause for natural linebroadening is the uncertainty principle. The finite lifetime of the excited state leads to broadening of the spectral line in accordance with the energy-time uncertainty principle:

$$\Delta E \Delta \tau \geq \hbar, \tag{2.110}$$

where ΔE is the energy uncertainty of the transition, which translates into the width of an emission line, and τ is the exciton lifetime. Therefore, the linewidth is subject to a theoretical minimum wich is determined by the lifetime of the emitting exciton. By taking a fourier transform of a pulse of light that decays with τ, we obtain the following lineshape function [41]:

$$L(\lambda, \lambda_0, \gamma) = \frac{\gamma^2}{\gamma^2 + 4(\lambda - \lambda_0)^2} \tag{2.111}$$

where λ is the emission wavelength λ_0 the peak wavelength and γ the full-width half maximum of the line, Equation 2.111 is called a Lorentzian lineshape and is the characteristic shape of a naturally broadened emission line.

In practice, lines are wider than their allowed theoretical minimum. This is because there are more broadning mechanisms at play. One of such is environmental broadening, which is relevant in our discussion of solid-state SPEs. Environmental broadening occurs when excitons transition to lower energy levels without emission of a photon (non-radiative transition). Exictons can for instance get rid of their energy by emitting phonons, which can be interpreted to be spacial excitations of the crystal lattice, atomic vibrations or simply as the generation of heat, The result of such non-radiative transition is that the effective life-time of the exciton shortens. A shorter lifetime leads to a wider spread in photon energy (eqn 2.110). Phonon-coupling is reduced by lowering temperatures. Narrower lines are therefore often produced by cooling emitters down.

As a final note: in general, emitters can also be subject to inhomogeneous line broadening mechanism, having to do with an ensemble of emitters (e.g. atoms, molecules etc.) each behaving differently, causing them to contribute to different parts of the spectrum. Inhomogeneous mechanisms are therefore less relevant when considering single-photon emission, as there is often only a single emitter addressed. Inhomogeneous line broadening tends to produce Gaussian shaped spectra.

Bibliography

[1] Chris Gerry and Peter Knight. *Introductory Quantum Optics*. Cambridge University Press, 2004.

[2] Mark Fox. *Quantum Optics: An Introduction*. Oxford University Press, 2006.

[3] Marlan O. Scully and M. Suhail Zubairy. *Quantum Optics*. Cambridge University Press, 1 edition, 1997.

[4] Rodney Loudon. *Quantum Theory of Light*. Oxford University Press, 3 edition, 2000.

[5] Hans A. Bachor and Timothy C. Ralph. *A Guide to Experiments in Quantum Optics*. Wiley, 9 2019.

[6] Thomas Young. I. the bakerian lecture. experiments and calculations relative to physical optics. *Philosophical Transactions of the Royal Society of London*, 94:1–16, 12 1804.

[7] David Griffiths. *Introduction to Quantum Mechanics*. Pearson Prentice Hall, second edition, 2005.

[8] R Hanbury Brown and R. Q. Twiss. Correlation between photons in two coherent beams of light. *Nature*, pages 27–29, 1956.

[9] George M K Baker, Chas C Foster, David Sarnoff, Frank M Folsom, Lewis Macconnach, and Ernest B Gorin. Radio and electronics research engineering radio corporation of america chairman of the board preside-lit.

[10] Hamamatsu Photonics K.K. Photomultiplier tube modules, 3 2019.

[11] D. Renker. Geiger-mode avalanche photodiodes, history, properties and problems. *Nuclear Instruments and Methods in Physics Research Section A: Accelerators, Spectrometers, Detectors and Associated Equipment*, 567:48–56, 11 2006.

[12] Excelitas technologies' spcm-aqrh-xx-tr single photon counting module datasheet. Available at `https://www.excelitas.com/product/spcm-aqrh-tr`.

[13] J. Chang, J. W. N. Los, J. O. Tenorio-Pearl, N. Noordzij, R. Gourgues, A. Guardiani, J. R. Zichi, S. F. Pereira, H. P. Urbach, V. Zwiller, S. N. Dorenbos, and I. Esmaeil Zadeh. Detecting telecom single photons with 99.5−2.07+0.5detection efficiency and high time resolution. *APL Photonics*, 6:036114, 3 2021.

[14] Sq nbtin superconducting nanowire single photon detector datasheet, 2022. Available at `https://singlequantum.com/wp-content/uploads/2022/08/Single-Quantum-Brochure-v2-digital.pdf-2.pdf`.

[15] Faraz Najafi, Francesco Marsili, Varun B. Verma, Qingyuan Zhao, Matthew D. Shaw, Karl K. Berggren, and Sae Woo Nam. Superconducting nanowire architectures for single photon detection, 2016.

[16] Chao Zhang, Yun□Feng Huang, Bi□Heng Liu, Chuan□Feng Li, and Guang□Can Guo. Spontaneous parametric down□conversion sources for multiphoton experiments. *Advanced Quantum Technologies*, 4:2000132, 5 2021.

[17] Bixuan Fan, Zhenglu Duan, Lu Zhou, Chunhua Yuan, Z. Y. Ou, and Weiping Zhang. Generation of a single-photon source via a four-wave mixing process in a cavity. *Physical Review A*, 80:063809, 12 2009.

[18] E H S Burhop, H B Gil, H J Kimble, and L Mandel. Photon antibunching in resonance fluorescence, 1977.

[19] Markus Hijlkema, Bernhard Weber, Holger P. Specht, Simon C. Webster, Axel Kuhn, and Gerhard Rempe. A single-photon server with just one atom. *Nature Physics*, 3:253–255, 4 2007.

[20] Igor Aharonovich and Elke Neu. Diamond nanophotonics. *Advanced Optical Materials*, 2:911–928, 10 2014.

[21] Mohammad Jamali, Ilja Gerhardt, Mohammad Rezai, Karsten Frenner, Helmut Fedder, and Jörg Wrachtrup. Microscopic diamond solid-immersion-lenses fabricated around single defect centers by focused ion beam milling. *Review of Scientific Instruments*, 85:123703, 12 2014.

[22] Erika Janitz, Mihir K. Bhaskar, and Lilian Childress. Cavity quantum electrodynamics with color centers in diamond. *Optica*, 7:1232, 10 2020.

[23] Ekber Selcuk. Guided and deterministic self organization of quantum dots, 2009.

[24] Esmaeil I.Z. Zadeh. Integrated quantum photonics from modular to monolithic integration, 2016.

[25] K. S. Novoselov, A. K. Geim, S. V. Morozov, D. Jiang, Y. Zhang, S. V. Dubonos, I. V. Grigorieva, and A. A. Firsov. Electric field effect in atomically thin carbon films. *Science*, 306:666–669, 10 2004.

[26] Kin Fai Mak and Jie Shan. Photonics and optoelectronics of 2d semiconductor transition metal dichalcogenides. *Nature Photonics*, 10:216–226, 4 2016.

[27] Yu Ming He, Genevieve Clark, John R. Schaibley, Yu He, Ming Cheng Chen, Yu Jia Wei, Xing Ding, Qiang Zhang, Wang Yao, Xiaodong Xu, Chao Yang Lu, and Jian Wei Pan. Single quantum emitters in monolayer semiconductors. *Nature Nanotechnology*, 10:497–502, 6 2015.

[28] Annemarie L. Exarhos, David A. Hopper, Raj N. Patel, Marcus W. Doherty, and Lee C. Bassett. Magnetic-field-dependent quantum emission in hexagonal boron nitride at room temperature. *Nature Communications*, 10:222, 12 2019.

[29] Carmen Palacios-Berraquero, Dhiren M. Kara, Alejandro R.-P. Montblanch, Matteo Barbone, Pawel Latawiec, Duhee Yoon, Anna K. Ott, Marko Loncar, Andrea C. Ferrari, and Mete Atatüre. Large-scale quantum-emitter arrays in atomically thin semiconductors. *Nature Communications*, 8:15093, 8 2017.

[30] Toan Trong Tran, Danqing Wang, Zai-Quan Xu, Ankun Yang, Milos Toth, Teri W. Odom, and Igor Aharonovich. Deterministic coupling of quantum emitters in 2d materials to plasmonic nanocavity arrays. *Nano Letters*, 17:2634–2639, 4 2017.

[31] Yongzhou Xue, Hui Wang, Qinghai Tan, Jun Zhang, Tongjun Yu, Kun Ding, Desheng Jiang, Xiuming Dou, Jun jie Shi, and Bao quan Sun. Anomalous pressure characteristics of defects in hexagonal boron nitride flakes. *ACS Nano*, 12:7127–7133, 7 2018.

[32] David Moss. Fabrication methods for integrating 2d materials. 1 2022.

[33] Chitraleema Chakraborty, Laura Kinnischtzke, Kenneth M. Goodfellow, Ryan Beams, and A. Nick Vamivakas. Voltage-controlled quantum light from an atomically thin semiconductor. *Nature Nanotechnology*, 10:507–511, 6 2015.

[34] M. Koperski, K. Nogajewski, A. Arora, V. Cherkez, P. Mallet, J.-Y. Veuillen, J. Marcus, P. Kossacki, and M. Potemski. Single photon emitters in exfoliated wse2 structures. *Nature Nanotechnology*, 10:503–506, 6 2015.

[35] Won Seok Yun, S. W. Han, Soon Cheol Hong, In Gee Kim, and J. D. Lee. Thickness and strain effects on electronic structures of transition metal dichalcogenides: 2h- <math display="inline"> <mrow> <mi>m</mi> <msub> <mi>x</mi> <mn>2</mn> </msub> </mrow> </math> semiconductors (<math display="inline"> <mi>m</mi> </math> <math display="inline"> <mo>=</mo> </math> mo, w; <math display="inline"> <mi>x</mi> </math> <math display="inline"> <mo>=</mo> </math> s, se, te). *Physical Review B*, 85:033305, 1 2012.

[36] Romain Bourrellier, Sophie Meuret, Anna Tararan, Odile Stéphan, Mathieu Kociak, Luiz H. G. Tizei, and Alberto Zobelli. Bright uv single photon emission at point defects in h -bn. *Nano Letters*, 16:4317–4321, 7 2016.

[37] Kenji Watanabe, Takashi Taniguchi, and Hisao Kanda. Direct-bandgap properties and evidence for ultraviolet lasing of hexagonal boron nitride single crystal. *Nature Materials*, 3:404–409, 6 2004.

[38] Mehran Kianinia, Blake Regan, Sherif Abdulkader Tawfik, Toan Trong Tran, Michael J. Ford, Igor Aharonovich, and Milos Toth. Robust solid-state quantum system operating at 800 k. *ACS Photonics*, 4:768–773, 4 2017.

[39] Toan Trong Tran, Christopher Elbadawi, Daniel Totonjian, Charlene J. Lobo, Gabriele Grosso, Hyowon Moon, Dirk R. Englund, Michael J. Ford, Igor Aharonovich, and Milos Toth. Robust multicolor single photon emission from point defects in hexagonal boron nitride. *ACS Nano*, 10:7331–7338, 8 2016.

[40] Elke Neu, Mario Agio, and Christoph Becher. Photophysics of single silicon vacancy centers in diamond: implications for single photon emission. *Optics Express*, 20:19956, 8 2012.

[41] Lukas Novotny and Bert Hecht. *Principles of Nano-Optics*. Cambridge University Press, 6 2006.

3

Experiment and Results

The aim of this experimental master project is to design and build an experimental setup for photoluminescence spectroscopy and second-order auto correlation ($g^{(2)}$) measurements of single-photon sources. In this chapter the reader is walked through the different steps that led to the realization of this goal.

Initially, the setup that would be based on a micro-photoluminescence (μPL) setup as used, for example, in [1] was required to be optimized for single-photon emission (SPE) from Indium Arsenide Phosphide (InAsP) quantum dots. InAsP QDs require cryogenic operation and have narrow SP emission lines in the near infrared (NIR). The design therefore includes a continuous flow cryostat in which a sample can be mounted on a two axes translation stage. Additionally, it contains a high resolution monochromator (Acton 750mm, $\sim$0.02nm) with the option of using one of three different groove density diffraction gratings. The monochromator can be used in two modes of operation depending on the position of its internal flippable mirror. When the flippable mirror is down, the filtered light is focused onto the sensor of a liquid nitrogen cooled CCD sensor for PL-spectroscopy measurements. With the flippable mirror engaged, the light that is filtered by the diffraction grating is directed towards an output port so that it can be further processed. The highest groove density diffraction grating can be used to extract the emission line of a single QD transition. The objective is NIR (from 480 to 1800 nm) infinity corrected with a relatively long working distance of 17.26 mm to bridge the gap that is inevitably induced by the cryostat between the sample and objective. Its numerical aperture is 0.42 and magnification 50X. It is mounted on a one axis translation stage.

Before the final version of the experimental setup is described in section 3.4, the reader is walked through process that led up to the final configuration. In section 3.1 we describe how the first goal of obtaining accurate PL-spectra was worked towards. Three iterations of the optical setup are briefly described and their advantages and disadvantages are discussed. The goal was reached with the third iteration, and, after its description, spectroscopy measurements are presented in section 3.2. In section 3.3 we describe how the second goal of obtaining $g^{(2)}$ measurements was worked towards. Sections 2.3-3.3.4 describe four different attempts to include a free-space Hanbury-Brown and Twiss (HBT) interferometer in the optical setup. The third attempt lead to the first $g^{(2)}$ measurements. The first $g^{(2)}$ measurement indicating indisputable anti-bunching with $g^{(2)}(0) < 0.3$ are obtained with the fourth and final version. Finally, we briefly discuss the response functions of our setup in an attempt to determine the reliability of our HBT-interferometer.

3.1. Working towards a μPL setup

3.1.1. First configuration

In the first configuration, a pump laser diode (LD) is coupled to the optical system via an optical fiber and collimating mirror (CM). Two carefully placed irises are used for alignment of the laser beam with the objective. Beamsplitter BS1 has a reflection-transmission ratio of 90:10 [1]. A large R:T ratio ensures that little of the collected signal is lost. An optimal beamsplitter transmits just sufficient excitation power and reflects plenty of the PL signal. All the other beamsplitters R:T ratios are 50:50. A white light source illumates the sample in the cryostat via flippable BS2. The illuminated light produces an image after being directed via OBJ, BS2, BS1, BS3 on to the sensor of an infrared camera. A 6 cm focal lens is screwed into a lens tube such that it focuses a plane at infinity onto an image on the sensor of the camera. The collected light from the sample is filtered (F) before being directed into the monochromator. A flippable mirror (FM) gives the option of coupling collected light into an optical fiber for future purposes.

+ Setup includes essential components (infrared camera, objective, cryostat, monochromator, laser diode, flippable 50:50 beamsplitter) that will also end up in the final, working version.
– Overall this setup is not successful as it is not able to produce PL-spectroscopy measurements. More specifically:
– Setup does not produce sample image.
– Beamsplitter BS2 displays unexpected behaviour with unwanted reflections and a R:T that seems to be different from the value suggested by its labeling.
– One mirror (CM) is not enough for alignment of the laser beam: if CM is not exactly lined up with I1, I2 and OBJ, alignment is impossible.
– One mirror is not sufficient for directing the collected light into the monochromator at normal incidence.

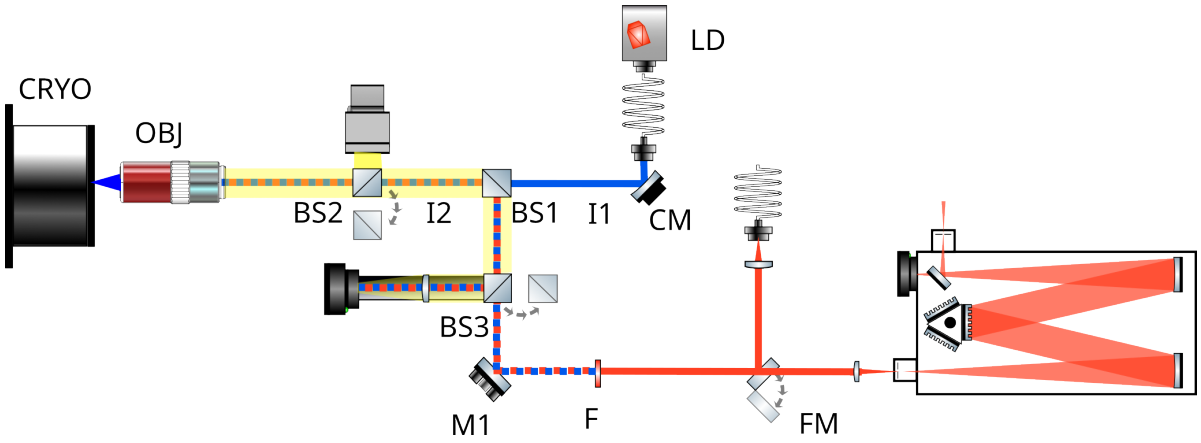

Figure 3.1: Schematic of the unsuccessful first version of the μPL setup.

[1] R:T value is suggested by labeling of BS1 and has not been verified at this point

3.1.2. Second configuration

A new, more compact arrangement combines the optical path connected to the infrared camera and the optical path connected to the illumination source into one via a 50:50 beamsplitter (BS3). Moreover, two lenses affecting the imaging (L1, L2) are installed on slidable lens mounts (see figure 3.3. Empirically, lenses of focal length $f = 17$cm and $f = 10$cm are found to give a workable sample image. Next to being collimated by lens L2, the illuminating light is passed through a 700 long-pass filter (F2) as without filtering, the light over saturates the camera.
The excitation laser is aligned with the objective. The laser beam is collimated by lens L5, instead of by a collimating mirror (CM in figure 3.1. Beamsplitter BS1 is replaced by a beamsplitter with R:T coefficients 70:30 [2] installed on an adjustable mount. Together with the adjustable beamsplitter, mirrors M6, M7 and M8 and irises I1, I2, I5 and I6 make alignment possible by a process of 'walking the beam', which, in the particular example of aligning with irises I1 and I2 is described as follows: mirror M7 (furthest away from I1) is adjusted untill the laser is aligned with I1. When aligned with I1, mirror M8 (mirror closest to I2) is used to align with I2. When aligned with I2, it is checked whether laser is still aligned with I1. If not, the process is repeated. If yes, laser is aligned with I1 and I2. As a rule of thumb: the further the distance between the two irises, the more accurate is the alignment.
The collected light is aligned with the input slit of the monochromator at normal incidence. Introduction of mirrors M2, M3, M4, M5 and irises I3 and I4 allow for proper alignment. If the sample reflects insufficient light for alignment, the cryostat can be removed such that light is directed through iris I6 and reflected off mirror M1.

This configuration additionally includes the possibility of side-excitation and side imaging with the introduction of flippable mirrors FM1, FM2, mirror M9 and lens L4. Side-excitation can be used to direct pump laser into, or collect emitted light from an on-chip waveguide. This new feature has not been used nor optimized as we have not come to measure on photonic integrated circuits (PIC).
A second new feature is the introduction of a helium-neon (HeNe) laser. A HeNe laser typically emits single-mode laser light at 632.8 nm of very high spectral purity (bandwidth of 0.002 nm). It is therefore well suited for calibration of the monochromator, but also for precise alignment as its beamspot is of a clear Gaussian shape. The HeNe laser is coupled to an optical fiber as follows: A laser diode of different color (green) is send out of fiber coupler FC. Simultaneously, the HeNe laser is roughly directed into FC. Both a HeNe and a green laser beam spot is made visible by inserting a half-transparent sheet of paper into the beam paths. Using the mirror closest to the HeNe source (Mbottom), and inserting the sheet between FC and the mirror closest to FC (Mtop) the HeNe beamspot is made to overlap with the green beamspot. When overlapping, the sheet is inserted in between HeNe and Mbottom. Now mirror Mtop is used to overlap the green beamspot with the HeNe beamspot. When overlapping, the sheet is again inserted between Mtop and FC to check whether the beamspots still overlap. If not, the process is repeated, if yes, HeNe is roughly coupled into FC. Afterwards, HeNe is more carefully aligned to FC by connecting the output of FC to a power meter and adjusting mirrors Mtop and Mbottom untill the signal is maximized. When aligned, the fiber is coupled into the optical system by connecting it to the fiber coupler located at LD in the schematic. See figure 3.2

- $+$ Introduction of extra mirrors and irises allow for more careful alignment.
- $+$ Slidable and interchangeable lenses (L1 and L2) allow for empirical determination of the combination of lenses that give a sample image as desired by the user.
- $+$ The introduction of HeNe allows for calibration of the monochromator and precise optical alignment.
- $-$ Although a desirably feature in the long term, the inclusion of the side-excitation/imaging optical path is unnecessary for the duration of the master end project.
- $-$ Accuracy of alignment could be improved upon by increasing distance between I3 and I4.
- $-$ Four aligning mirrors (M2, M3, M4, M5) is more than the required minimum of two. With each mirror reflection, although tiny, a fraction of valuable SPE is lost. Moreover, the reflectivity of the mirrors is optimal at a 45° angle. The beam reflects off of these mirrors at different than 45 $^\circ$ angles.
- $-$ A cube beamsplitter will inevitably produce unwanted reflections (ghost images). Moreover, the nature of the beamsplitter mount makes perfect alignment difficult (see figure 3.3).

[2] The value of R:T has not been verified, but is assumed from its labeling

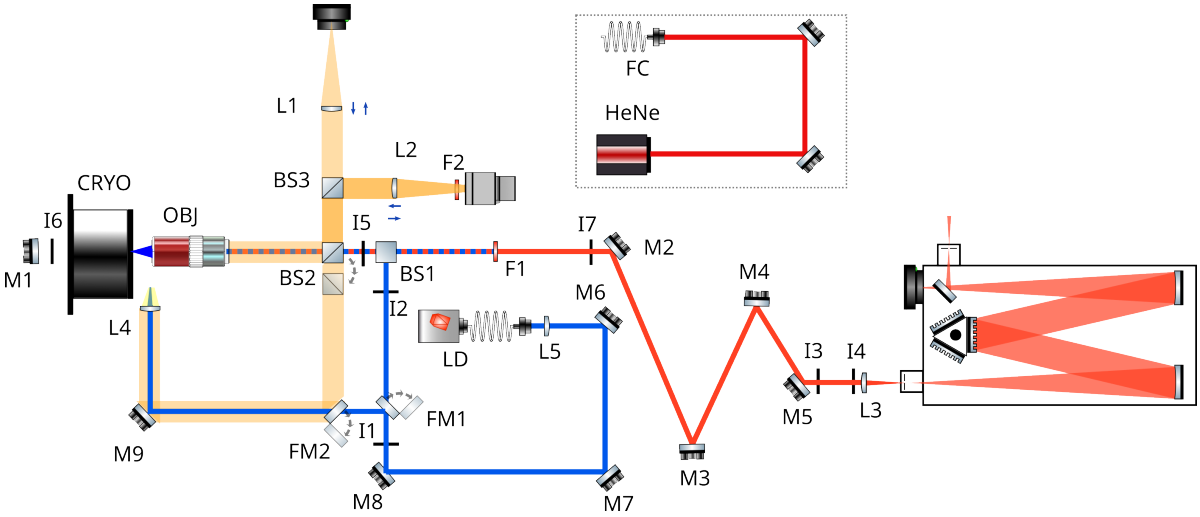

Figure 3.2: Schematic of the second version of the optical setup.

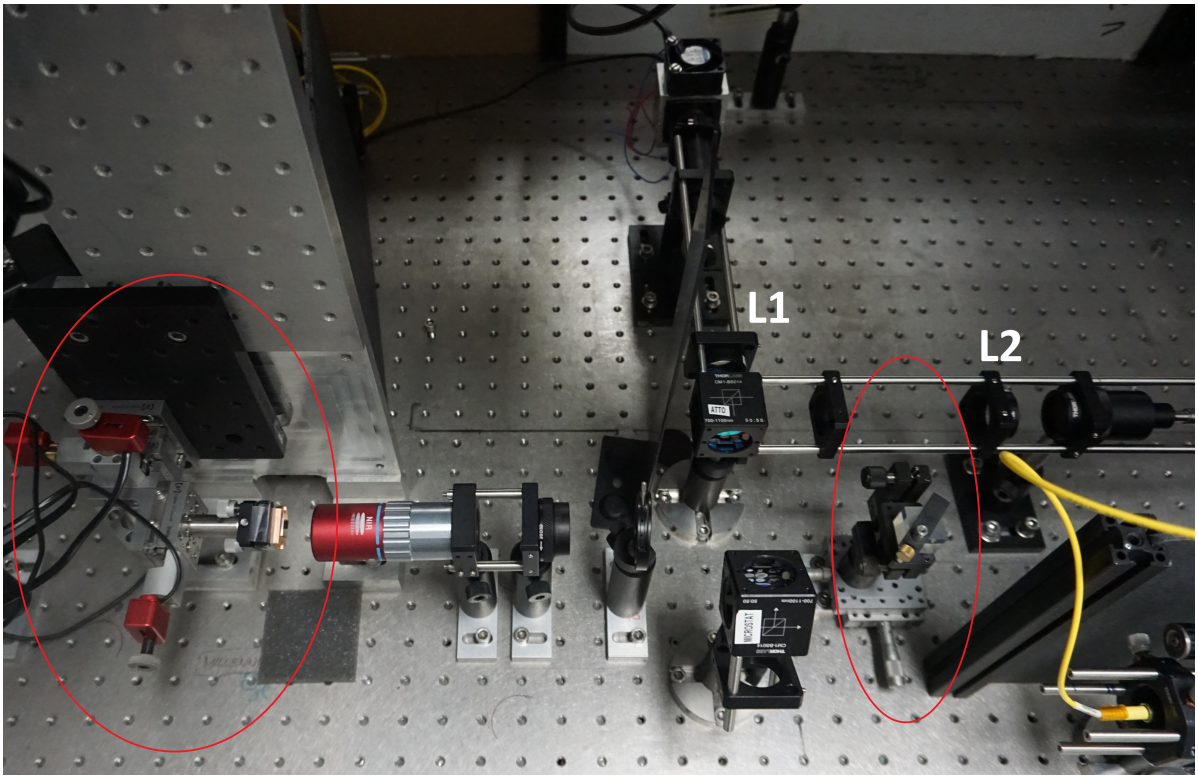

Figure 3.3: Photograph of part of the second version of the optical setup. In the top right, the new arrangement of the imaging system is visible which includes slidable lens mounts (L1, L2). Encircled in red on the left is a three axis translation stage temporarily replacing the cryostat. The translation stages in the cryostat were malfunctioning and were sent off to the manufacturer for rapair. On the right, the cube beamsplitter (BS1) is encircled. The nature of the beamsplitter mount made it difficult to position the beamsplitter exactly on the crossing of the two optical beam paths (pump laser and collection).

3.1.3. Third configuration

The third configuration improves upon the second in a number of ways.
The cube beamsplitter (BS1) has been replaced by a pellicle beam splitter with R:T 33:67. Ghost images are reduced and the beamsplitter is able to be installed on a mount that allows for easier alignment. The new beamsplitter mount however requires the pump laser to be directed onto the beamsplitter from above, instead of from below (in the schematic). The imaging and excitation sections are therefore positionally interchanged. Moreover, the number of mirrors in the system has been reduced. The three mirrors previously used for directing the pump laser into the optical system has been reduced to two (M1, M2). The four mirrors that previously directed the collected light into the monochromator have been reduced to two (M4, M5). Apart from the latter being beneficial in terms of losses, it additionally leads to a larger separation between mirror M5 and the input of the monochromator, allowing for more accurate alignment. Also, the over complete feature of side-excitation/imaging has been removed. At this point in time it does not seem likely that measurements of PICs will be performed during this master project. Finally, the option of fiber coupling the output signal of the monochromator is introduced and a fourier optics analysis has been performed to determine the slit width and lens focal length (L3, L4) that optimizes the coupling of the signal to the monochromator. See the appendix A.2 for calculations.

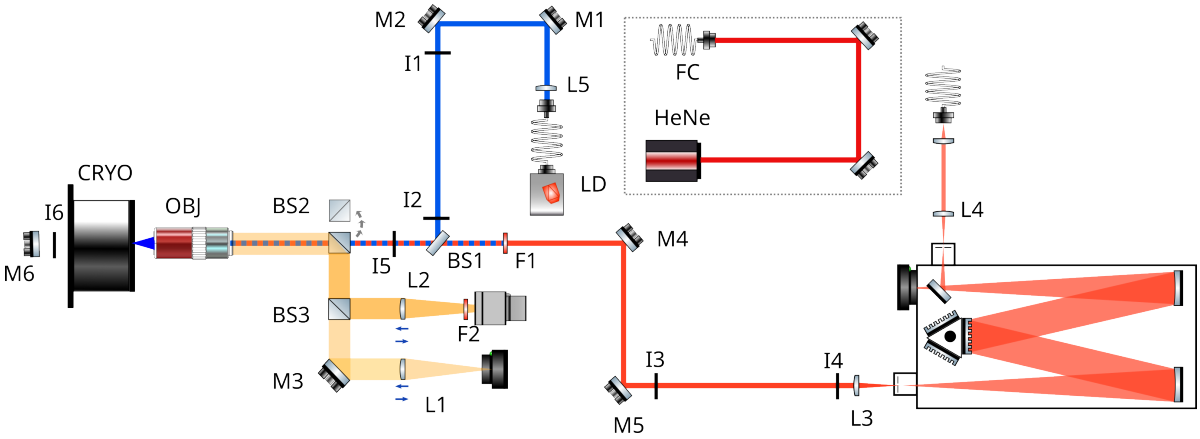

Figure 3.4: Schematic of the third configuration of the optical setup that is used for PL-spectroscopy measurements presented in section 3.2.

A problem was encountered with the images produced by the CCD camera of the spectrometer. Independent of the intensity of the incoming light, entire columns of pixels appear to be illuminated leading to spectra of too high intensities. The problem is understood as follows: A CCD sensor consist of a matrix pixels each of which is a metal-on-oxide semiconductor (MOS) capacitor. The pixels are overlayed with a light-sensitive thin film. Each capacitor functions as a bin that can collect photoelectrons generated by light incident on the thin film. During exposure, charge builts up on each pixel's capacitor. The pixels in each column are connected by switches. On the bottom the matrix is connected to an output which directs the charges to circuitry that converts the analog to digital values. During readout the pixels are emptied into the output channel one row at the time, starting at the bottom row of pixels. If exposure is continuous, a pixel on which light is incident will not be emptied during readout, but will instead continuously feed charge into underlying pixels, which, by the nature of the system's readout mechanism, will be interpreted to be stemming from pixels lying above the illuminated pixel. This will lead to an inaccurate image. Installation of a shutter in front of the input of the spectrometer to allow for readout time during which the sensor is not exposed resolves the issue. Comparison of a CCD image that is continuously exposed with a CCD image that is obtained using a shutter is shown in figure A.4.

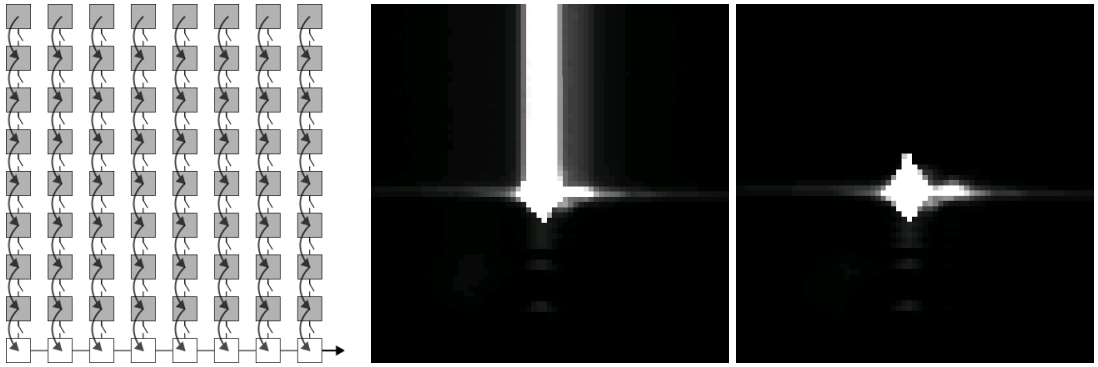

Figure 3.5: Three images illustrating the issue encounted with the spectrometer CCD image. Left displays the readout mechanism of the CCD sensor. Note that the sensor is readout one row at a time, by transferring collected charge via underlying pixels to the output channel on the bottom. The middle and left images compare a CCD image obtained with (right) and without (middle) the use of a shutter. Without a shutter, pixels are continuously exposed, also during readout. The CCD system will misinterpret the output signal resulting in an innacurate image.

3.2. Spectroscopy measurements

With the third configuration of the μPL setup, PL-spectroscopy measurements can be performed. In this section a selection of PL-spectra of different materials is presented. In section 3.2.1 PL-spectra of three different samples of thin film silicon nitride on silicon dioxide substrate are displayed, each fabricated under different conditions. The SiN samples were investigated in search for localized emission, as it has been reported that SiN fabricated under the appropriate conditions hold SPEs. Localized emission was not observed. In section 3.2.2 PL-spectra of monolayer and few-layer tungsten diselenide (WSe_2) are presented. Two-dimensional WSe_2 has been reported to hold point defects emitting single-photons at cryogenic temperatures. The cryostat however was unavailable during the time we had access to the WSe_2 sample as its translation stages were malfunctioning and it was sent over to its manufacturer for repair. Not more than a couple of days was spent on measuring WSe_2, as an accident damaged the sample to such an extent that measurements were no longer possible. Nevertheless, a selection of the recorded PL-spectra are presented. Finally, in section 3.2.3 we present PL-spectra of hexagonal Boron Nitride (hBN) nanoflakes. hBN has been reported to be capable of bright SPE at room temperature. We find highly localized bright emission which pressed for the extension of the setup with an HBT-interferometer so that it could be investigated whether the emission was single-photon in nature or not.

3.2.1. Silicon Nitride

Inspired by Senichev et. al., whom in their publication [2] report on SPEs in Silicon Nitride (SiN), three SiN samples, each annealed under different conditions, are manually scanned in search of localized emission lines suggestive of a single-photon source. The SiN films are grown on a sillicon dioxide substrate by High Density Plasma Chemical Vapor Deposition at a ratio SiH_4:N_2 of 1:1, 1:4, 1:6 for sample 1, 2 and 3 respectively. Manually scanning the samples is highly laborious, and spectra are recorded at at most three different positions on each sample. The single-photon emitting SiN in [2] is fabricated at a SiH_4:N_2 ratio of 1:6. The spectra of sample 1, which indeed did not reveal any obvious localized emission are therefore not presented. The spectra of sample 2 and sample 3 are shown in figures 3.6 3.7. In the figures, no significant difference between spectra of the same sample at different positions stand out. Neither were localized emission lines observed during visual inspection of the spectra whilst scanning over the samples. To rule out the presence of SPEs however, an automated scanning (confocal) microscope set up is necessary. Such setup would allow for a more thorough investigation of the SiN samples. Three different excitation laser wavelengths are used: 453 nm (blue), 512 nm (green) and 632 nm (red). For blue and green three different levels of intensity are used. Red is only used at one intensity level. All spectra are obtained using a 150 g/mm blazed diffraction grating.

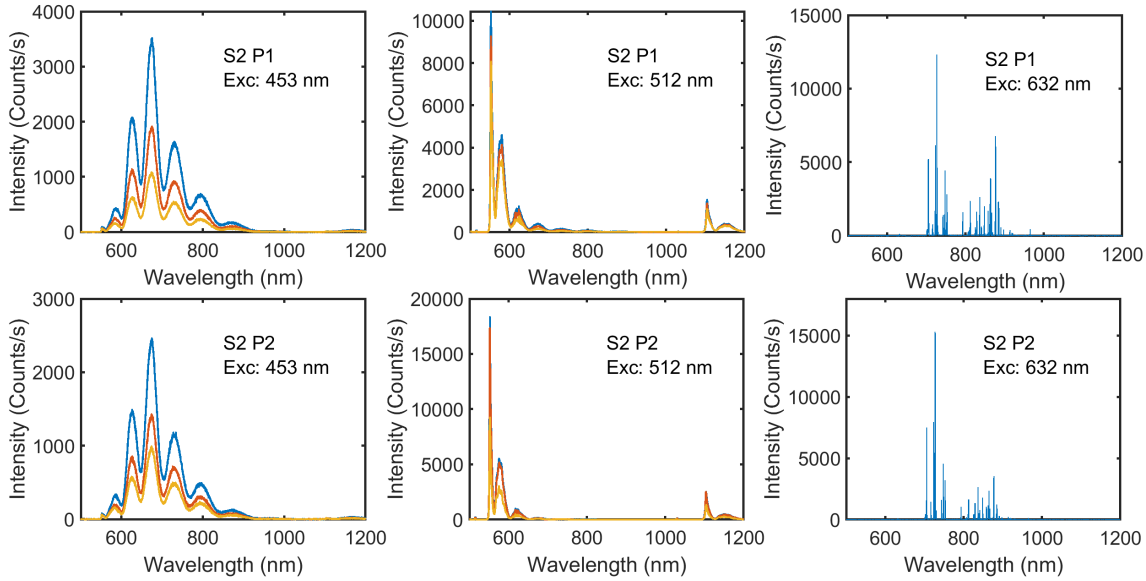

Figure 3.6: Sample (S) 2, Position (P) 1 (upper row) and position (P) 2 (lower row). PL spectroscopy measurements of SiN grown at a ratio of SiH_4/N_2 of 1:4 under excitation of (from left to right) 453 nm, 512 nm and 632 nm. For 453 and 512 nm three different excitation intensities are applied. Blue curves indicate highest intensity, yellow curve lowest intensity.

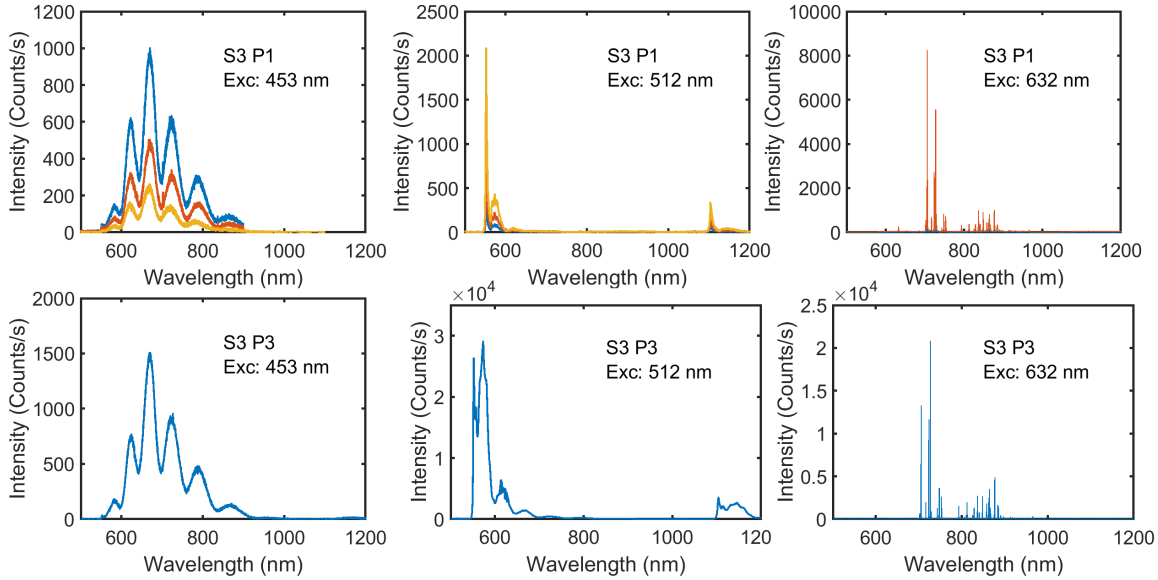

Figure 3.7: Sample (S) 3, Position (P) 1 (upper row) and position (P) 3 (lower row). PL spectroscopy measurements of SiN grown at a ratio of SiH_4/N_2 of 1:6 under excitation of (from left to right) 453 nm, 512 nm and 632 nm. For 453 and 512 nm three different excitation intensities are applied. Blue curves indicate highest intensity, yellow curve lowest intensity. Measurements of position 2 yielded similar spectra and are therefore not presented.

3.2.2. Tungsten Diselenide

Two-dimensional tungsten diselenide (WSe_2) has been reported to be capable of bright SPE at cryogenic temperatures. Despite a number efforts to resolve the issues, the cryostat has not been operational within the duration of this project. It is therefore ruled out that SPE is obtained from WSe_2. Not more than a couple of days was spent on measuring WSe_2, as additionally, an accident damaged the sample to such an extent that measurements were no longer possible (see figure 3.9). Nevertheless, a selection of the recorded PL-spectra are presented in figure 3.8. WSe_2 was one of the first samples that was taken PL-spectroscopy measurements from. I was getting used to the monochromator and had not established proper data recording methods. The origin of the spectrum displayed in the right figure is therefore not properly documented. Interpretation of the spectra is left for future studies.

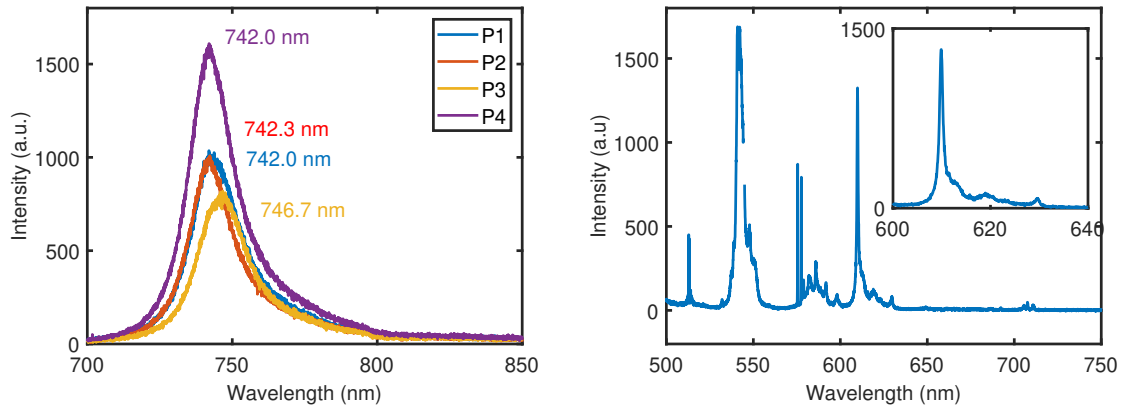

Figure 3.8: Left: PL-spectra of different positions on mono- or few-layer WSe_2. Direct bandgap transitions in two dimensional WSe_2 are known to correspond with emission peaks around 760nm [3]. Right: PL-spectrum of WSe_2 of which exact origins are uncertain. Spectral shape resembles that of a room temperature Raman spectrum of monolayer WSe_2 reported in [3] (figure 5a).

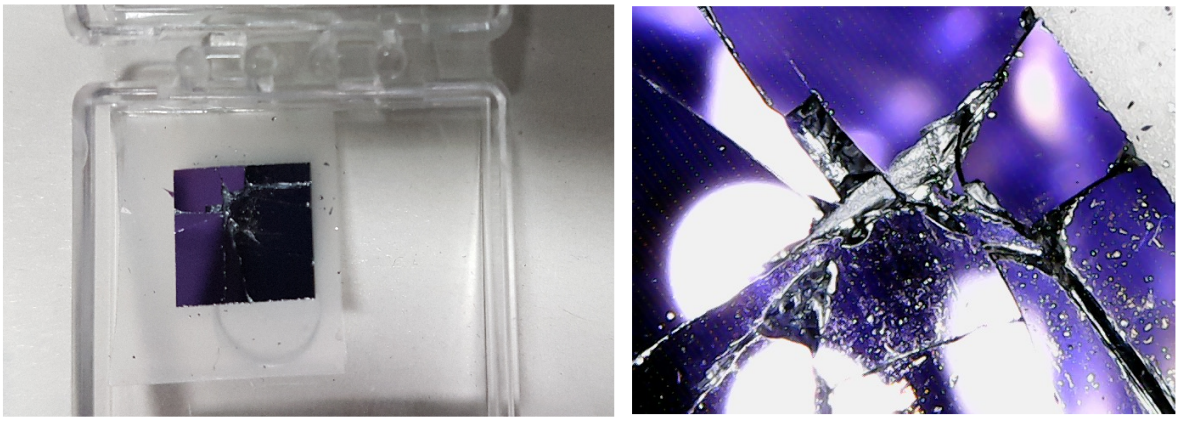

Figure 3.9: Photograph (left) and optical microscope (right) image of the damaged WSe_2 sample.

3.2.3. Hexagonal Boron Nitride

Hexagonal Boron Nitride (hBN) is known to hold SPEs at room temperatures. hBN sample is obtained from a collaboration with the University of Exeter. Two spectra are presented here displaying sharp peaks centered around different wavelength (figure 3.10). The most interesting emission line is the one centered around 810 nm. It displays best signal to noise ratio, is due to its large wavelength easily separated from the higher energy 453 nm pump laser signal, and matched a 810-10 bandpass spectral filter available in the lab. Line profiles are taken of the emitter corresponding to the 810 nm ZPL (figure 3.11), demonstrating the localized nature of the source of the emission.

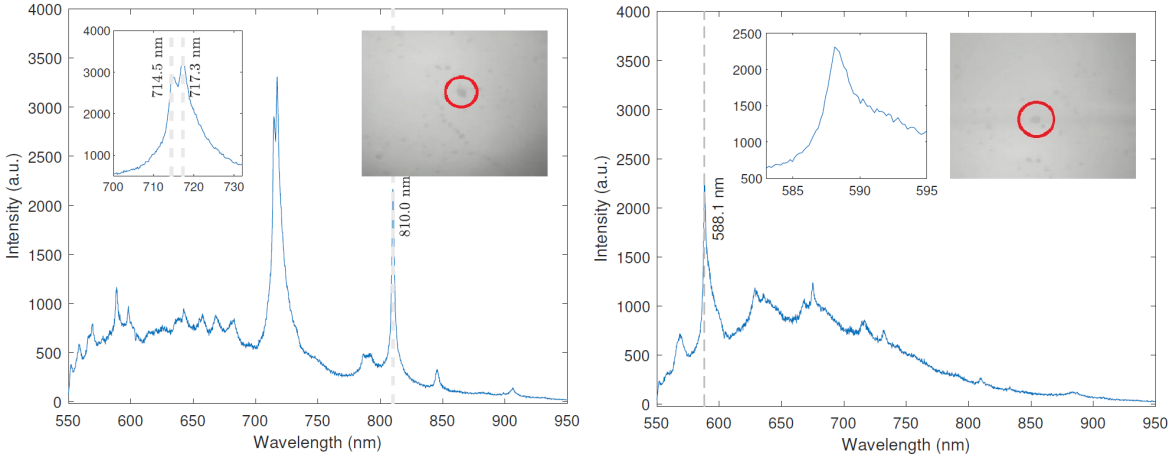

Figure 3.10: Photoluminescence spectra of two different hBN nanoflakes obtained using a 453 nm pump laser. Left: Two clear distinct peaks stand out. The left peak is enlarged in the left inset, emphasizing the fact there are two peaks separated by about 3 nm. The right peak is positioned at 810 nm. Right inset displays position of the emitter encircled in red. Right: Emission line at 588.1 nm stands out. Right inset displays position of the emitter. Left inset presents the emission line enlarged.

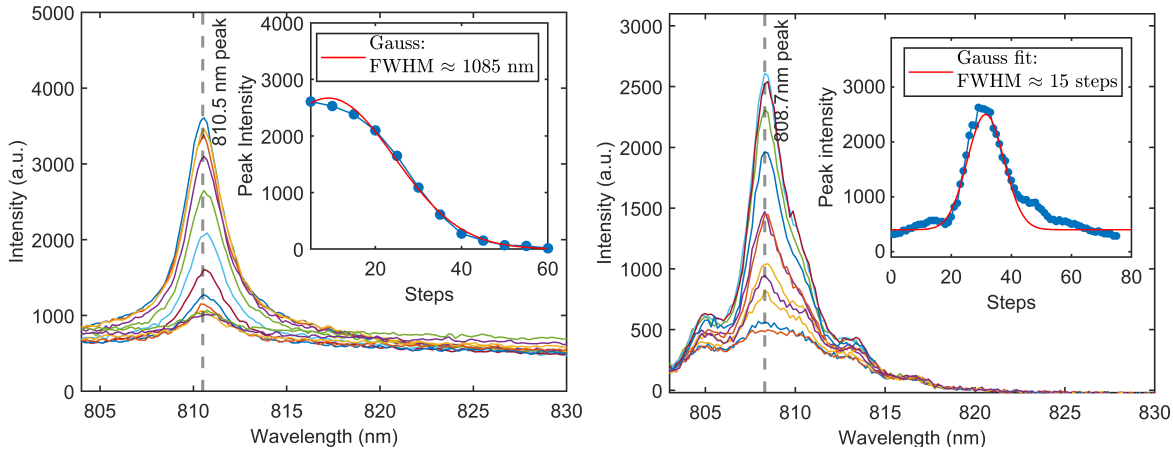

Figure 3.11: Two line profiles of the emitter corresponding to the emission line centered around 810 nm visible in figure 3.10 obtained using a pump laser of 453 nm (left) and 520 nm (right). For each of the line profiles, the sample was mounted on a different translation stage. The step size of the stages corresponding to the figure on the left is 30 nm. The step size of the stages used in obtaining the figure on the right is unknown. Both figures demonstrate the localized nature of the emitter. Left: Spectral lines measured for a range of excitation positions. Inset shows a line profile. Step size is 30 nm. From a Gaussian fit a FWHM ≈ 1085 nm is extracted, presumably much larger than the size of the emitting point defect which, being of a size comparable to a single atom, is assumed to be of the order of a few tens of nanometers. The width of the line profile is therefore probably largely determined by the excitation laser beam spot and NA of the objective. Excitation laser of 453 nm is used. Right: Spectral lines for a range of excitation positions. Inset shows line profile. Excitation laser of 520 nm is used. Signal is spectrally filtered by a 550 longpass and 810-10 bandpass filter. The latter is responsible for the wavy side-bands and improves the signal-to-background emission ratio. A slight blueshift is observed compared to (left).

3.3. Second-order autocorrelation measurements

Having confirmed the localized nature of the source of the emission line centered around 810 nm, second-order autocorrelation measurements are required to determine whether or not the emission is single-photon in nature. Sections 2.3-3.3.4 describe four different attempts to include a free-space Hanbury-Brown and Twiss (HBT) interferometer in the optical setup. The third attempt lead to the first $g^{(2)}$ measurements. The first $g^{(2)}$ measurement indicating indisputable anti-bunching with $g^{(2)}(0) < 0.3$ are obtained with the fourth and final version.

3.3.1. First HBT-interferometer configuration

The first attempt is schematically displayed in figure 3.12. It was inspired by the confocal scanning microscope built by Yanik Herrmann (Qutech), in which the detectors where positioned in a compact lightproof cardboard box. The advantages of this setup are that the monochromator is bypassed. The output signal of the monochromator is at best 60 % of the input signal. Bypassing the monochromator therefore leaves more signal to work with. Additionally, the setup is compact. This allows for good enclosure of the APDs with a opague, cardboard box. Disadvantages however are that alignment is difficult. In principle, there are two adjustable mirrors per APD for alignment. M1 and M2 can be used for coupling to the bottom APD, and M3 and M4 can be used to couple to the other APD. In practice, the fact that M1 also affects the beam passing M3 and M4 makes alignment difficult. Moreover, mirrors are too course to properly couple light to the tiny 180 μm active areas of the APDs. Also, alignment can only be done when the enclosing cardboard box is removed. This in turn requires the roomlight to be minimized, as the sensitive APDs can not be exposed by too much light. Finally, the fact that the monochromator is bypassed is an advantage in terms of photon counts, but a disadvantage as the monochromator can be used for very narrow bandwidth filtering, which is useful for processing the narrow emission lines of quantum dots for instance.

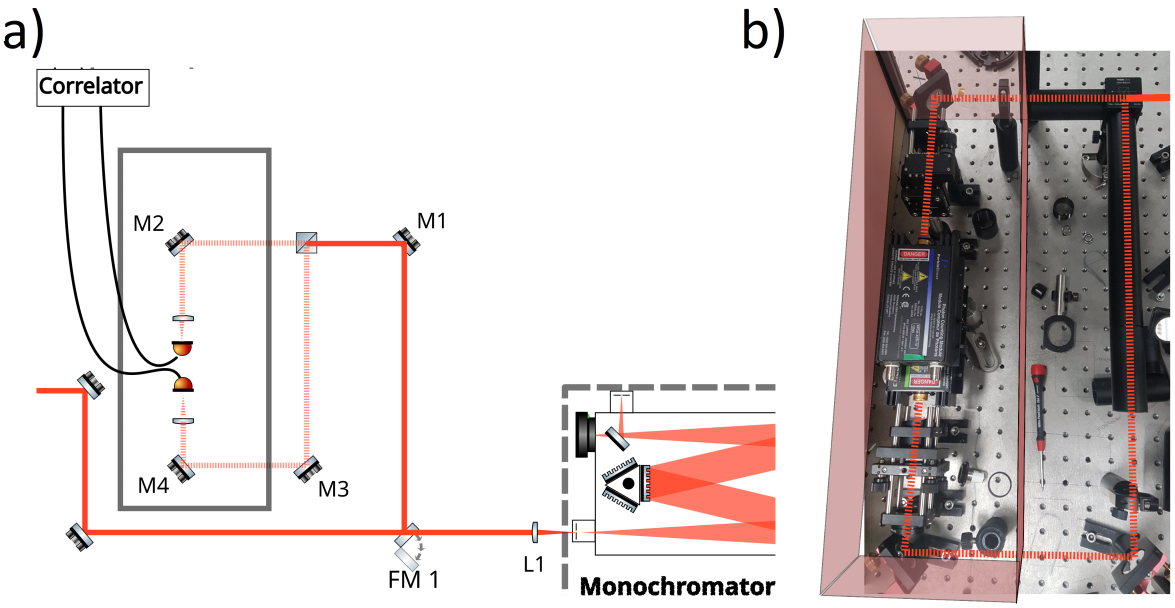

Figure 3.12: a) Schematic of the first configuration of the optical setup including an HBT-interferometer. A flippable mirror (FM1) directs the light into the HBT-interferometer. Two adjustable mirrors (M1, M2) can be used for coupling to the bottom detector, and two other (M3,M4) for coupling to the second detector. b) Photograph of the HBT-interferometer. A drawing indicates where the lightproof container would be. Light is sent into the container through tubes and irises embedded into the cardboard box, minimizing the box openings.

3.3.2. Second HBT-interferometer configuration

The second design of the HBT setup (figure 3.13) improves upon the first by allowing for both bypassing of the monochromator, and for using the monochromator depending on the positions of flippable mirrors FM1 and FM2. Moreover, instead of sending the signal into the HBT interferometer, it can be coupled to an optical fiber so that it can e.g. be processed with in-fiber components or directed to SNSPDs elsewhere in the lab. Also, more accurate coupling to the detectors is now possible using lenses L1 and L2 that are installed on fine resolution x-y-z translation stages. The HBT interferometer is encapsulated by an opague cardboard box. The light enters the box through an iris. Advantages: the option of either using the monochromator's filtering capacities, or bypassing the monochromator. Signal can be fiber coupled for further processing. Compared to the previous configuration, x-y-z stages of lenses L1 L2 allow for slightly easier alignment. Disadvantages: similarly to the last version of the HBT setup, the opague box needs to be removed for alignment, requiring roomlight to be minimized. Although using the movable lenses for alignment instead of adjustable mirrors is a slight improvement, it is still not optimal. For best performance (small focussing beam spot, least amount off loss), light should be directed through the center of the lens. Ideally, the APDs are mounted on translation stages instead.

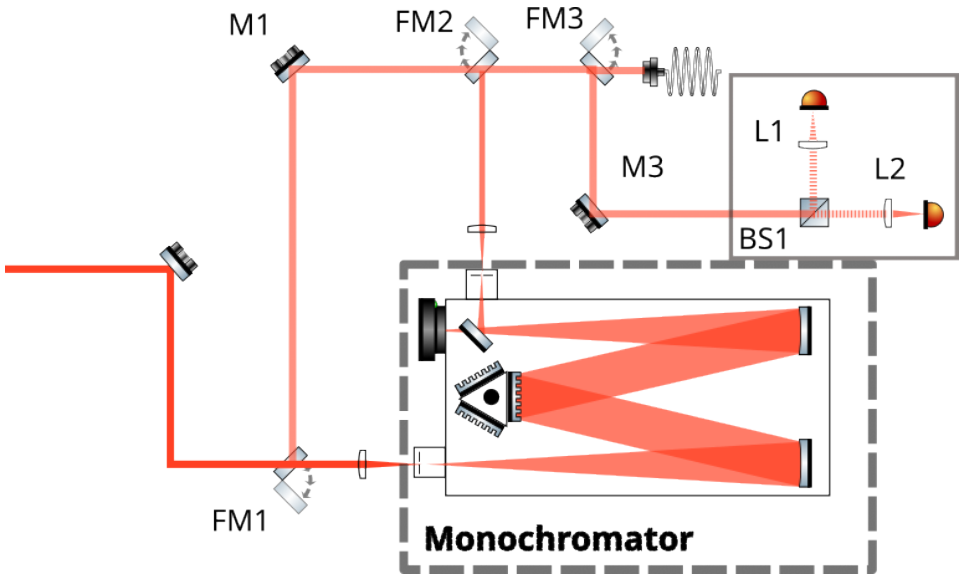

Figure 3.13: Schematic of the second attempt of inlcuding an HBT-interferometer in the optical setup. A flippable mirror (FM1) gives the option of bypassing the monochromator. Another flippable mirror (FM3) sends the collected light into the free-space HBT-interferometer for $g^{(2)}$ measurements when engaged. When not, the collected light is directed into an optical fiber.

3.3.3. Third HBT-interferometer configuration

In the third design, the HBT-interferometer is installed on a breadboard. Instead of a cardboard box, an opague cloth is used to darken the HBT-setup and suppress background light. Lenses on translation stages are still used for alignment, as we have not found a way of mounting the APDs on translation stages yet. The advantages of this design are that the detectors can remain covered during alignment by carefully maneuvering your hands under the cover. Moreover, with the HBT interferometer being installed on a breadboard it can be easily moved to for instance the output port of the monochromator. The first auto-correlation measurements are performed in the composition as depicted in figure 3.14.

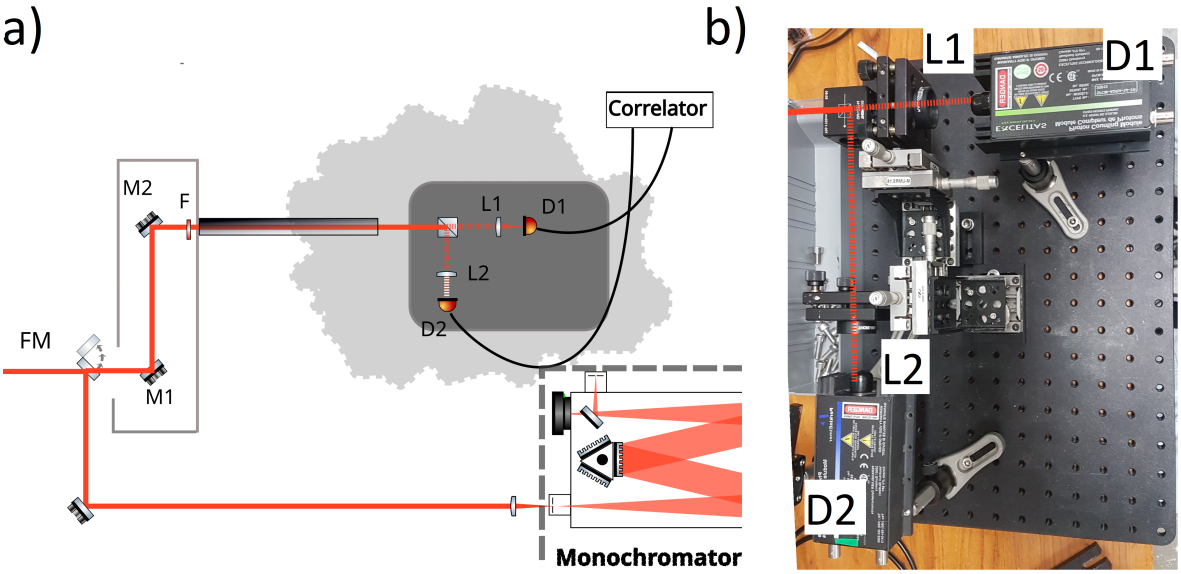

Figure 3.14: a) Schematic of the third attempt of including the HBT interferometer into the optical setup. Mirror M1 and M2 are enclosed by a cardboard box to suppress noise. From mirror M2 light is directed via an optical filter through an iris into a tube. The tube directs the light under the opague cover into the HBT-interferometer. When initiated, flippable mirror FM1 sends the light into the monochromator for spectroscopy. b) The HBT-interferometer is installed onto an optical breadboard. The lenses L1 and L2 are mounted on x-y-z translation stages.

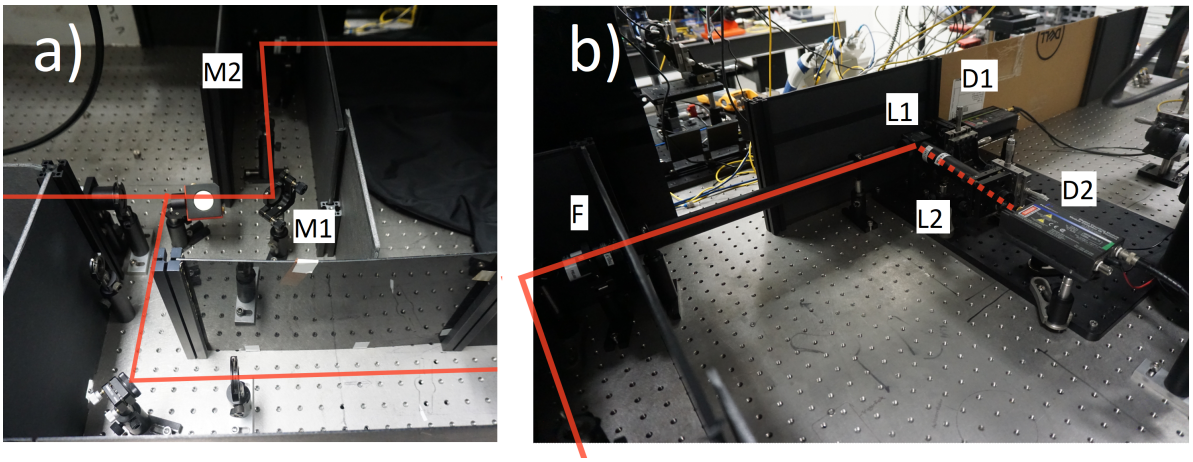

Figure 3.15: Photographs of the third HBT-interferometer configuration. A flippable mirror (a) directs the collected light towards the monochromator when engaged. When not engaged, light is directed towards the HBT-interferometer via mirrors M1,M2 (a) and filter F (b). During measurement, a lid encloses the 'box' encapsulating M1, M2 and F, and the HBT-interferometer visible in (b) is carefully covered by an opaque cloth.

Cross-talk between detectors

In the first $g^{(2)}(\tau)$ measurements a problem is encountered: two atypical sharp peaks appear approximately 10 ns apart. The hypothesis is that the peaks are caused by crosstalking between the two SAPDs

via photons emitted by a detection event. The phenomenon is briefly mentioned in the datasheet of the manufacturer and the characteristics of this particular photoemission, or 'breakdown flash' is investigated in [4]. As the spectrum of the breakdown flash overlaps with the spectrum of the 810-emitter, reduction of the crosstalk by means of spectral filtering will also reduce the light of interest. Therefore, an attempt is made to apply spatial filtering of the breakdown flash by slightly rotating the beamsplitter and installing irises at each of its output ports (figure 3.16).

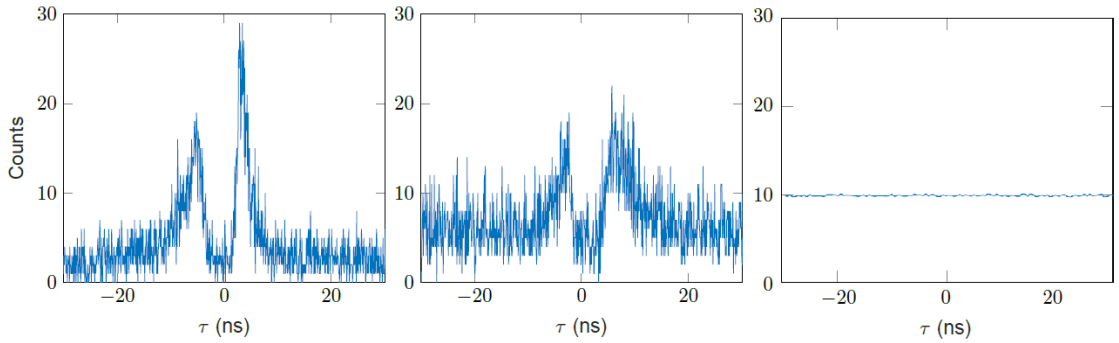

Figure 3.16: Left shows the affect of breakdown flash cross-talking between APDs on $g^{(2)}(\tau)$ measurements. Middle is a first attempt at suppressing this unwanted phenomenon by slightly tilting the beamsplitter. Namely: only the reflected, and not the transmitted light is affected by the orientation of the beamsplitter. A slight rotation of the beansplitter therefore spatially filters out some of the cross-talk (see figure 3.17 (b)). The cross-talking was completely overcome (right) after rotating the beamsplitter even more and additionally installing irises right infront of the lenses focussing the light on the APDs (see figure 3.18 (b)). Note: the data in the right figure is collected in larger bins (512 ps per bin versus 64 ps per bin) and therefore appears less noisy than the other two.

First hint of photon anti-bunching

With the configuration of figure 3.14 a first $g^{(2)}(\tau)$ is measured of the emission line centered around 810 nm that hints towards photon anti-bunching (figure 3.17). At this point a first attempt has been made to suppress the cross-talk betwen detectors and the beamsplitter is only slightly tilted (middle figure 3.16). The complete suppression of the crosstalk (as displayed in the right plot of figure 3.16) was accomplished later. The measurement therefore is still affected by the cross-talking between the ADPs. Moreover, the photon count rate incident on the detectors is low ($\approx 4.7 \times 10^3\,\mathrm{s}^{-1}$ with pump laser on and $\approx 1.5 \times 10^3\,\mathrm{s}^{-1}$ with laser off (dark counts). Integration time was only a couple of hours and a large resolution is applied: each time bin is 512 ps wide. The signal to dark counts ratio is with $\approx 3:1$ sub optimal and is improved upon in the next correlation measurements.

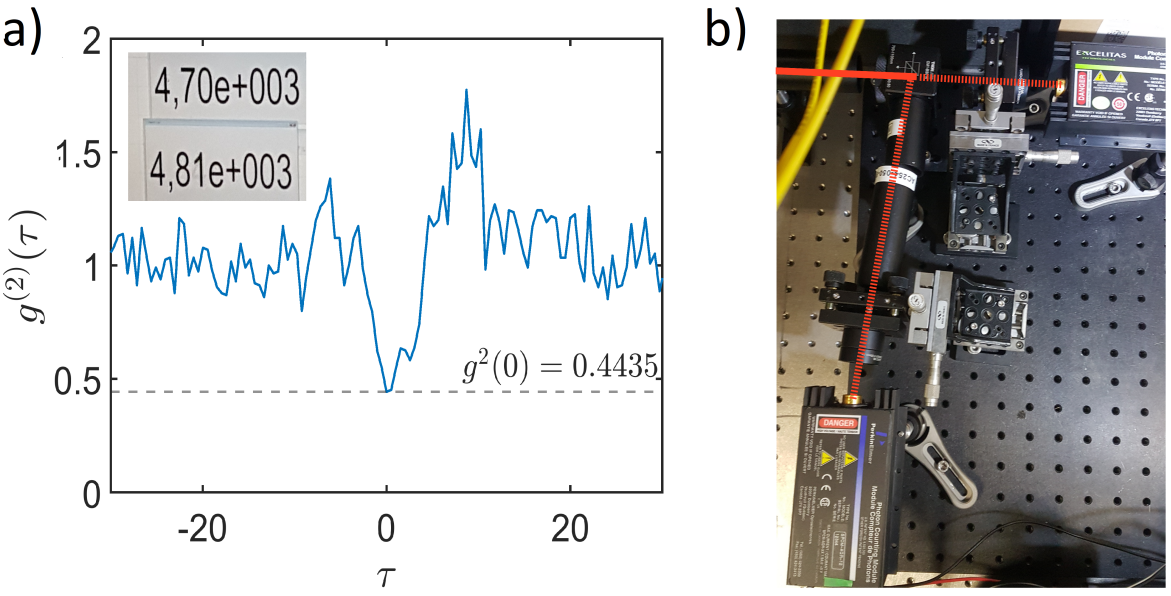

Figure 3.17: a) First hint of photon anti-bunching. Measurement is of too low resolution (bin size 512 ps), and consists of too little data points (total count of 7.15×10^7) to establish SPE. Inset displays a snapshot of the count rates of the two detectors. Dark count rates were approximately a factor of 3 lower $\approx 1.5 \times 10^3\,\mathrm{s}^{-1}$. Measurement is despite suppression, still affected by cross-talk between detectors. b) a slight tilt of the beamsplitter decreases the crosstalk between detectors. This configuration corresponds to the $g^{(2)}(\tau)$ in (a) and also to the middle correlation measurement in figure 3.16.

3.3.4. Fourth HBT-interferometer configuration

In the final configuration (figure 3.18), the breadboard mounted HBT-interferometer is aligned with the output port of the monochromator. The signal is filtered before entering the monochromator (F) and additional spectral filtering by the diffraction grating of the monochromator is optional. The signal is either directed onto the sensor of the monochromator's CCD camera or sent towards the HBT-interferometer, depending on the position of the flippable mirror (FM). In the second case, the light is sent through a tube that directs the light under the opague cover into the HBT-interferometer. A lens (L4) inside the tube collimates the light. Not the lenses (L1 and L2), but the APDs are now mounted on x-y-z translation stages. The beamsplitter is more heavily tilted and irises are installed which successfully suppresses cross-talk between the detectors (see right figure in 3.16).

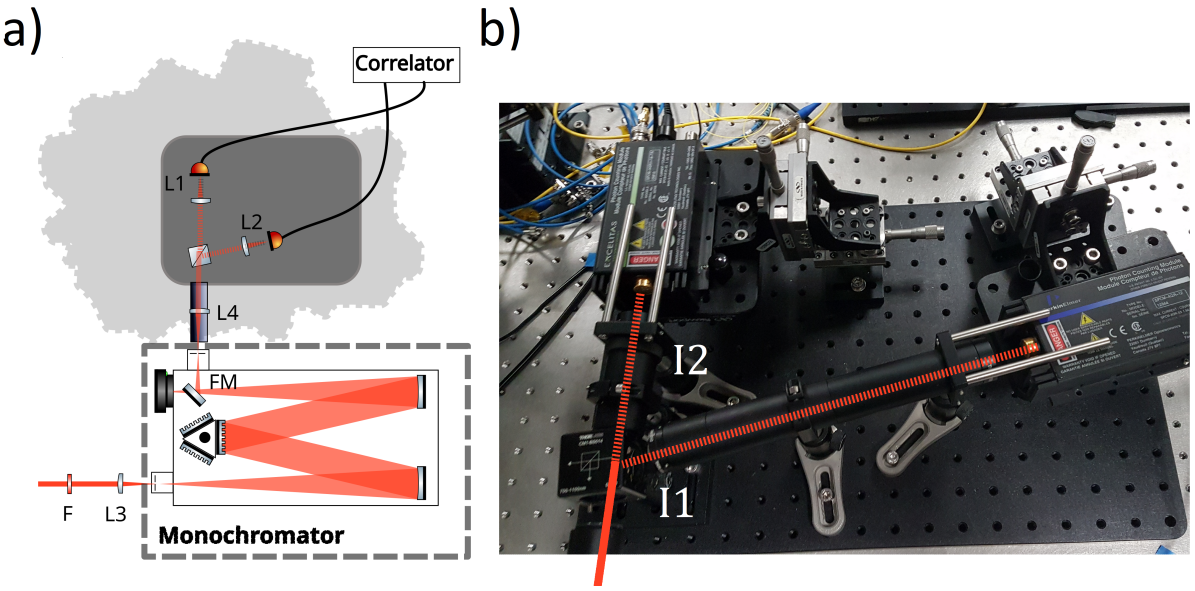

Figure 3.18: a) Schematic of the final configuration of the HBT-interferometer. Spectral filtering is performed by filter F and optionally by the diffraction grating of the monochromator. Flippable mirror FM directs light towards HBT-interferometer when initiated. Otherwise light is incident on the CCD camera, allowing for spectroscopy measurements. An opague cloth (light grey) is used to suppress dark counts. b) Photograph of the HBT-interferometer. Cross-talk between detectors has been completely suppressed by spatial filtering using two irises (I1, I2) and orientating the beamsplitter slightly rotated with respect to the incoming light beam. The APDs are mounted on x-y-z translation stages.

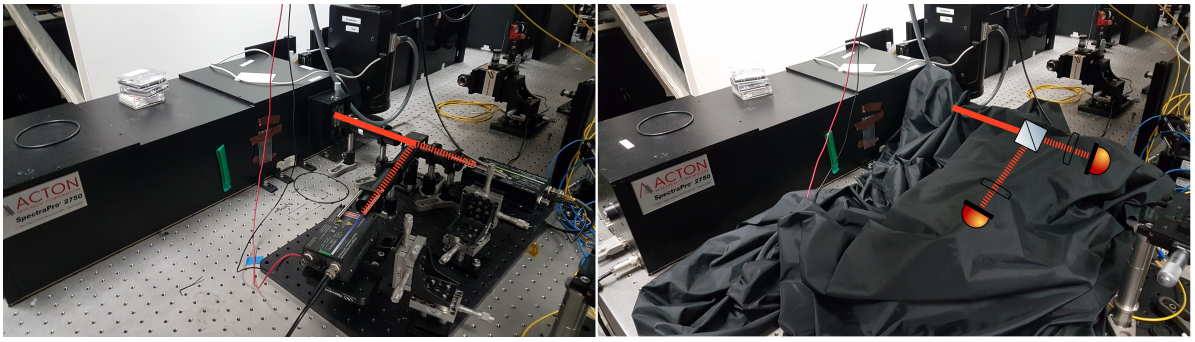

Figure 3.19: Two photographs displaying the HBT-interferometer uncovered (left) and covered (right).

Second-order autocorrelation measurement indicating pronounced photon anti-bunching

The detectors are intially aligned using a strongly attenuated laser. More fine adjustments are made with the 810 nm emission line. Green instead of blue pump laser (453 nm vs 520 nm) is used as it gives a higher intensity 810 nm emission line and better signal-to-background emission ratio (see figure 3.11). The collected light is spectrally filtered by a 550 nm longpass filter and a 810-10 bandpass filter. After alignment, the count rates of the detectors fluctuate around the following values: $SI8.9E3$ and $9.0 \times 10^3\,\mathrm{s}^{-1}$ during excitation, and $4.6 \times 10^2\,\mathrm{s}^{-1}$ and $9.8 \times 10^2\,\mathrm{s}^{-1}$ with excitation laser switched off (dark counts). The signal to dark count ratio of over 10:1 is an improvement of well over a factor 3 compared to the first attempt. The measurement is performed overnight, spanning approximately 12 hours. The obtained $g^{(2)}(\tau)$ curve displays strong anti-bunching with a $g^{(2)}(0) < 0.3$. The data within interval $\tau = [-20, 20]$ is fitted using a typical three-level model expression $g^{(2)}(\tau) = c - ae^{-|\tau|/\tau_1} + be^{-|\tau|/\tau_2}$ [5]. The coefficients a and b represent the amplitudes of submicrosecond antibunching and bunching respectively. τ_1 and τ_2 represent the decay rates of these processes. We extract a lifetime of $\tau_1 = 3.52(34)$.

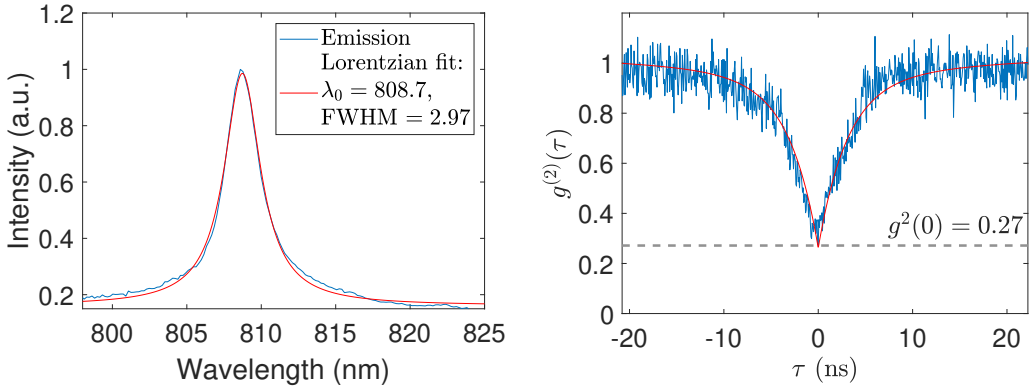

Figure 3.20: Left: Single photon spectral line peaking at 808.7 nm. A pump laser of 520 nm is used. It is apparent from the figure that the emission line is subject to broadening. A Lorentzian fit suggests the broadening mechanisms are predominantly homogeneous in nature, which is to be expected for a solid-state emitter (see section 2.4.3). Right: Second-order auto-correlation measurement of the emission corresponding to the spectral line in the left figure. Integration time is approximately 12 hours. The count rates during measurement are $\sim 8.9 \times 10^3\,\mathrm{s}^{-1}$ and $\sim 9.0 \times 10^3\,\mathrm{s}^{-1}$ during excitation, and $\sim 4.6 \times 10^2\,\mathrm{s}^{-1}$ and $\sim 9.8 \times 10^2\,\mathrm{s}^{-1}$ dark counts. From the fit a lifetime of $\tau_1 = 3.52(34)$ is extracted. We measure $g^{(2)}(0) = 0.27$ which is signature of single photon emission.

Response functions of optical setup

Only for a ratio of decay time (τ_1) to timing jitter (δt) $\tau_1/\delta t > 10$ does the measured $g^{(2)}(0)$ approach the real amplitude of the second-order correlation function [6]. To establish whether this condition is satisfied we have attempted to evaluate the response functions of our optical setup. The measured jitter values corresponding to the two APDs of approximately 1.3 ns and 720 ps make for ratios $\tau_1/\delta t < 5$ (see figure 3.21). According to the manufacturer, the timing resolution depends on the exact position on the active area that the photon is incident on. In the center of the active area, a timing resolution of about 220 ps may be expected. Moving 120 μm off-center however increases timing resolution to approximately 800 ps. Imperfect alignment therefore may be the cause of the sub-optimal jitter. The jitter measurements should be redone after more careful alignment to confirm that the measured $g^{(2)}(0)$ is an accurate representation of the real amplitude of $g^{(2)}(0)$. As a large δt corresponds to a large spread in measured photon arrival time, larger jitter would make for a bias towards higher $g^{(2)}(0)$ values, allowing us to use the measured value of $g^{(2)}(0)$ as an upper limit regardless. A too small $\tau_1/\delta t$ could however affect the measured lifetime. For a proper analysis, the fit function should be convoluted with an accurate instrument response function.

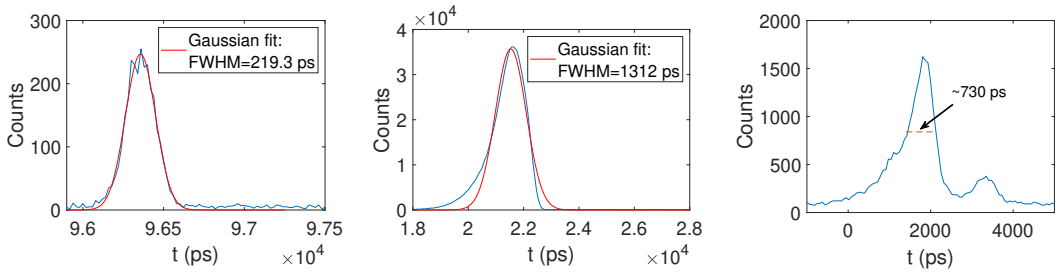

Figure 3.21: Response functions obtained using pulsed laser detected by SNSPD (left), APD1 (middle) and APD2 (right). The resolution of APD2 is significantly lower than that of APD1. The jitter of APD2 in particular is large enough to significantly affect second-order autocorrelation measurements performed on emitters of comparable nanosecond lifetime. The measurement with SNSPD is performed in an attempt to establish that the response of the APDs were the limiting factor, and not the laser pulse width. There were difficulties with regards to maintaining a constant laser pulse width however. The laser pulse width appeared to depend on intensity. The pulsed laser was directly fiber coupled to the SNSPDs, whereas it was sent through the entire optical setup to couople to the APDs. Measurements of SNSPD response and APD response therefore demanded different levels of intensity, giving different pulse widths.

3.4. Final configuration of experimental setup

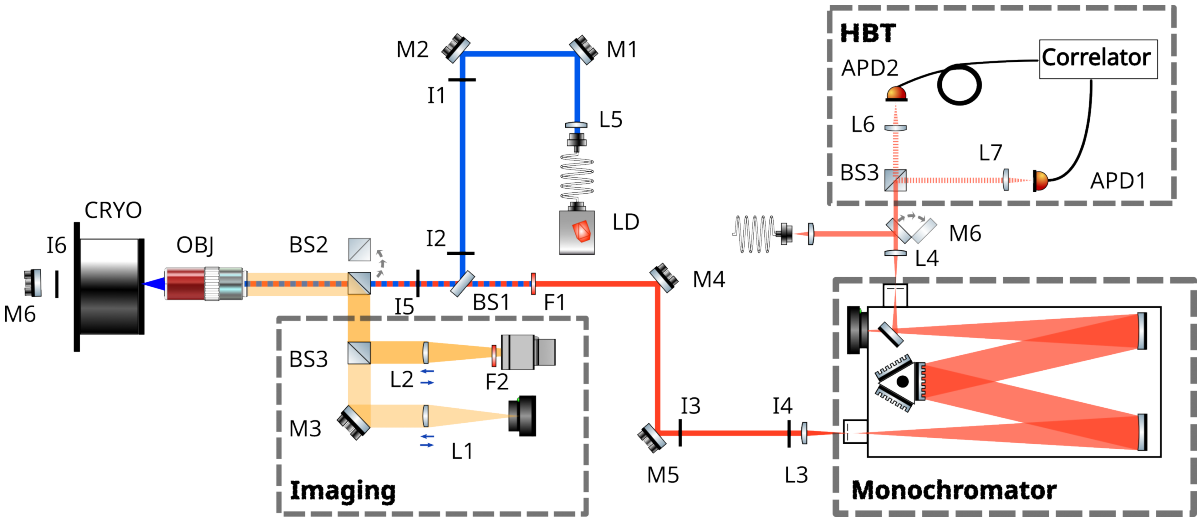

Figure 3.22: Schematic of the final version of the entire optical setup.

Here we give a a brief description of the final configuration of the experimental setup in its entirety, including references to the datasheets of optical components where relevant.

The sample is mounted on a two-axis translation stage in a continous flow cryostat (CRYO, [7]). Excitation laser light (blue in schematic) is focused onto the sample using a 50X infinity corrected objective with a numerical aperture of 0.42 (OBJ, [8]) and a working distance of 17.26 mm. The same objective collects reflected and photoluminescent light from the sample (red in schematic).

A flippable 50:50 beamsplitter (BS1) allows for imaging of the sample by simultaneously directing illuminating light onto the sample and light reflected off the sample onto a 3/2 inch cmos sensor of a camera via a a second 50:50 beamsplitter (BS2), mirror (M3) and focussing lens ($f = 17\,\mathrm{cm}$).

For excitation, either a 453 nm, 512nm or 520nm laser diode is used. The laser diode is coupled to the optical system via an optical fiber and collimating lens. Two mirrors are used to direct the beam through two irises (I1, I2) for alignment. The excitation laser light is then reflected by a 33:67 pellicle beam splitter (BS1, [9]) into the objective.

Collected light is filtered (F) to suppress excitation light from the signal and directed into a monochromator (Acton Spectrapro SP2750 [10]) via two alignment mirrors (M4, M5), two aligning irises (I3, I4) and a convex lens (L1, $f = 75\,\mathrm{mm}$, AR-coated) focussed on the monochromator's input slit. The monochromator has a maximum resolution of 0,023 nm at 435.8 nm and a mechanical scan range of

0-1400nm. It is equipped with three blazed gratings each of different groove density: 150 g/mm, 600 g/mm and 1800 g/mm. Additionaly, it has a built-in flippable mirror that when initiated directs the light that is now filtered by the grating through an output port. The filtered light is then either coupled to a fiber (FC1) or send into a Hanbury-Brown and Twiss (HBT) interferometer, depending on the position of a flippable mirror (FM1).

When fiber coupled, the signal can be further processed with fiber optical components (filters, beamsplitters, polarizers etc.) and/or directed to SNSPDs [11], located elsewhere in the lab.

The HBT consists of a 50:50 beamsplitter (BS3) seperating into two beams, which both are directed via a focussing lens (L2, L3, $f = 35\,\mathrm{mm}$ AR-coated) onto the $180\,\mu\mathrm{m}$ diameter active area of a single-photon avalanche diode operating in geiger-mode (APD1, APD2, SPCM-AQRH-TR [12]) with a photon detection efficiency $> 40\%$ within a range of 500-900 nm. Correlation measurements were done using a time-correlated single photon counting module (PicoHARP300, [13]).

Bibliography

[1] Ali W. Elshaari, Iman Esmaeil Zadeh, Andreas Fognini, Michael E. Reimer, Dan Dalacu, Philip J. Poole, Val Zwiller, and Klaus D. Jöns. On-chip single photon filtering and multiplexing in hybrid quantum photonic circuits. *Nature Communications*, 8, 12 2017.

[2] Alexander Senichev, Zachariah O Martin, Samuel Peana, Demid Sychev, Xiaohui Xu, Alexei S Lagutchev, Alexandra Boltasseva, and Vladimir M Shalaev. Room temperature single-photon emitters in silicon nitride.

[3] Sixin Zhu, Yongpeng Wu, Xinling Liu, Zhirui Gong, Hai Huang, and Qi Qin. Tuning the optical band gap of monolayer wse2 in ferroelectric field-effect transistors. *Ceramics International*, 48:14231–14236, 5 2022.

[4] Christian Kurtsiefer, Patrick Zarda, Sonja Mayer, and Harald Weinfurter. The breakdown flash of silicon avalance photodiodes-backdoor for eavesdropper attacks?, 2018.

[5] Stefania Castelletto, Brett C. Johnson, Cameron Zachreson, David Beke, István Balogh, Takeshi Ohshima, Igor Aharonovich, and Adam Gali. Room temperature quantum emission from cubic silicon carbide nanoparticles. *ACS Nano*, 8:7938–7947, 8 2014.

[6] Svetlana Khasminskaya, Felix Pyatkov, Karolina Słowik, Simone Ferrari, Oliver Kahl, Vadim Kovalyuk, Patrik Rath, Andreas Vetter, Frank Hennrich, Manfred M. Kappes, G. Gol'tsman, A. Korneev, Carsten Rockstuhl, Ralph Krupke, and Wolfram H. P. Pernice. Fully integrated quantum photonic circuit with an electrically driven light source. *Nature Photonics*, 10:727–732, 11 2016.

[7] Konti-cryostat-mikro datasheet. Available at `http://www.cryovac.de/downloads/konti_mikro.pdf`.

[8] 50x mitutoyo plan apo nir infinity corrected objective datasheet. Available at `https://www.edmundoptics.eu/p/50x-mitutoyo-plan-apo-nir-infinity-corrected-objective/6836/`.

[9] Bp133 product-page. Available at `https://www.thorlabs.com/thorproduct.cfm?partnumber=BP133`.

[10] Princeton Instruments. Operating instructions acton series sp-2750 0.750 meter focal length triple grating imaging monochromator / spectrograph acton sp-2750 operating instructions. Available at `https://usermanual.wiki/Collections/Princeton-Instruments/Public/Manuals/Acton/SP-2750.pdf.html`.

[11] Sq nbtin superconducting nanowire single photon detector datasheet, 2022. Available at `https://singlequantum.com/wp-content/uploads/2022/08/Single-Quantum-Brochure-v2-digital.pdf-2.pdf`.

[12] Excelitas technologies' spcm-aqrh-xx-tr single photon counting module datasheet. Available at `https://www.excelitas.com/product/spcm-aqrh-tr`.

[13] Picoharp 300 stand alone tcspc module with usb interface. Available at https://www.picoquant.com/images/uploads/downloads/7304-picoharp300.pdf.

4

Discussion

4.1. Conclusion

The aim of this master end project has been successfully achieved: an optical setup has been built that allows for the characterization of single-photon emitters. More specifically, the micro photoluminescence (PL) setup can be used for high resolution PL spectroscopy measurements. Additionally, it includes a free-space Hanbury-Brown and Twiss interferometer containing two geiger-mode avalanche photodiodes for second-order correlation measurements. PL measurements are performed on two-dimensional hexagonal Boron Nitride, demonstrating clear anti-bunching indicating single-photon emission.

4.2. Discussion and suggestions for future work

Here we will make some remarks on the results and a number of suggestions for future work.
An interesting observation is that the two hBN PL spectra in figure 3.10 display emission peaks that could be categorized in group 1 and group 2, as defined by [3] respectively. The fact that the 588.1 nm peak accurately resembles the criteria of a group 1 SPE, makes it likely that the emission line is that of a single-photon emitter. Similarly, the peak doublet centered around 715 nm is likely associated with single-photon emission as it shows distinct features of a group 2 emitter. $g^{(2)}(\tau)$ measurements have been performed on the 810 peak exclusively. In order to confirm these suppositions, $g^{(2)}(\tau)$ measurements on the other emission lines should be performed. An interesting side note: the ZPL wavelength of the SPE found in this work is higher than that of any of the 47 emitters reported in [3] (max ZPL 775 nm).
Having mentioned the peak doublet centered around 715 nm, it is suspected that the emission line contains SPE from two separate point defects, located in close vicinity of one another. It would therefore be questionable whether a $g^{(2)}(\tau)$ measurement would display anti-bunching. As it is thought that native point defects in hBN are always coupled to phonon states [2], we would expect the two peaks making up the doublet to be temperature dependent. Cooling the sample down to cryogenic temperatures will then give narrower emission lines, and potentially yield two separated single-photon emission lines entirely, one centered around 714.5 nm, and on centered around 717.3 nm.
Although the optical setup includes a continous flow crystat, we have not been able to put it into operation. A broken translation stage, followed by a broken sealing o-ring caused a delay. The problems have meanwhile been dealt with, and although not thoroughly tested, the cryostat should now be fully operational for future use. Because of the malfunctioning cryostat, the original idea of measuring QDs in nanowire had to be called off.
Moreover, in our attempt to determine the instrument response functions of our setup, we have found a jitter of APD2 in particular that is large enough to significantly affect the correlation measurements. As discussed in the previous chapter however, it is likely that the high jitter values are obtained because of imperfect alignment during the jitter measurements. Namely, an inquiry into the datasheet of the APDs reveals that jitter is highly dependent on the exact location on the active area of photon incidence. Moreover, one would expect the $g^{(2)}$ measurement in figure 3.20 to be more dramatically affected by the large jitter, given that it is of the order of magnitude of the lifetime of the emitter. The

jitter measurements should be repeated in future work after more careful alignment. For a more comprehensive analysis of the correlation measurements, the fit function could then be convoluted with the more carefully obtained response functions of the APDs.
Having state of the art superconducting nanowire single photon detectors (SNSPDs) available, an obvious extension of the setup is to include an in-fiber HBT-interforemeter. Moreover, quantum information technologies in particular require a single-photon source to emit indistinguishable single photons. A measure for single photon indistinguishability is the Hong-Ou and Mandell (HOM) [1] visibility, which is measured using an HOM interferometer. An interesting extension of the setup would be to include the latter, either in-fiber, using SNSPDS, or free-space.
In order to characterize the optical properties of entire photonic integrated circuits (PICs) or components thereof, a second interesting extension would be to include a second optical path to open up the possibility of side-excitation and side-collection. This has been worked towards during this master project as discussed in the previous chapter but has not been used nor finalized as we have not come to measure on PICs.

Bibliography

[1] C. K. Hong, Z. Y. Ou, and L. Mandel. Measurement of subpicosecond time intervals between two photons by interference. *Phys. Rev. Lett.*, 59:2044–2046, 11 1987.

[2] Nicholas R. Jungwirth, Brian Calderon, Yanxin Ji, Michael G. Spencer, Michael E. Flatté, and Gregory D. Fuchs. Temperature dependence of wavelength selectable zero-phonon emission from single defects in hexagonal boron nitride. *Nano Letters*, 16:6052–6057, 10 2016. ISSN 1530-6984. doi: 10.1021/acs.nanolett.6b01987.

[3] Toan Trong Tran, Christopher Elbadawi, Daniel Totonjian, Charlene J. Lobo, Gabriele Grosso, Hyowon Moon, Dirk R. Englund, Michael J. Ford, Igor Aharonovich, and Milos Toth. Robust multicolor single photon emission from point defects in hexagonal boron nitride. *ACS Nano*, 10:7331–7338, 8 2016. ISSN 1936-0851. doi: 10.1021/acsnano.6b03602.

A

Appendix A

A.1. Chronological overview

Brief overview of progression in chronological order.

- **Weeks 20**:
  Objectives achieved: there is a working imaging system; A lens focusing light on to the input slit of the spectrometer is mounted on to a linear three axes stage; reflected light from sample is directed towards spectrometer input.
  Summary: There were difficulties with getting the system into alignment. Moreover, it took some time to achieve the proper illumination. The initial light source was too bright and had to be filtered such that the light reflected from BS3 did not saturate the camera. Then initially, when an image was obtained, the field of view was too small. By installing tube lens of focal length 17 cm and a collimating lens of focal length 10 cm for the illuminating light, the image was enlarged to a size that was sufficiently large to work with (see figure A.1). A Heleum-Neon laser was installed for purposes of alignment and testing the spectrometer with. Its beam is close to an ideal Gaussian beam, therefore, when He-Ne is properly aligned with the objective, sample, and imaging system, upon moving the objective towards and from the sample, the image should display a scanning through concentric circular diffraction rings. By this time, it is clear that one of the two translation stages in the cryostat is not working. This is a problem as both stages are needed in order to isolate and excite a single photon source.

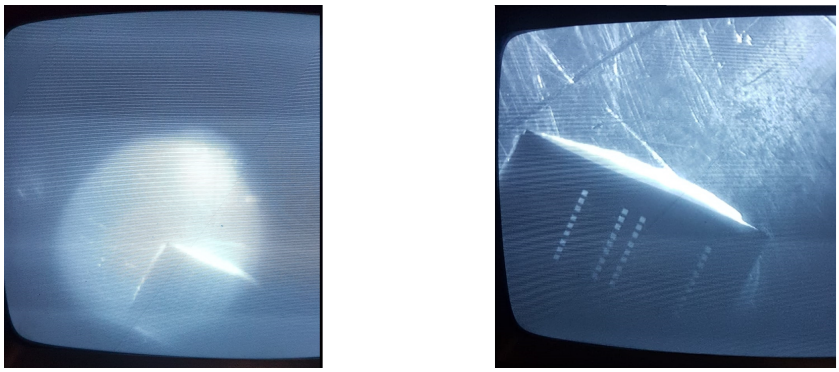

Figure A.1: Before (left) and after (right) installation of appropriate lenses for the imaging system.

- **Week 21-24**:
  Objectives achieved: The first spectra are obtained; setup is redesigned: cryostat replaced by 3-axes stage, side excitation.
  Summary: For spectroscopy, the CCD camera needs to be cooled down with liquid nitrogen which I learned this week how to obtain and handle. There appears to be an issue with acquired

spectra however: even when intensity of incoming light is low, the measured spectra indicate high intensity and independent of the intensity of the incoming light, the CCD images display entire columns of illuminated pixels. In parallel, attempts are made by the technician to fix the malfunctioning cryostat translation stage without success. Furhtermore, the setup is redesigned. It now allows for the possibility of side-excitation and the cryostat is replaced by a 3-axes translation stage on which (room temperature) samples can be mounted. Apart from QDs in nanowire that require a fully operational cryostat, there are no single photon sources available which stalls further development of the setup. Time is spent on studying quantum optics and endeavours are made to obtain single photon emitters that are operable at room temperature.

- **Week 25-26**:
  Objectives achieved: Obtained hBN emitters from KTH Royal Institute of Technology in Stockholm; CCD issue is resolved.
  Summary: A sample of hBN dropcast on Si/SiO_2 is shipped over to us from KTH Stockholm. Numerous spectra are taken from the hBN dropcast sample using pump lasers of different frequencies in search for single photon emission but without success. Other single photon sources are being arranged for, namely, WSe_2 monolayers from the University of Exeter. The cryostat is shipped over to its manufacturers in Germany for further inspection. The problem of the saturating CCD image is solved by installing a shutter in front input slit of the monochromator, as a CCD relies on having a certain amount of readout time during which it is not exposed. This is elaborated in more detail in section **??**

- **Week 27-28**:
  Objectives achieved: WSe_2 obtained; first spectra taken of assumed single photon emission.
  Summary: A sample of WSe_2 on SiO_2 substrate is sent over. Together with the sample, microscope images of a monolayer are provided. The sample is covered with positional markings allowing for the monolayer to be readily found. PL-spectroscopy measurements are performed. Also, considerations are made to purchase type IIa diamond. After inquiring with Element Six, it became clear that the NV-center density is too high for a single emitter to be isolated. Moreover, delivery time was expected to be 20 weeks.
- **Week 29**:
  Objectives achieved: N/A
  Summary: A Fourier optics analysis is performed to determine the lens and slit opening to be used. The beam diameter of collected light is approximated to be $5\,\mathrm{mm}$. A slit opening of $50\,\mu\mathrm{m}$ is obtained and it is calculated that a lens with focal length of $75\,\mathrm{mm}$ is needed for spectrometer input. Two lenses of said focal length are ordered. Two new pellicle beamsplitters with more desirable properties are ordered.
- **Week 30-34**:
  Objectives achieved: Measured spectra of annealed SiN; Expanded setup to allow for fiber coupling, bypassing the monochromator.
  Summary: In week 30 the WSe_2 monolayer sample was accidentally crushed by the objective making it impossible to use it for further investigation. Inspired by Senichev et. al., whom in their publication [1] report on single-photon emitters in Silicon Nitride, Bruno Lopez Rodrigues prepared three SiN samples. The samples are manually scanned in search of single photon emission, without succes. A scanning (confocal) microscope set up is necessary for a more thorough investigation of the SiN samples which is a suggestion for future work.
  The setup was expanded by allowing for the possibility to couple the photoluminescent light into a fiber coupled spectral filter, bypassing the spectrometer. In week 30 I contacted Ronald Hanson asking whether he had any room temperature single photon sources that I could use. He linked me up with his phD student Yannik Herrmann who had a sample of NV-centers in diamond behind solid immersion lenses available. He was not sure whether the sample was still usable he suspected the sample to have been contaminated in a recent experiment. I spent a day in qutech measuring the sample with a scanning con-focal microscope. However, contamination indeed appeared to prevent excitation and/or collection of the NV-centers.
- **Week 35-36**:
  Objectives achieved: Spectra measured that suggest single photon emission from hBN.
  Summary: A new sample of hBN dropcast onto Si/SiO_2 is sent over. This time an hBN solution

is used that is known to contain single photon emitters. As a double check, a PL spectrum of the sample is taken before shipping, confirming the presence of multiple emitters. Indeed, the spectra that are measured now are suggestive of single photon emission. In particular, a narrow peak is found at $810\,\mathrm{nm}$ which is compatible with a band-pass filter that is available in the lab. Also, the cryostat is back from Germany in working order. Part of week 36 is spent building a free space HBT setup for $g^{(2)}(\tau)$ measurements.

- **Week 36**
  Summary: Attempting different HBT designs. Correlation measurements are still not possible because a particular inverter is needed. Inverter is ordered on September 8. 810-emitter is aligned to one SAPD measuring 6e4 counts while pumping, and 6e2 in the dark. Lifetime measurements of 810 -emitter are attempted with pulsed laser and one SAPD (see figure A.2). There appears to be an issue with the pulsed laser. Amplitude of pulses is possibly too low for causing sufficient excitation.

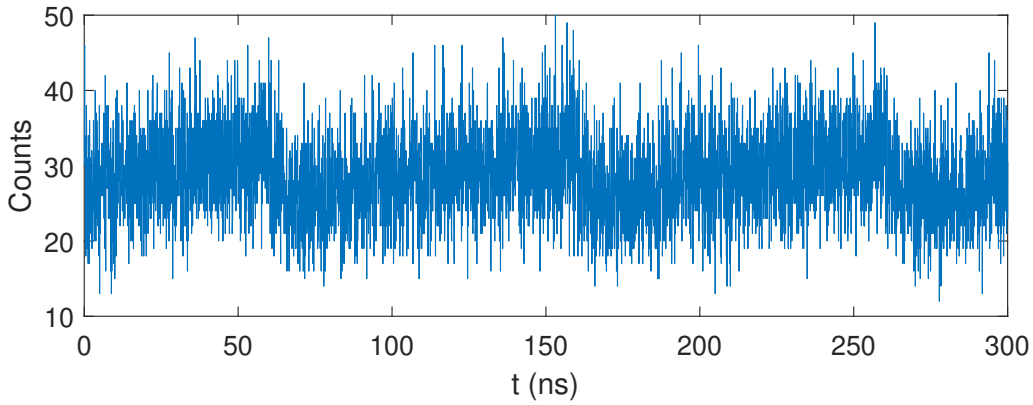

Figure A.2: Attempt at lifetime masurement with pulsed laser.

- **Week 37-38**:
  Objectives achieved: Cryostat assembled and partially operational; First $g^{(2)}(\tau)$ measurements.
  Summary: As the cryostat was disassembled for inspection, it had to be reassembled. The cryostat stages are now working but we discover an o-ring is broken. In an attempt to pump vacuum, we discover that the break in the o-ring is the cause of a leak. The cryostat is again disassembled. The o-ring is of an uncommon size and therefore hard to get hold of. The technician tries a quick fix by gluing the rubber o-ring, but in vain: the cryostat is still leaking. In a third attempt vacuum grease is used to seal off the cryostat. This fixes the problem: the cryostat is brought down to a pressure sufficiently low for our purposes of helium cooling.
  On September 22 we have the inverter that is needed for $g^{(2)}(\tau)$ measurements and on the same day the first $g^{(2)}(\tau)$ measurements are performed (figure 3.16). A problem is encountered: two atypical sharp peaks appear approximately 10 ns apart. The hypothesis is that the peaks are caused by crosstalking between the two SAPDs via photons emitted by a detection event. The characteristics of this particular photoemission, or 'breakdown flash' is investigated in [2], As the spectrum of the breakdown flash overlaps with the spectrum of the 810-emitter, reduction of the crosstalk by means of spectral filtering will also reduce the light of interest. Therefore, an attempt is made to apply spatial filtering of the breakdown flash by slightly rotating the beamsplitter and installing irises at each of its output ports.
- **Week 39**
  Summary: A scheduled power outtage prevents any activities in the lab. Time is spent on writing.
- **Week 40-41**:
  Objectives achieved: Cryostat included in setup. *Summary*: Redoing setup including cryostat
- **Week 42-43** Summary: writing.
- **Week 44** *Objectives achieved*: First second-order auto correlation measurement displaying clear anti-bunching. Summary: An overnight $g^{(2)}(\tau)$ measurement of the hBN emitter shows clear anti-

bunching with a value of $g^{(2)}(0) < 0.3$. An attempt is made to perform additional measurements inclding a $g^{(2)}(\tau)$ measurement on the broken WSe_2 sample but without success.

A.2. Fourier optics analysis of spectrometer to decide on slit width and lens focal length

Here we use one-dimensional Fourier optics to calculate in approximation the optimal slit width and lens focal lens to use for guiding light into the spectrometer. The distance from the slit to the collimating mirror is D, the width of the slit is δ, the collimating mirror is approximated to be of square shape of width and height $a = 68\,\mathrm{mm}$. We assume the slit width to be much smaller than D ($\delta << D$) and the angle the diffracting light makes with the optical axis of the system (θ) to remain small ($a << D$). Therefore, our system is in the Fraunhofer regime from which we know that the intensity profile of the diffracted light is given by:

$$I(\theta) \propto sinc^2\left[\frac{\pi\delta}{\lambda}\theta\right]. \tag{A.1}$$

We choose our parameters such that the first zeros of $I(\theta)$ are on the edges of the collimating mirror. The angle corresponding to the edge of the mirror is given by

$$\theta_{min,0} = \tan^{-1}\left(\frac{a/2}{D}\right) \approx 0.0453. \tag{A.2}$$

By equating the argument of (A.1) with π and subtstituting $\theta_{min,0}$ for θ, we find the following slit width δ as a function of wavelength λ will produce the diffraction intensity profile that we are looking for:

$$\frac{\pi\delta}{\lambda}\theta_{min,0} = \pi, \tag{A.3}$$

$$\delta \approx 22\lambda. \tag{A.4}$$

For wavelengths of $400\,\mathrm{nm}$ and $1000\,\mathrm{nm}$ for example, we find respectively a slit opening of $\delta \approx 9\,\mu\mathrm{m}$ and $\delta \approx 22\,\mu\mathrm{m}$. As the light that is investigated in the experiments is within the range of $400 - 1000\,\mathrm{nm}$, these two values are used as approximate lower and upper limits of the slit opening between which a slit width is empirically determined that optimizes the signal.
To find the appropriate lens to focus the light onto the slit and into the spectrometer, we require the diameter of the focussed spot size to be equal to the slit width. From §5.9 in [3] we calculate the spot size diameter (w_0) using:

$$w_0 = \frac{4f\lambda}{\pi w_s}, \tag{A.5}$$

where f is the focal length of the lens, λ the wavelength, and w_s the diameter of the beam at the lens. Estimating the beam diameter on the lens to be within a range of $3 - 6\,\mathrm{mm}$, we find that equations A.4 and A.5 suggest using a lens with focal length within a range of approximately $5 - 10\,\mathrm{cm}$. A $f = 7.5\,\mathrm{cm}$ lens is used in the experiments [4].

A.3. hBN Sample fabrication

The hexagonal Boron Nitride sample was fabricated in June 2022 by Valentin Haemmerli (University of Exceter). The fabrication process is described by him as follows:
Undoped silicon with a 300 nm layer of thermally grown silicon dioxide (commercially available wafer, Inseto) was diced into 10 mm chips and cleaned in 85°C acetone for 10 minutes, before ultrasonication in acetone, and then isopropanol, each for 10 minutes at 80 kHz/40% power. An additional oxygen plasma cleaning step was performed (JLS RIE80, 4 min process time, 30 W RF power, 50 mTorr chamber pressure, 50 SCCM O_2), before the substrate was pre-baked on a hotplate for at least 10 minutes at 110□C. 2 ml of pristine boron nitride (BN) nanoflake solution (Graphene Supermarket) was transferred to a beaker and ultrasonicated for 5 minutes 80 kHz/40% power. Six to seven drops (using a micropipette) were evenly and centrally transferred to the hot substrate, allowing time for the solvent to evaporate in between drops and for the sample to heat back up. Finally, an annealing step (Jipelec

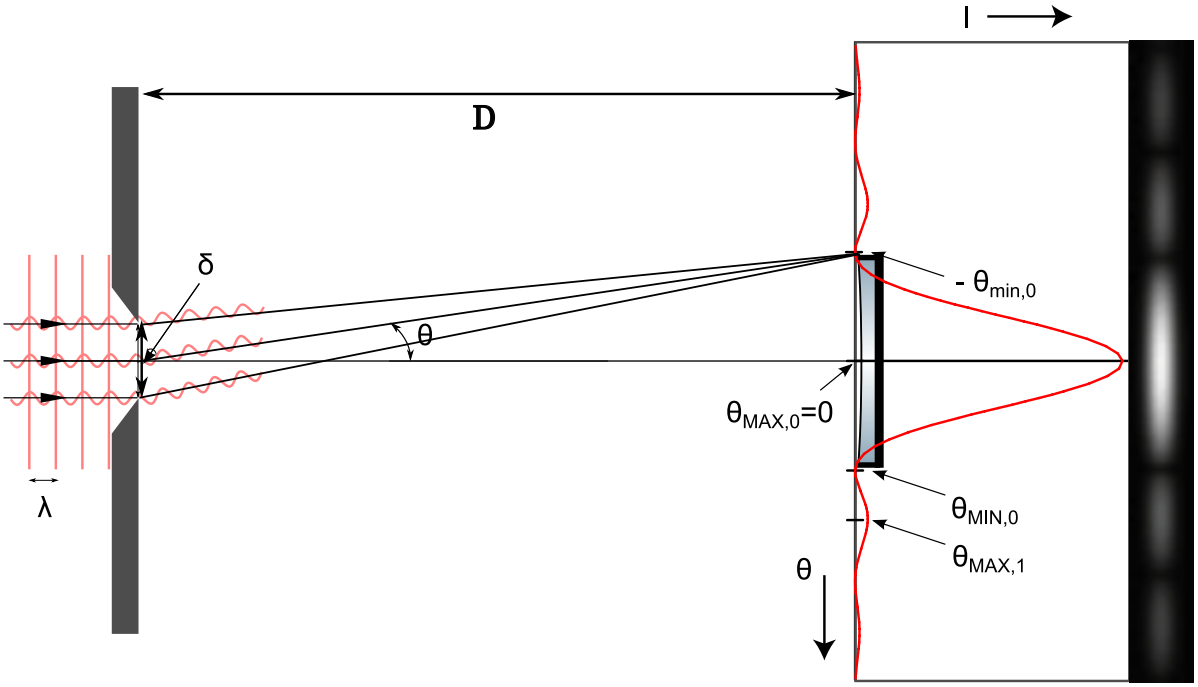

Figure A.3: Schematic of monochromator input slit diffraction. A slit opening is chosen that creates an optimal diffraction pattern in the plane of the collimating mirror, having the first zeroes overlap with the edges of the mirror as shown in the figure.

Rapid Thermal Annealer) was performed at 700°C for 15 minutes in argon atmosphere. Subsequently, the sample was baked for a further 5 minutes at 110°C before packing and vacuum sealing.

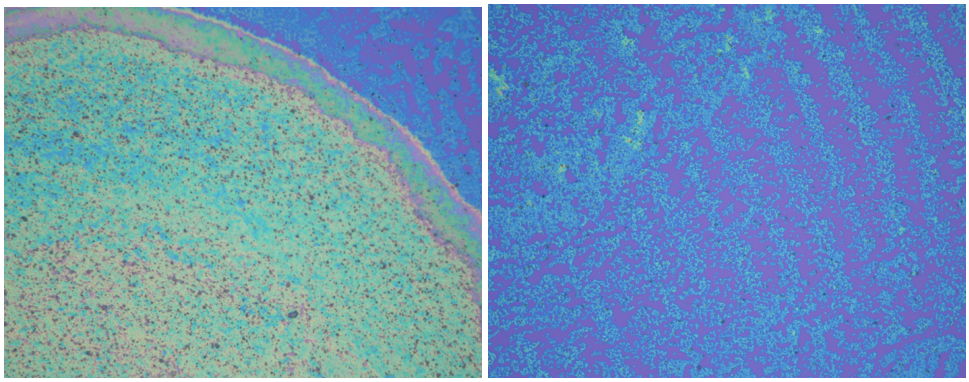

Figure A.4: Optical microscope images of the dropcast hBN sample. Left shows an area of high nanoflake density. The density of nanoflakes on the right is more sparse and it is therefore more likely to find isolated single-photon emitters here. The emitters that were studied in this thesis were found in a low density area akin to that depicted in the right figure.

A.4. Extra figures

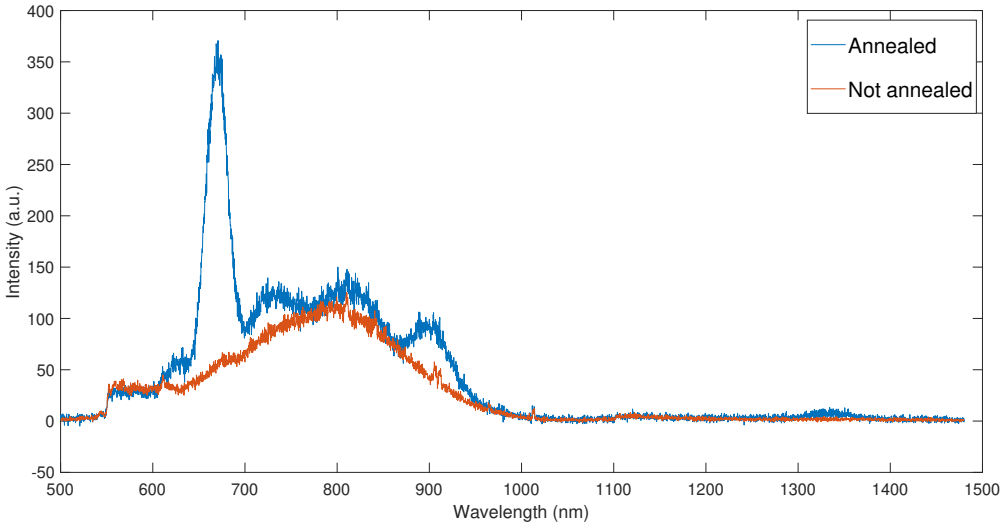

Figure A.5: Photoluminescence spectrum of silicon carbide that is annealed under high temperature versus PL spectrum of silicon carbide that has not been annealed. Peak is possibly PL emission of underlying substrate that has been exposed by the breaking apart of the SiC film. Further investigation is required to determine the exact origin of the observed peak.

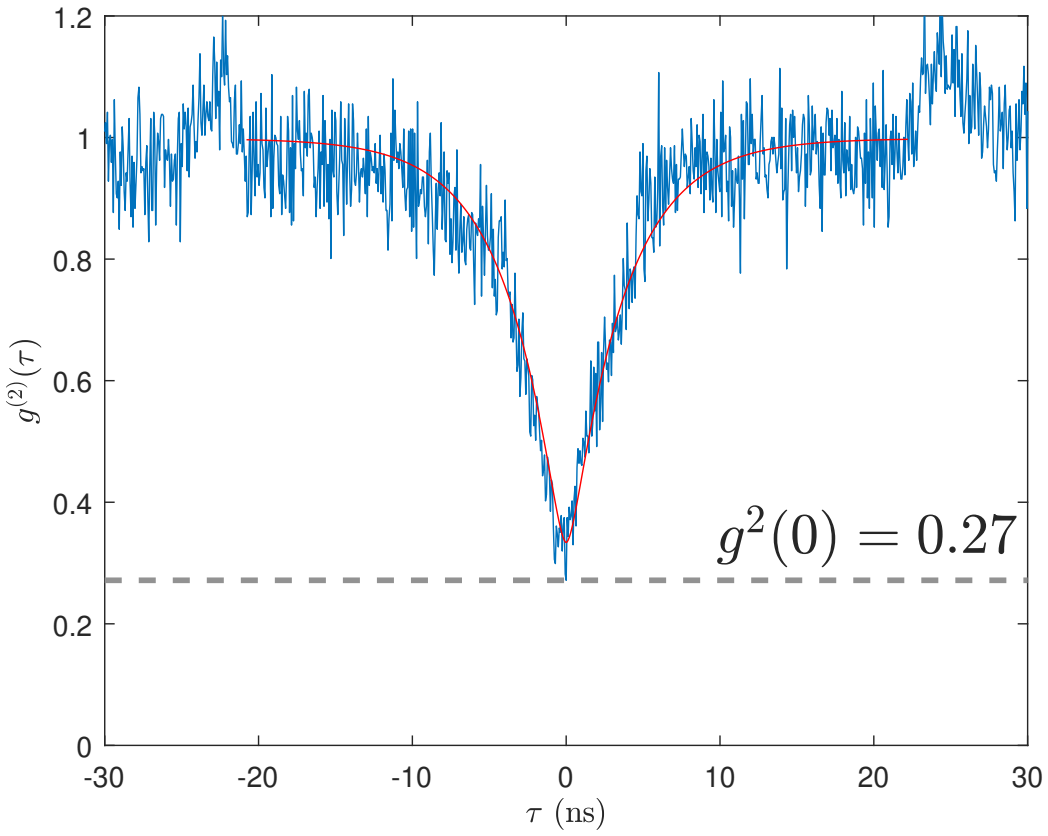

Figure A.6: $g^{(2)}$ data of 3.20 plotted over a wider range of τ. Two remarkable peaks are observed separated from one another by approximately 50 ns. The time separation is too far apart for the peaks to be explained by cross-talking between detectors.

Bibliography

[1] Alexander Senichev, Zachariah O Martin, Samuel Peana, Demid Sychev, Xiaohui Xu, Alexei S Lagutchev, Alexandra Boltasseva, and Vladimir M Shalaev. Room temperature single-photon emitters in silicon nitride.

[2] Christian Kurtsiefer, Patrick Zarda, Sonja Mayer, and Harald Weinfurter. The breakdown flash of silicon avalance photodiodes-backdoor for eavesdropper attacks?, 2018.

[3] Wolfgang Demtroder. Gaussian beams, 1998.

[4] La1608-b product-page. Available at `https://www.thorlabs.com/thorproduct.cfm?partnumber=LA1608-B`.

B

Code

Script used to read spectroscopy data saved in .SPE extension.

```
    function sp = loadSPE(filename)
%
% sp=loadSPE(filename)
%   Loads PrincetonInstrument Lightfield .spe files into a matlab structure that contains
%   1D or 2D data in the sp.int(intensity) field
%   1D: 'sp.int' returns a 1D intensity array.
%   2D: 'sp.int' returns a 2D intensity matrix.
%   3D: 'sp.NumFrames' returns the frames number of a video,
%       'sp.int' has a third dim of frames, haven't tested.
%   In addition,
%   'sp.wavelength' returns the wavelength array (column array)
%   'sp.expo_time' returns the exposure time of the experiment in [second]
%
% This code is rewritten since the .spe file format totally changed in version 3.0
% Basically it is a mixture of binary data (as 2.0 version) and newly added XML ASCII footer.
% We need to read the offset location from the binary part, which tells the starting position of the
% XML data, and then read from there.
%
% Known issue: Temporarily do not support multiple Region of Interest.
% Please refer to ftp://ftp.piacton.com/Public/Manuals/Princeton%20Instruments/SPE%203.0%20File%20Format%20Specification.pdf
% to learn how to extract the multiple data blocks.

% Author: Zhaorong Wang
% Date: 2016-02-19

%------------ Modification History --------------------
% 2015-02-22 by Zhaorong: Revised the data fields; Added the back-compatibility of SPE 2.0
% 2015-02-21 by Zhaorong: Finished the basic functionalities.

%============ Program Begins ===============================================

% Test filename existence
if exist(filename)~=2
    if exist([filename '.spe'])==2  % Append with .spe and try again
        filename=[filename '.spe'];
    else
        error(['File "' filename '" does not exist!']);
        sp=[];
        return
    end
end

% If file exists, open it with a file id.
fid = fopen(filename, 'r');
if fid==-1
    errordlg('Can''t read file (insufficient rights?)!');
    sp=[];
```

```
48      return
49  end
50
51  % Read basic information from the binary header
52  header = readheader(fid); % readheader is a function defined later
53  sp = struct();
54  if (header.xdim == 0 || header.ydim == 0)
55      errordlg('Zero data dimensions! Probably due to multiple Region of Interest chosen');
56      return
57  end
58  sp.xdim = header.xdim;
59  sp.ydim = header.ydim;
60
61  % Read actual data and store columnwise in .int field
62  fseek(fid,4100,'bof');  % Move the file pointer to the beginning of the intensity data
63
64  switch header.Datatype
65      case 0
66          typ='float32';
67      case 1
68          typ='int32'; %seems to work for many of our files
69      case 2
70          typ='int16';
71      case 3
72          typ='uint16';
73  end
74
75  for kk=1:header.NumFrames
76      for ii=1:header.ydim
77          sp.int(ii,:,kk)=fread(fid,header.xdim,[typ '=>double']);
78      end
79  end
80
81  % If version>=3.0, get calibration data from the XML footer
82  if header.version>=3.0
83
84      % Find and save the XML footer into a temp.xml file
85      fseek(fid, header.XML_offset, 'bof');
86      segsize = 10000;    % Read 10kb a time
87      XML_fileID = fopen('temp.xml','w');
88      while ~feof(fid)
89          currData = fread(fid, segsize);
90          if ~isempty(currData)
91              fwrite(XML_fileID, currData);
92          end
93      end
94      fclose(XML_fileID);
95
96      % Search for the 'Wavelength' and 'ExposureTime' tags and save their data
97      DOMnode = xmlread('temp.xml');
98      sp.wavelength = readXMLdata(DOMnode, 'Wavelength');
99      sp.expo_time = readXMLdata(DOMnode, 'ExposureTime')./1000; % Convert from ms to second
100     % If you want to save other data important for your experiement, you can call this
            function
101
102     if exist('temp.xml', 'file')==2 % Delete the temp file when done.
103         delete('temp.xml');
104     end
105
106 elseif header.version>=2.0  % For SPE2.0, read calibration data from the header
107     % Create wavelength axis from calibration polynomial
108     sp.wavelength=(header.Calibpoly(1)+...
109           header.Calibpoly(2)*(header.startx:header.startx+header.xdim-1)+...
110           header.Calibpoly(3)*(header.startx:header.startx+header.xdim-1).^2)';
111     sp.expo_time = header.Exposure;
112 else
113     errordlg('Unsupported Version! Only support 2.x and 3.x');
114 end
115
116 fclose(fid);
117
```

```
return

function header=readheader(fid)

%each entry in headerinfo corresponds to data that is read into the header
%structure of the resulting Matlab spectrum structure
%fields are: Name, Offset (Byte number in .spe file), Type (Datatype),
%Length (for Arrays of Type), and Load (whether or not this item should be
%read)
c=1;
headerinfo(c)=struct('Name','Exposure', 'Offset',10,  'Type','float',  'MType','double','
    Length',1,'Transpose',1,'Load',1); c=c+1;
headerinfo(c)=struct('Name','Date',     'Offset',20,  'Type','char',   'MType','char',  '
    Length',10,'Transpose',1,'Load',1); c=c+1;
headerinfo(c)=struct('Name','Time',     'Offset',172, 'Type','char',   'MType','char',  '
    Length',7,'Transpose',1,'Load',1); c=c+1;
headerinfo(c)=struct('Name','xdim',     'Offset',42,  'Type','uint16', 'MType','double','
    Length',1, 'Transpose',1,'Load',1); c=c+1;
headerinfo(c)=struct('Name','ydim',     'Offset',656, 'Type','uint16', 'MType','double','
    Length',1, 'Transpose',1,'Load',1); c=c+1;
headerinfo(c)=struct('Name','Datatype', 'Offset',108, 'Type','int16',  'MType','double', '
    Length',1, 'Transpose',1,'Load',1); c=c+1;
headerinfo(c)=struct('Name','NumFrames','Offset',1446,'Type','int32',  'MType','double','
    Length',1, 'Transpose',1,'Load',1); c=c+1;
headerinfo(c)=struct('Name','XML_offset','Offset',678,'Type','uint64',  'MType','double','
    Length',1, 'Transpose',1,'Load',1); c=c+1;
headerinfo(c)=struct('Name','version',  'Offset',1992,'Type','float32',  'MType','double','
    Length',1, 'Transpose',1,'Load',1); c=c+1;
headerinfo(c)=struct('Name','startx',   'Offset',1512,'Type','uint16', 'MType','double','
    Length',1, 'Transpose',1,'Load',1); c=c+1;
headerinfo(c)=struct('Name','Calibpoly','Offset',3263,'Type','float64','MType','double','
    Length',6, 'Transpose',1,'Load',1); c=c+1;
headerinfo(c)=struct('Name','BckGrdApplied','Offset',150,'Type','char','MType','double', '
    Length',1, 'Transpose',1,'Load',1); c=c+1;
headerinfo(c)=struct('Name','FltFldApplied','Offset',706,'Type','char','MType','double', '
    Length',1, 'Transpose',1,'Load',1); c=c+1;
headerinfo(c)=struct('Name','Gain',     'Offset',198,  'Type','int16', 'MType','double','
    Length',1, 'Transpose',1,'Load',1);

for i=1:length(headerinfo)
    if headerinfo(i).Load
        fseek(fid,headerinfo(i).Offset,'bof');
        if headerinfo(i).Transpose
            header.(headerinfo(i).Name)=fread(fid,headerinfo(i).Length,[headerinfo(i).Type
                '=>' headerinfo(i).MType])';
        else
            header.(headerinfo(i).Name)=fread(fid,headerinfo(i).Length,[headerinfo(i).Type
                '=>' headerinfo(i).MType]);
        end
    end
end

return

function data = readXMLdata(DOMnode, tag)
% This function can read the data from a given tag of a DOMnode (Document Object Model node)
    returned by xmlread()
    theNodeList = DOMnode.getElementsByTagName(tag);
    theElement = theNodeList.item(0);
    the_str = char(theElement.getFirstChild.getData);
    the_cellarr = textscan(the_str, '%f64,');   % The wavelength data is float64 delimited by
         comma
    data = the_cellarr{1,1};
return
```

Script used to read PicoQuant correlation data as saved in .PHU extension.

```
    % Read_PHU.m    Read PicoQuant Unified Histogram Files
% This is demo code. Use at your own risk. No warranties.
% Marcus Sackrow, Michael Wahl, PicoQUant GmbH, December 2013
% Updated by Michael Wahl, PicoQUant GmbH, June 2016

```

```
% Note that marker events have a lower time resolution and may therefore appear
% in the file slightly out of order with respect to regular (photon) event records.
% This is by design. Markers are designed only for relatively coarse
% synchronization requirements such as image scanning.

% T Mode data are written to an output file [filename].out
% We do not keep it in memory because of the huge amout of memory
% this would take in case of large files. Of course you can change this,
% e.g. if your files are not too big.
% Otherwise it is best process the data on the fly and keep only the results.

% All header data are introduced as Variable to Matlab and can directly be
% used for further analysis

    clear all;
    clc;
    % some constants
    tyEmpty8      = hex2dec('FFFF0008');
    tyBool8       = hex2dec('00000008');
    tyInt8        = hex2dec('10000008');
    tyBitSet64    = hex2dec('11000008');
    tyColor8      = hex2dec('12000008');
    tyFloat8      = hex2dec('20000008');
    tyTDateTime   = hex2dec('21000008');
    tyFloat8Array = hex2dec('2001FFFF');
    tyAnsiString  = hex2dec('4001FFFF');
    tyWideString  = hex2dec('4002FFFF');
    tyBinaryBlob  = hex2dec('FFFFFFFF');

    % start Main program
    [filename, pathname]=uigetfile('*.phu', 'E:\stijnmep\');
    fid=fopen([pathname filename]);

    fprintf(1,'\n');
    Magic = fread(fid, 8, '*char');
    if not(strcmp(Magic(Magic~=0)','PQHISTO'))
        error('Magic invalid, this is not a PHU file.');
    end;
    Version = fread(fid, 8, '*char');
    fprintf(1,'Tag Version: %s\n', Version);

    % there is no repeat.. until (or do..while) construct in matlab so we use
    % while 1 ... if (expr) break; end; end;
    while 1
        % read Tag Head
        TagIdent = fread(fid, 32, '*char'); % TagHead.Ident
        TagIdent = (TagIdent(TagIdent ~= 0))'; % remove #0 and make more readable
        TagIdx = fread(fid, 1, 'int32');    % TagHead.Idx
        TagTyp = fread(fid, 1, 'uint32');   % TagHead.Typ
                                            % TagHead.Value will be read in the
                                            % right type function
        if TagIdx > -1
          EvalName = [TagIdent '(' int2str(TagIdx + 1) ')'];
        else
          EvalName = TagIdent;
        end
        fprintf(1,'\n   %-40s', EvalName);
        % check Type of Header
        switch TagTyp
            case tyEmpty8
                fread(fid, 1, 'int64');
                fprintf(1,'<Empty>');
            case tyBool8
                TagInt = fread(fid, 1, 'int64');
                if TagInt==0
                    fprintf(1,'FALSE');
                    eval([EvalName '=false;']);
                else
                    fprintf(1,'TRUE');
                    eval([EvalName '=true;']);
                end
```

```
77              case tyInt8
78                  TagInt = fread(fid, 1, 'int64');
79                  fprintf(1,'%d', TagInt);
80                  eval([EvalName '=TagInt;']);
81              case tyBitSet64
82                  TagInt = fread(fid, 1, 'int64');
83                  fprintf(1,'%X', TagInt);
84                  eval([EvalName '=TagInt;']);
85              case tyColor8
86                  TagInt = fread(fid, 1, 'int64');
87                  fprintf(1,'%X', TagInt);
88                  eval([EvalName '=TagInt;']);
89              case tyFloat8
90                  TagFloat = fread(fid, 1, 'double');
91                  fprintf(1, '%e', TagFloat);
92                  eval([EvalName '=TagFloat;']);
93              case tyFloat8Array
94                  TagInt = fread(fid, 1, 'int64');
95                  fprintf(1,'<Float array with %d Entries>', TagInt / 8);
96                  fseek(fid, TagInt, 'cof');
97              case tyTDateTime
98                  TagFloat = fread(fid, 1, 'double');
99                  fprintf(1, '%s', datestr(datenum(1899,12,30)+TagFloat)); % display as Matlab
                        Date String
100                 eval([EvalName '=datenum(1899,12,30)+TagFloat;']); % but keep in memory as
                        Matlab Date Number
101             case tyAnsiString
102                 TagInt = fread(fid, 1, 'int64');
103                 TagString = fread(fid, TagInt, '*char');
104                 TagString = (TagString(TagString ~= 0))';
105                 fprintf(1, '%s', TagString);
106                 if TagIdx > -1
107                    EvalName = [TagIdent '{' int2str(TagIdx + 1) '}'];
108                 end;
109                 eval([EvalName '=[TagString];']);
110             case tyWideString
111                 % Matlab does not support Widestrings at all, just read and
112                 % remove the 0's (up to current (2012))
113                 TagInt = fread(fid, 1, 'int64');
114                 TagString = fread(fid, TagInt, '*char');
115                 TagString = (TagString(TagString ~= 0))';
116                 fprintf(1, '%s', TagString);
117                 if TagIdx > -1
118                    EvalName = [TagIdent '{' int2str(TagIdx + 1) '}'];
119                 end;
120                 eval([EvalName '=[TagString];']);
121             case tyBinaryBlob
122                 TagInt = fread(fid, 1, 'int64');
123                 fprintf(1,'<Binary Blob with %d Bytes>', TagInt);
124                 fseek(fid, TagInt, 'cof');
125             otherwise
126                 error('Illegal Type identifier found! Broken file?');
127         end;
128         if strcmp(TagIdent, 'Header_End')
129             break
130         end
131     end
132
133
134 %%%%%%%%%%%%%%%%%%%%%%%%%%%%%%%%%%%%%%%%%%%%%%%%%%%%%%%%%%%%%%%%%%%%%%%%%%%%%%%%
135 %
136 %          Read all histograms into one matrix
137 %
138 %%%%%%%%%%%%%%%%%%%%%%%%%%%%%%%%%%%%%%%%%%%%%%%%%%%%%%%%%%%%%%%%%%%%%%%%%%%%%%%%
139
140 for i = 1:HistoResult_NumberOfCurves
141     fseek(fid,HistResDscr_DataOffset(i),'bof');
142     Counts(:,i) = fread(fid, HistResDscr_HistogramBins(i), 'uint32');
143 end;
144
145 Peak=max(Counts);
```

```

%%%%%%%%%%%%%%%%%%%%%%%%%%%%%%%%%%%%%%%%%%%%%%%%%%%%%%%%%%%%%%%%%%%%%%%%%%%%%%%%
%
%          Summary
%
%%%%%%%%%%%%%%%%%%%%%%%%%%%%%%%%%%%%%%%%%%%%%%%%%%%%%%%%%%%%%%%%%%%%%%%%%%%%%%%%

fprintf(1,'\n');
fprintf(1,'\n');
fprintf(1,'=======================================================\n');
fprintf(1,'                HISTOGRAM DATA SUMMARY                 \n');
fprintf(1,'=======================================================\n');
fprintf(1,'  Curve    Time bin    Number of     Peak     Integral \n');
fprintf(1,'  index   resolution   time bins     count     count   \n');
fprintf(1,'=======================================================\n');

for i = 1:HistoResult_NumberOfCurves
fprintf(1,'  %3i       %2.6g  %10i  %10i  %10i\n', HistResDscr_CurveIndex(i),
    HistResDscr_MDescResolution(i), HistResDscr_HistogramBins(i), Peak(i),
    HistResDscr_IntegralCount(i));
end;

%%%%%%%%%%%%%%%%%%%%%%%%%%%%%%%%%%%%%%%%%%%%%%%%%%%%%%%%%%%%%%%%%%%%%%%%%%%%%%%%
%
%          Next is a simple display of the histogram(s)
%
%%%%%%%%%%%%%%%%%%%%%%%%%%%%%%%%%%%%%%%%%%%%%%%%%%%%%%%%%%%%%%%%%%%%%%%%%%%%%%%%

figure(1);
semilogy(Counts);
% axis([0 max(max(Channels)) 1 10*max(max(Counts))]);
xlabel('Channel #');
ylabel('Counts');

if HistoResult_NumberOfCurves<21
   legend(num2str((1:HistoResult_NumberOfCurves)'),0);
end;

fclose(fid);
```

Code to produce Lorentz fit and the left plot in figure 3.20.

```
sp = loadSPE('E:\31ok\sessionnewsetup_31okt\groen516150blz_int5s_5001000.SPE') %150 BLZ
    spectrum 500-1000 nm, green pump, 5 sec integration
lorentzfit = 'A + B*(F^2)/(F^2+4*(x-a)^2)'
startPoints = [0.2 1 10 810];
xdata = sp.wavelength(1653:1881);
f1 = fit(xdata, (sp.int(1653:1881)/6588.78)', lorentzfit, 'Start', startPoints); %Setting
    peak to 1 by deviding by 6588.78 peak intensity
plot(xdata,(sp.int(1653:1881)/6588.78)');
hold on;
plot(f1);
ylim([0.15,1.2])
xlim([798,825]);
xlabel('Wavelength (nm)');
ylabel('Intensity (a.u.)');
legend({'Emission',['Lorentzian fit:' char(10) '$\lambda_0=808.7$,' char(10) 'FWHM $=2.97$
    ']},'interpreter','latex');
set(gca,'FontSize',20);
```

Code to produce g2 fit and the right plot of figure 3.20.

```
    xdata = 1:1000;
xdata = xdata * 0.064; %64 ps per bin
xdata = xdata-30.784; % correct for tau=0
read_PHU('newsetup_niceg2_higherrsolution_overnight.phu') %high resolution overnight
    measurement

g2_fitt = 'c-a*exp(-abs(x)/t1)+b*exp(-abs(x)/t2)';
StartPoints= [1 0 1 3 20];
f_g2 = fit(xdata', Counts(1:1000,3)/290.9,g2_fitt, 'Start', StartPoints,'Exclude',xdata
    >52-30.784, 'Exclude', xdata<12-30.784);
```

```
display(f_g2);
plot(xdata, Counts(1:1000,3)/290.9); %correlation data is 'normalized' by deviding by 290.9
hold on;
xlim([10,53]-30.784);
ylim([0,1.2]);
plot(f_g2);
ylabel('$g^{(2)}(\tau)$','interpreter','latex');
xlabel('$\tau$ (ns)','interpreter','latex');
minimum = min(Counts(1:1000,3)/290.9);
display(minimum); % exact minimum is 0.2716
yline(minimum,'Alpha',0.5,'LineStyle','--','LineWidth',2,...
    'Label','$g^{2}(0)=0.27$', 'interpreter', 'latex','FontSize',20);
legend('off');
```